Finite element modelling of hydraulic fracture flow in porous media.

Lobao, Mauricio Centeno

University of Wales Swansea
School of Engineering
Civil and Computational Eng. Centre

Finite Element Modelling of Hydraulic Fracture Flow in Porous Media

Mauricio Centeno Lobão
Eng.Mec. (UFSC), M.Sc. (UFSC)

Thesis submitted to the University of Wales in candidature
for the degree of Doctor of Philosophy

March 2007

Declaration and Statements

Declaration

This work has not previously been accepted in substance for any degree and is not being concurrently submitted in candidature for any degree.

Candidate: _____

Date: 27/07/2007

Statement 1

This thesis is the result of my own investigations, except where otherwise stated. Other sources are acknowledged by footnotes giving explicit references. A bibliography is appended.

Candidate: _____

Date: 27/07/2007

Statement 2

I am hereby consent for my thesis, if accepted, to be available for photocopying and for inter-library loan, and for the title and summary to be made available to outside organizations.

Candidate: _____

Date: 27/07/2007

Acknowledgments

My sincere gratitude for their inspiration, guidance, assistance and support goes to my supervisors Dr. E. A. de Souza Neto and Prof. D. R. J. Owen. Without their experience, knowledge, patience and enthusiasm, this thesis would not have been what it is today.

Also, I am grateful to Prof. R. J. Pine, Dr. J. S. Coggan and Dr. Z. N. Flynn from Camborne School of Mines at Cornwall for all their insightful ideas and discussions during this period of time.

I would like to thanks all the support and assistance received from colleagues at Rockfield Software Ltd. in the last four years which have being extremely important during the development of this research. I owe many thanks to Dr. A. J. L. Crook, Dr. G. Q. Liu and Dr. R. Eve for insightful ideas, interesting discussions and suggestions during the course of this work. I am really grateful to Dr. A. Garai, S. Y. Zhao, Dr. J. Armstrong, Dr. Jian Yu, Dr. Z. Wei, Dr. M. Cottrell, Dr. M. Dutko, M. Hudson, for all their patience and enthusiastic help. Furthermore, a warm thanks to Dr. M. Armstrong and Dr. F. Paw for all their assistance. And for Dr. H. J. Anderson and Dr. J. M. Rance for the all cooperation and great support given.

I am really grateful to Wulf Dettmer, Chenfeng Li, Andreas Rippl, Holger Ettinger, Miguel Rodriguez Paz for making my stay in Swansea so enjoyable.

Special thanks goes to Vasconcello's Family, Daisy, Marisa K. Morita, Francisco M. A. Pires, Silvina, Ricardo, Cristina, Rhodri and Caress Mugford, Andrew and Charllote, Norman and Janete Jenkins for a great friendship developed during this years. And to all my great friends Pablo, Bruno, Rodrigo, Henrique, Sideto, Breno, Stefan, Ligia and Sonia.

To my Parents, Sisters, Grandparents, Greatgrandmother and Family in law for their great love, patience, energy and advice during this time.

I would like to dedicate this achievement to my loved wife who has been absolutely brilliant. Her dedication, understanding and companionship during this period has been invaluable.

I would like to acknowledge the financial support received from the EPSRC Funded Research at the School of Enginnering in the UWS.

Contents

List of Figures

List of Tables

Abstract

In the present thesis, a computational framework for the analysis of coupled hydro-fracture flow in deformable porous media using a Finite/Discrete Element Method is presented. In this context, a series of developments have been made in order to provide a more efficient and robust numerical model capable of dealing with oil production and slope stability problems.

The mechanical response of the skeleton is highly dependent on its seepage behaviour as pore pressure modifications affect the in situ stress field. The *u-p* formulation has been employed using an explicit time integration scheme where fully saturated and single-phase partially saturated analysis are incorporated for 2-D and 3-D cases.

Owing to their inherent simplicity, low order elements provide an excellent framework in which contact conditions coupled with crack propagation can be dealt with in an effective manner. For linear elements this implies single point integration which, however, can result in spurious zero-energy modes. Therefore, in order to obtain reliable results, a stabilization technique has been devised to eliminate hourglassing.

The success of the modelling strategy ultimately depends on the interdependence of different phenomena. The linking between the displacement components, network and pore pressures represents an important role in the efficiency of the overall coupling procedure. Therefore, a master-slave technique is proposed to link seepage and network fields, proving to be particularly attractive from a computational cost point of view. Another important development that has provided substantial savings in CPU times is the use of an explicit-explicit subcycling scheme.

Numerical examples have been used to assess the accuracy and efficiency of the proposed framework. Special attention is focused on the investigation of hydraulic fracture propagation in oil production problems and plane failure analysis of the stability of slopes.

Chapter 1

Introduction

Due to the computational advances achieved in the last decade, the use of numerical models for the solution of practical engineering problems has increased significantly. Sophisticated models capable of solving coupled hydro-mechanical processes in fractured geological media, such as soils and rock masses, have been developed. These numerical tools are assisting analysts in the design, performance and safety assessment of many civil and environmental engineering works, such as dam foundations, slopes, extraction of oil, gas and water and leakage of hazardous materials (e.g. toxic and radioactive waste). These types of applications are characterized by the presence of soil or rock-like materials, in which the pores of the solid phase are filled with one or more fluids. An additional degree of complexity is introduced by the coalescence and growth of voids, which results in the appearance of macro-cracks and subsequent fragmentation. Despite the wide variety of applications as described above, the main focus of this research is related with oil production and slope stability problems. In the following section, a brief description of the mechanisms involved and previous related research are highlighted.

1.1 Motivation

It is well known that rocks and soils are characterized by a higher compression strength compared to their tensile strength. This plays an important role in determining a failure limit for these materials. In cases where fluids are injected into hydro-fractures an extensional loading develops ahead of the crack tip, due to the high net pressures developed. This creates a tensile stress field directly ahead of the crack tip, but at some offset from it, the stress decreases strongly in the direction perpendicular to the fracture plane. This type of stress behavior will cause the rock to shear and, consequently,

will induce the formation of a plastic zone, as shown in Figure 1.1.

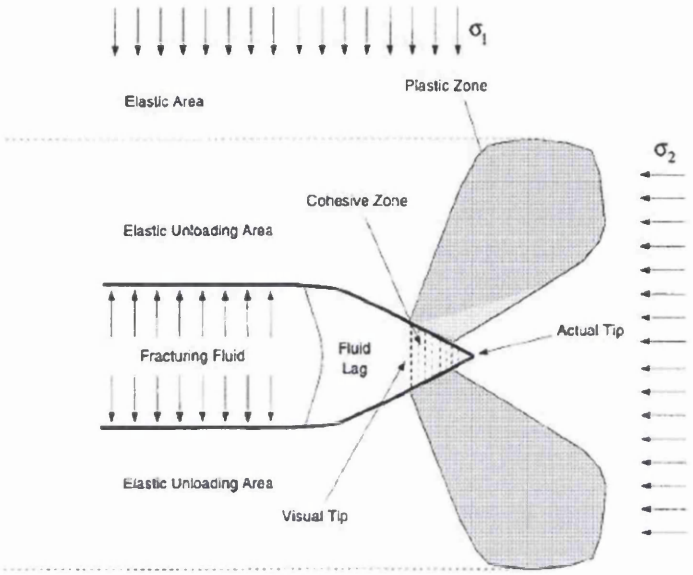

Figure 1.1: Plastic zone caused by high net pressures. (Papanastasiou (1999a))

The Delft Fracturing Consortium (Papanastasiou (1999a)) has recently carried out a world-wide survey on net-pressures, which has indicated that net-pressures in the field are 50 to 100 percent higher than the net-pressures predicted by the conventional hydraulic fracturing simulators. van Dam et al. (1997) observed that in weak formations the difference is even higher. In order to understand the difference in the results several approaches have been proposed. Among them, the most consistent with observations are the dilation hypothesis, effective fracture toughness and leak-off effects.

The first assumption, proposed by Cleary et al. (1991), states that rock dilation behind the advancing fracture would constrain the opening which may lead to sharp pressure gradients. Papanastasiou and Thiercelin (1993) and Papanastasiou (1997b) have used a finite difference-finite element scheme fully coupled with a fluid flow model to simulate the process. The model allows the fluid to flow through the cracks without taking into account any leak-off to the material itself. These studies have shown that the aperture in propagating elastoplastic fractures are wider than in the elastic case, resulting in smaller fluid-lag regions. This result is in complete contradiction with the dilation hypothesis proposed.

The second assumption states that values of the fracture toughness mea-

sured in the laboratory underestimate in-situ values. Shlyapobersky (1985) showed that typical toughness values determined from conventional laboratory tests are one to two times lower than estimates based on hydraulic fracturing fields. Papanastasiou (1999a) presented a fully hydro-mechanical coupled model which calculates the value of the effective fracture toughness using the path independent J-integral. The results of the study showed an increase of the effective fracture toughness (EFT) by more than one order of magnitude due to the fact that the plastic yielding near the tip of a propagating fracture provides an effective shielding. Also, this author found that the size of the plastic zone and the resulting EFT increases when the difference between the horizontal and vertical in-situ stress are higher. The conclusions agreed well with those stated by Shlyapobersky (1985). However, an accurate analysis of the *in situ* stress field can only be obtained if the soil or rock-like material is treated as a porous medium, since the effective stresses are significantly affected by changes in pore pressure, specially in pressure dependent materials, such as rock and soils.

Detournay et al. (1990) and Boone and Ingraffea (1990) have developed a hydraulic fracturing design model which incorporates poroelasticity effects and observed that net-pressures were higher than those predicted by conventional models. The results have shown that an increase in the fluid flow into the hydraulic fracture is necessary to avoid a drop in net-pressure due to leak-off through the formation. Consequently, higher net-pressure has to be developed in order to maintain the same fracture opening as for non-permeable models. These results agree well with the third assumption. However, more realistic solutions of the net-pressures, apertures and flow rates are expected when an elasto-plastic analysis is performed to account for the factors described in the second assumption.

Another set of hydro-mechanical coupling problems in a discontinuous porous medium, at which this work is particularly aimed, are slope stability problems. The causes of landslide in slopes are attributed to a number of factors such as geologic features, topography, vegetation, weather conditions or a combination of these factors.

In the analysis of rock slopes, the failure surface is often predefined as a continuous plane or a series of interconnected planes. In cases where the rock masses contain discontinuous joints varying in persistence, the shear strength becomes a combination of the friction strength component, the cohesion of the intact rock bridges between discontinuous joints and the magnitude of the effective normal stress. Bjerrum (1967) suggested that progressive slope failure is initiated when a reduction in the shear strength from peak to residual values occurs along the failure surface. This decrease causes the development of a continuous sliding surface through the progressive propagation of a shear

surface. Figure 1.2 illustrates the process described above.

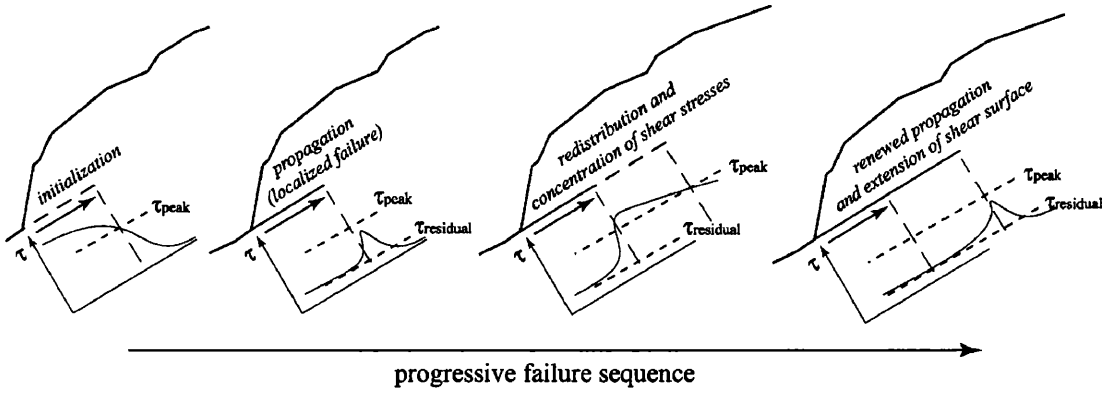

Figure 1.2: Development of a shear surface due to progressive failure. (Bjerrum (1967)).

In a recent survey of equilibrium methods of slope stability analysis, Duncan (1996) summarized the characteristics of a large number of methods, including the ordinary method of slices (Fellenius (1936)), Bishop's modified method (Bishop (1955)), force equilibrium methods (e.g. Lowe and Karafiath (1960)), Janbu's generalized procedure of slices (Janbu (1968)), Morgenstern and Price's method (Morgenstern and Price (1965)) and Spencer's method (Spencer (1967)). A difficulty with all these equilibrium methods is that they are based on the assumption that the failing soil mass can be divided into slices. Therefore, the approach made about directions of the side forces between slices becomes one of the main characteristics that distinguishes one limit equilibrium from another, and yet is itself an entirely artificial distinction.

In the last few years, several slope stability analyses have been carried out using the finite element (FE) approach. Griffiths and Lane (1999) have shown that the FE method is reliable and robust for assessing the factor of safety of slopes. Ng and Shi (1998) and Cho and Lee (2001) have examined the process of infiltration into a slope due to rainfall and its effect on soil slope behavior using a FE flow-deformation coupled analysis. Eberhardt et al. (2004) have used a Finite/Discrete Element method which combines continuum and discontinuum methodologies, to understand the progressive failure in massive natural rock slopes as a function of slide plane surface and internal strength degradation. These studies has revealed the advantages of the FE analysis over conventional limit equilibrium methods which can be summarized as follows:

- Failure occurs 'naturally' in zones where the soil shear strength is unable to support the applied shear stresses, without it being necessary in advance to postulate the shape or location of the failure surface.
- Global equilibrium is preserved until failure is reached in the FE approach. In the FE method there is no concept of slices and consequently, there is no need for any hypothesis about slice side forces.
- The FE method, at working stresses levels, provides information about deformations when consistent soil properties data are given.

In order to obtain a better understanding of the progressive failure mechanism and a more accurate assessment of the factor of safety in rock/soil slopes, the combination of a porous elasto-plastic analysis with hydraulic fractures becomes crucial. With this approach, a decrease in the frictional strength of the joints and changes in matric suction of rock mass caused by the fluid flow are expected. Consequently, the shear strength, which is primarily responsible for the stability of the slope, will be affected.

Therefore, the development of a complex computational model which allows the flow along fractures as well as the flow within the material itself and an elasto-plastic analysis becomes the main goal of this research.

1.2 Objectives

Several theories and approaches have been used to improve the understanding of the complex interplay between different phenomena related with oil extraction and slope stability analyses. The use of computational models have been shown to be particularly attractive in the solution of such problems, particularly the ones based on the Finite Element Method. However, some assumptions have been taken by current numerical models which have constrained their capabilities, as described in section 1.1.

In order to tackle some of the difficulties presented, several tasks have been pursued in this thesis as described below:

- Implementation and validation of a 2D and 3D explicit Soil-Pore Fluid interaction analysis in the Elfen (2005) code.
- A stabilization procedure to eliminate spurious singular modes in seepage analysis (quadrilateral and hexahedral elements). The verification of the reliability of the scheme has been carried out in detail.

- Development of a computational model for 2D and 3D analysis of coupled hydro-fracture flow in porous media using a Finite/Discrete Element Method and an explicit time integration scheme.
- Simulation of a hydraulic fracture propagation in a porous medium, with particular interest on oil extraction and slope stability problems;
- Analysis of the influence of the plastic zones on the extension, apertures, pressures and flow rates in a fractured porous medium;
- Assessment of the factor of safety for slope stability problems subjected to flow along fractures and changes in effective normal stress.

1.3 Layout of the thesis

This document is organized in the following manner.

- Chapter 2 - presents some basic concepts of porous media, such as, Darcy's law, properties of a porous medium, effective stress principle and saturation. Also, it allows the understanding of the limits of validity of Darcy's Law. Finally, it defines the governing equations and some of their limitations.
- Chapter 3 - discretizes the governing equations in space and time using a finite element method and an explicit difference scheme. Also, it defines the constitutive problem to be solved and failure criteria adopted. Finally, it explains important aspects related to the numerical stability and stabilization of singular spurious modes.
- Chapter 4 - gives a detailed description of the overall coupling procedure developed. An explicit subcycling scheme is proposed in order to reduce computational cost. Finally, a mass conservation balance is verified through a dynamic filtration test, in order to show the robustness of the numerical model.
- Chapter 5 - shows some of the previous work developed to tackle the hydraulic fracture problem and their limitations. Also, it defines the hydraulic fracture problem and its particular features. Finally, it presents a series of numerical examples.
- Chapter 6 - describes a plane failure analysis in slopes to verify the influence of water pressure effects on stability. A joint element is introduced in the failure plane in order to model the water flow in these

cracks. This is particularly interesting, since, the increase in water pressure is well known to affect the effective tangential stresses causing a reduction in the friction force. Consequently, a slope failure is expected. The factor of safety obtained through theory is tested against a numerical model.

- Chapter 7 - gives a discussion of the overall objectives tackled, main conclusions and suggestions for future research.

- Appendix A - presents the formulation used in the stabilization of singular spurious modes with 3D elements.

Chapter 2

Basic concepts of porous media

Soils are three phase systems consisting of solid grains with fluids and gases filling the void spaces between the grains. The nature of the grains, current state, structure or fabric and formation are the primarily factors responsible for the mechanical properties of a soil.

In oil production and slope stability analysis, both seepage and network flows are estimated by Darcy's law. In spite of this similarity, differences can be seen in the determination of some properties and formulation of the governing equations for each field. This plays an important role in the understanding of the assumptions that have been made and consequently, determines the range of validity within which it is acceptable to use them.

In order to provide some background to the following chapters some of the basic concepts related to the theory of porous media will be given.

2.1 Soils particle sizes and shapes

In the description of the main features of a soil it is important to take into account size, grading, shape, surface texture and mineralogy of the grains, currents stress and moisture content, history of loading and unloading, type of fabric or structure (layering, bedding, fissure, jointing and cementing) and type of formation (naturally deposited, residual product of rock weathering or compacted by machines).

According to the predominant size of the particles, soils are classified as boulders, cobbles, gravel, sand, silt, or clay. In spite of several organizations having developed different soil description schemes, in the United Kingdom the British Standards for site investigations B. S. 5930 (1981) and for soil testing B. S. 1377 (1991) provides the characteristics of the most common soils in the region.

The distribution of particle sizes in a soil is represented by a grading curve on a particle size chart, as shown in Figure 2.1. If the soil contains a wide variety of particle sizes, i.e., the grading curve is flat, the soil is known as well graded. On the other hand, if a particular size predominates the soil is poorly graded. Often, the analysis of the grading of a soil reflects its origin.

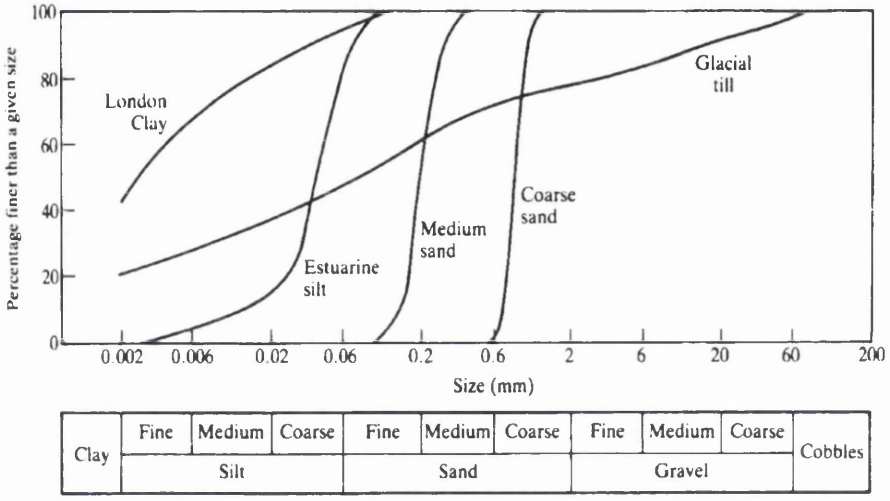

Figure 2.1: Grading curves plotted on a particle size distribution chart. (B. S. 1377 (1991)).

Another feature that distinguish the soil particles are their shape. Usually, rotund shapes occur more predominantly in silt, sand and gravel, while, thin plates are more common in clay grains.

2.2 Basic relationships

Most of the basic relationships encountered in the Theory of Porous Media relates to the contents of fluid and grains through weight and volume ratios, since the compactation of the packing of the grains is responsible for modifications in many mechanical properties; for example, loose soils are weaker and more compressible than dense soils. Therefore, the definition of some of the basic relationships are essential to obtain a better understanding of the concepts that will follow in the present work.

- Specific gravity (G_s)

  In soil mechanics the calculation of the specific gravity is often needed. It defines the ratio between the mass densities of the dry solid grains, ρ_s,

and water, ρ_w. It can be easily obtained from the laboratory through a water displacement test, giving

$$G_s = \frac{W_s}{W_w} = \frac{\rho_s}{\rho_w} \tag{2.1}$$

where, W_s is the weight of the dry solid grains and W_w is the weight of water displaced. Table 2.1 shows values of the specific gravity for some common minerals found in soils.

Table 2.1: Specific gravity of important minerals. (Das (1985))

Mineral	Specific gravity G_s
Quartz	2.65
Kaolinite	2.6
Illite	2.8
Halloysite	2.65 - 2.80
Potassium feldspar	2.57
Sodium and clacium feldspar	2.62 - 2.76
Chlorite	2.6 - 2.9
Biotite	2.8 - 3.2
Muscovite	2.76 - 3.1
Hornblende	3.0 - 3.47
Limonite	3.6 - 4.0
Olivine	3.27 - 3.37

- Specific volume (v)

  The state of a soil can be described by the specific volume, which is defined as the ratio between the volume of a soil sample, V, and the volume of dry solid grains, V_s, i.e.

$$v = \frac{V}{V_s} \tag{2.2}$$

  For coarse grained soils the maximum specific volume for a loose assembly of uniform spheres is 1.92 and the minimum v of a dense assembly is 1.35; common sands and gravels have specific volumes in the range 1.3 to 2.0.

- Void ratio e_{vr} and porosity n)

  Experimental tests have shown that the permeability of a soil, which will be detailed in Section 2.4, is significantly affected by changes in the volume of voids. Owing to this, the permeability is often given as a function of the void ratio or the porosity. Void ratio is defined as the ratio between volume of voids, V_v, and the volume of dry solid grains, V_s.

$$e_{vr} = \frac{V_v}{V_s} = \upsilon - 1 \tag{2.3}$$

  Porosity represents the ratio between the volume of voids and the total volume, i.e.

$$n = \frac{V_v}{V} = \frac{e_{vr}}{1 + e_{vr}} \tag{2.4}$$

- Moisture content w and unit weight γ

  The moisture content is defined as the ratio between the weight of water W_w and the weight of dry solid grains W_s in a given volume of soil,

$$w = \frac{W_w}{W_s} = \frac{\upsilon - 1}{G_s} \tag{2.5}$$

  and the unit weight is the weight of soil, W, per unit volume, V.

$$\gamma = \frac{W}{V} = \left(\frac{G_s + \upsilon - 1}{\upsilon}\right)\gamma_w, \tag{2.6}$$

  where γ_w is the unit weight of water.

  The weights can be measured by simple weighing and the volume of the cubic or cylindrical sample determined by direct measurement. Since, the specific volume cannot be measured directly, its determination through a relation with the water content and the unit weight becomes convenient.

2.3 Darcy's law

In 1856, Henry Darcy developed an experimental procedure to investigate the flow of water in vertical homogeneous sand filters, as shown in Figure 2.2. Darcy observed that the rate of flow , Q $[L^3/T]$, is proportional to

the cross-sectional area A, proportional to the difference in piezometric head across the filter $h_1 - h_2$ which is measured with respect to some arbitrary datum level, and inversely proportional to the length L of the filter. Darcy's law has been formulated based on these observations as

$$Q = KA\frac{(h_1 - h_2)}{L} \tag{2.7}$$

where K is a coefficient of proportionality known as the hydraulic conductivity to be discussed in Section 2.4. Often, Darcy's formula is rewritten as

$$q = \frac{Q}{A} = K\frac{(h_1 - h_2)}{L} \tag{2.8}$$

where the specific discharge q $[L/T]$ is defined as the quantity of fluid flowing in a unit time per unit of cross-sectional area of soil normal to the direction of flow. However, the actual velocity of the fluid (seepage velocity) through the void spaces is higher than q. A relationship between the specific discharge and the seepage velocity,v_s, can be derived as follows.

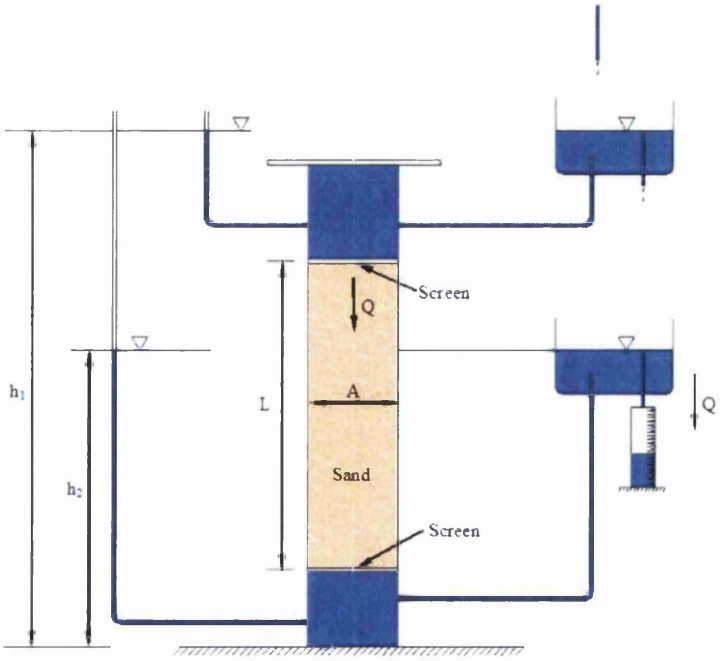

Figure 2.2: Darcy's experiment.

The rate of flow, Q through a horizontal soil column of length L with a cross sectional area A, as shown in Figure 2.3, can be defined as:

$$Q = qA = A_v v_s \tag{2.9}$$

where, A_v is the area of voids in the cross-section of the specimen.

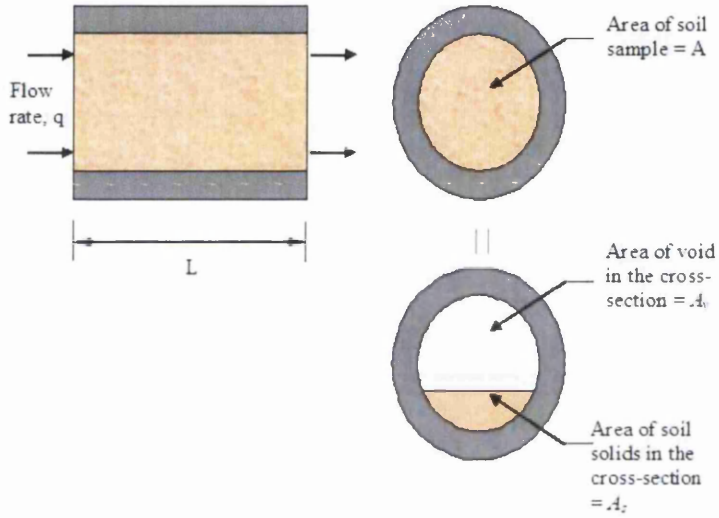

Figure 2.3: Derivation of seepage velocity (v_s).

Since the cross-sectional area is the sum of the area of voids and area of solids

$$A = A_v + A_s \tag{2.10}$$

then,

$$Q = q(A_v + A_s) = A_v v_s \tag{2.11}$$

or

$$v_s = \frac{q(A_v + A_s)}{A_v} = \frac{q(A_v + A_s)L}{A_v L} = \frac{q(V_v + V_s)}{V_v} = \frac{q}{n} \tag{2.12}$$

The piezometric head at a point in the fluid under motion can be defined by Bernoulli's equation as the sum of the kinetic and potential energies, which is written in the following manner:

$$h = \frac{p}{\rho g} + \frac{v^2}{2g} + z \tag{2.13}$$

where, h is the total head, p is the pressure, v is the velocity, g is the gravity acceleration and ρ is the mass density.

The terms in the formula represent the pressure, velocity and elevation heads respectively. In cases where the seepage velocities are small, the term containing the velocity head can be neglected due to the fact that changes in the kinetic energy are small when compared to changes in the piezometric head. This allows the piezometric head to be adequately represented by:

$$h = \frac{p}{\rho g} + z \tag{2.14}$$

For a compressible fluid under isothermal conditions, $\rho = \rho(p)$. A more physical insight into fluid flow in porous media, especially as related to petroleum engineering, was given by the introduction of a piezometric head by Hubbert (1940) in the following form:

$$h^* = z + \int_{p_0}^{p} \frac{dp}{\rho(p)g} \tag{2.15}$$

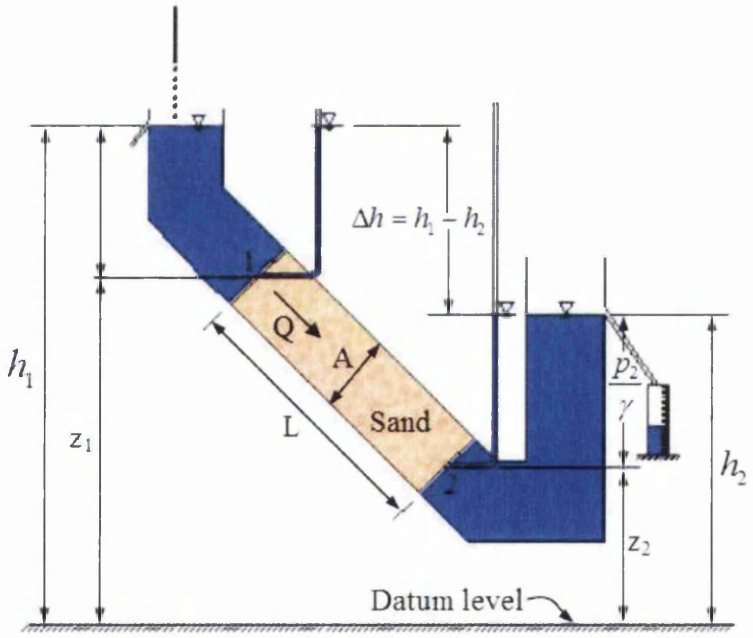

Figure 2.4: Seepage flow through an inclined sand filter.

It is important to observe that Darcy's law states that flow will take place from a higher piezometric head to a lower one. This can be verified in an inclined homogeneous sand filter, as shown in Figure 2.4. In this case, the pressure head at point 1 is smaller when compared to the one at point 2, but, the flow is in the direction of increasing pressure or decreasing head.

Darcy's law was experimentally derived for a one-dimensional flow of an isotropic homogeneous incompressible fluid. An extension to a three-dimensional form is obtained as

$$q = -K\nabla h = -\frac{k}{\mu}(\nabla p - \rho g) \tag{2.16}$$

where, $K = \rho g k/\mu$, μ is the dynamic viscosity of the fluid and k is the intrinsic permeability $[L^2]$ which will be seen in detail in Section 2.4. In the case of a compressible fluid, the motion equation (2.16) may be written as:

$$q = -K\nabla h^* \tag{2.17}$$

2.3.1 Range of validity

As expressed by equation (2.16), the specific discharge, q, varies linearly with the piezometric head. However, this relationship is only acceptable for laminar flow occurring at low velocities, as illustrated by Figure 2.5.

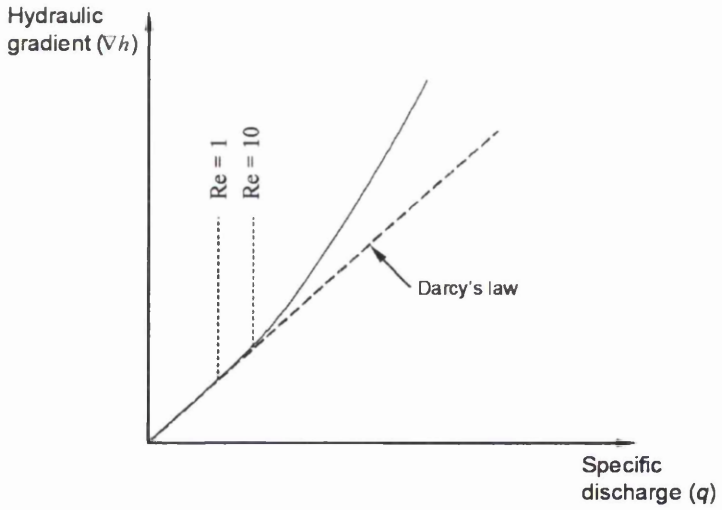

Figure 2.5: Schematic curve relating the hydraulic gradient to the specific discharge.

In fluid mechanics, the dimensionless Reynolds number, Re, identifies whether laminar (low velocities) or turbulent (high velocities) flows occur, through the evaluation of the ratio of inertial to viscous forces acting on the fluid. By analogy, a Reynolds number can be defined for flow through porous

media as

$$Re = \frac{\rho q d}{\mu} \tag{2.18}$$

where, μ is the dynamic viscosity of the fluid and d is some representative length of the porous matrix. Often, this length dimension is defined by the mean grain diameter. Although, there is still some controversy regarding the length dimension d, Darcy's law has been shown to be valid for values of the Reynolds number varying between 1 and 10 (Bear (1979)).

2.4 Hydraulic conductivity K

In Darcy's law, the specific discharge, q, is related to the hydraulic gradient through a coefficient of proportionality, known as the hydraulic conductivity, as shown in Equation (2.8), which has dimensions of $[L/T]$. It is a scalar value that expresses the ease with which a fluid is transported through a porous matrix.

In the derivation of a relationship for the hydraulic conductivity several factors must be considered, such as: pore and grain size distribution, roughness of the mineral particles, void ratio, fluid viscosity, temperature and degree of saturation. It is therefore a coefficient which depends on both matrix and fluid properties. Nutting (1930) has proposed a relationship which expresses the hydraulic conductivity as:

$$K = \frac{\rho g k}{\mu} \tag{2.19}$$

where, the mass density, ρ, and the dynamic viscosity, μ, are related to fluid properties, while, the intrinsic permeability, k, is associated solely with the solid matrix. Table 2.2 presents some values of intrinsic permeability for rocks and soils.

The randomness of particle size distribution, void ratio and pore structures contribute to the hetereogenety of natural soils. Owing to this, several empirical equations and theories proposed have related the intrinsic permeability with microscale properties of porous media.

Hazen (1930), based on observations from experiments on loose, clean sand filters, has proposed an empirical relation in the form:

$$k = cd^2 \tag{2.20}$$

where c is a coefficient in the range between 45 for clayey sand, and 140 for pure sand, and d is the effective grain diameter. Often, d_{10}, the diameter

Table 2.2: Typical values of intrinsic permeability. [Bear (1979)]

Rocks	Intrinsic permeability $k[m^2]$
Oil Rocks	1.0×10^{-11} - 1.0×10^{-14}
Sandstone	1.0×10^{-14} - 1.0×10^{-16}
Good limestone, dolomite	1.0×10^{-16} - 1.0×10^{-18}
Breccia, granite	1.0×10^{-18} - 1.0×10^{-20}
Soils	**Intrinsic permeability $k[m^2]$**
Clean gravel	1.0×10^{-07} - 1.0×10^{-09}
Clean sand or sand and gravel	1.0×10^{-09} - 1.0×10^{-12}
Very fine sand, silt, loess, loam, solonetz	1.0×10^{-12} - 1.0×10^{-16}
Peat	1.0×10^{-11} - 1.0×10^{-13}
Stratified clay	1.0×10^{-13} - 1.0×10^{-16}
Unweathered clay	1.0×10^{-16} - 1.0×10^{-20}

such that 10 percent by weight of the grains are smaller than that diameter, is used as the effective grain diameter.

Modifications occurring in the structure and texture of the solid matrix caused by consolidation, subsidence, swelling or other factors, may cause the permeability to vary with time. For this reason, it is common to express the intrinsic permeability as a function of the void ratio. A purely theoretical formula obtained from derivations of the Hagen-Poiseuille equation combined with Darcy's law to model the flow in a horizontal capillary is the Kozeny-Carman equation. The model defines the intrinsic permeability as a function of the specific area of the porous matrix, M_s, the void ratio, e, and a coefficient, C_0, for which Carman (1937) suggested the value of 0.2. The Kozeny-Carman equation is expressed as:

$$k = C_0 \frac{e^3}{(1+e)M_s^2} \tag{2.21}$$

More recent studies have been developed to estimate the permeability of porous media through the use of stochastic methods assuming a permeability probability density function. The construction of the probability density function for permeability can be based on experiments or analytical reliability

approximation methods, details can be seen in the work of Turcke and Kueper (1996) and Li et al. (2005) respectively.

Several units are used in practice for the intrinsic permeability. In the International System of Units, SI, m^2 is frequently used as an unit, while, in the Imperial - United Kingdom Units it is common to see ft^2. Reservoir engineers use the unit *darcy* (d) defined as:

$$1\ darcy = 9.8697 \text{ x } 10^{-13}\ m^2 = 1.0624 \text{ x } 10^{-11}\ ft^2$$

2.5 Saturation

Depending on the amount of water and gas that soils contain, they are defined as dry (no fluids), saturated (no gases) or partially saturated (fluid and gases). In the majority of the problems involving slope stability and oil extraction, the soil is usually a multiphase system where the voids in the skeleton are partly filled with fluid and partly filled with gases. Therefore, a straightforward relationship arises as:

$$S_f + S_g = 1 \tag{2.22}$$

where, S_f and S_g are the degree of fluid and gas saturation respectively.

The development of negative pore pressures are direct related with soil dilation phenomena. During the process of soil dilation, separation surfaces in the fluid contained in the pores are formed and voids are opened up, since they are incapable of sustaining tension forces, leading to the well known capillary effects. The voids are normally opened when the fluid pressure value reaches zero, causing the air to ingress from the free water surface if this is open to atmosphere. This allows a simplified approach of the unsatured case to be easily obtained if the atmospheric pressure is neglected, $p_{atm} = 0$. From computational point of view this is particularly attractive since the number of variables to be solved are reduced. However, it is important to emphasize that mainly for oil extraction problems this assumption will introduce some restrictions in the overall analysis.

It is noted that the degree of saturation, S_f, is dependent on the pore fluid pressure in a complex manner. The relationship is, therefore, simplified by defining absorption, S_{fa}, and exsorption curves, S_{fe}, together with a "scanning" curve that defines the transition between the two curves (Figure 2.6). Using this definition saturation is defined as

$$S_f(p_f) \quad \text{with} \quad S_{fa}(p_f) \leq S_f(p_f) \leq S_{fe}(p_f) \tag{2.23}$$

where, S_{fa} is the limit where absorption will occur, i.e., saturation increases ($\dot{S}_f > 0$) and $S_{fe}(p_f)$ is the limit where exsorption will occur, i.e., saturation decreases ($\dot{S}_f < 0$). The scanning curve, which defines the transition from the absorption to the exsorption curve, is approximated as a straight line.

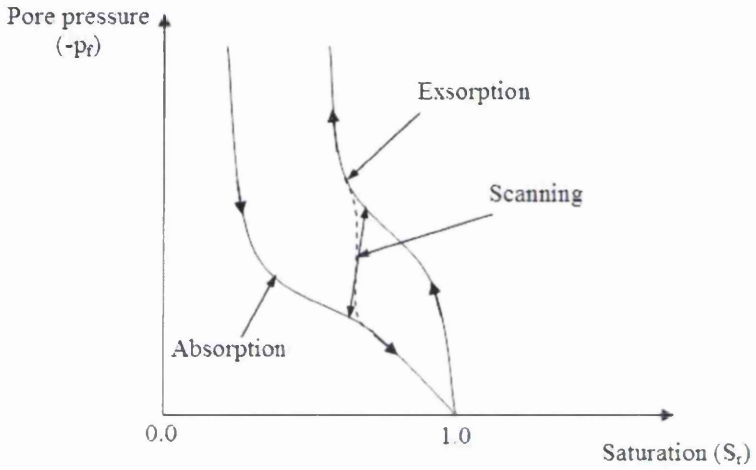

Figure 2.6: Typical absorption and exsorption behavior.

As the soil becomes increasingly partially saturated the volumetric content of the soil decreases. This reduces the permeability or hydraulic coefficient of the soil as the transport of fluid is impeded by the reduction in the number of fluid filled spaces. The relationship between permeability and soil saturation is normally given as a saturation-permeability curve as shown in Figure 2.7. The permeability is then defined as a function of the saturation as

$$k_f(S_f) = \kappa_r(S_f) k_f^{sat} \tag{2.24}$$

where, $\kappa_r(S_f)$ is a relative permeability factor and k_f^{sat} is the permeability when the soil is fully saturated. The saturation-permeability curve may be specified for both isotropic and anisotropic materials.

2.5.1 Numerical example

In the following example, an idealized undrained embankment with 12 m height is submitted to a gravitational force, following the model proposed in Slide (2002). A constant water table of 10 m is considered to act on the left side of the slope and a drain with 12 m length is positioned on the right bottom as detailed in the layout in Figure 2.8. The material properties are

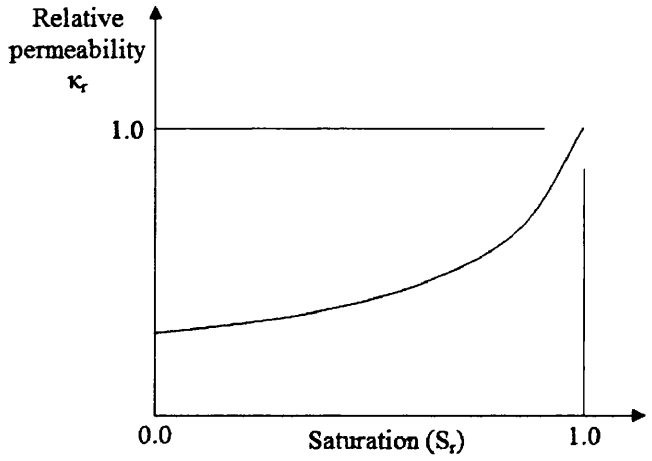

Figure 2.7: Relative permeability-saturation curve for partially saturated soils.

given by Table 2.3, while the absorption curve and the relative permeability as a function of the saturation curve are given by Figure 2.9 items (a) and (b) respectively.

The main goal is to determine the free surface location in isotropic and anisotropic cases and compare the pressure head along the vertical line AA against the ones provided by Slide (2002), consequently verifying the consistency of the numerical implementation presented here.

The free surface displays a different location in isotropic and anisotropic cases as shown in Figures 2.10 and 2.11. A higher pressure head gradient is verified in the isotropic case due to higher vertical permeability which facilitates the flow throughout the drain.

The pressure head results are shown to be slightly lower than the ones provided by Slide (2002) as shown in Figures 2.12 (a) and (b). These are expected to be a consequence of a two phase analysis where the assumption of negligible pressure of the gases have been adopted in the present work, while, a three phase analysis have been used by Slide (2002). Apart from that, the qualitative behavior has been shown to be in good agreement and, quantitatively, the differences are acceptable.

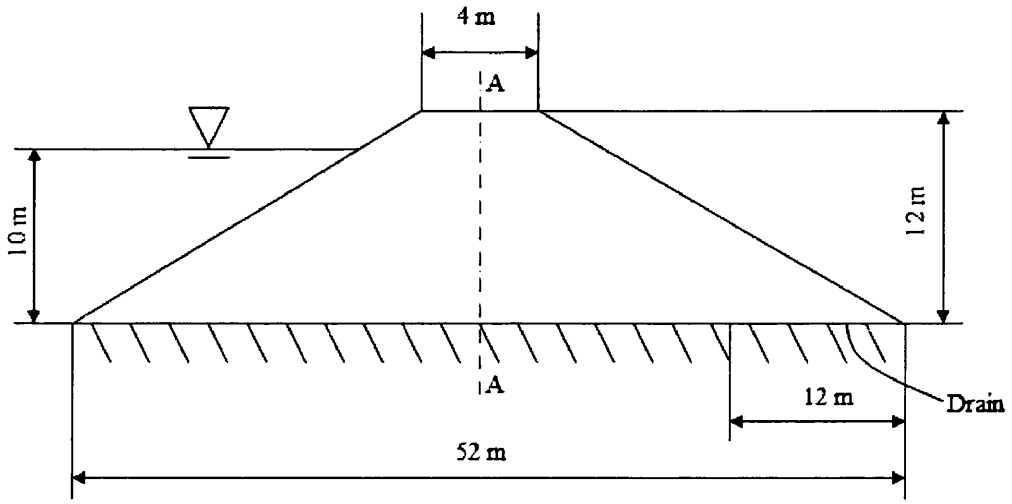

Figure 2.8: Layout of the problem.

Input parameters	
Young Modulus	1.3 MPa
Poisson ratio	0.4
Grain mass density	2000 kg/m^3
Fluid mass density	1000 kg/m^3
Permeability in x	1.0e-07 m^2
Permeability in y	1.11e-08 m^2
Grain bulk modulus	2.167 MPa
Fluid bulk modulus	2.0 GPa
Viscosity	0.001 Pa.s
Porosity	0.2975

Table 2.3: Material properties of the embankment.

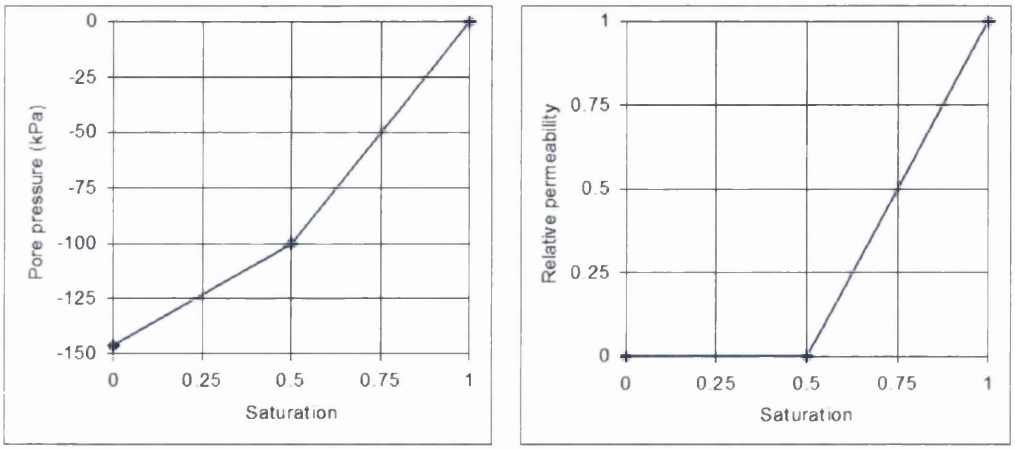

(a) (b)

Figure 2.9: (a) Pore pressure vs. saturation curve. (b) Relative permeability vs. saturation curve.

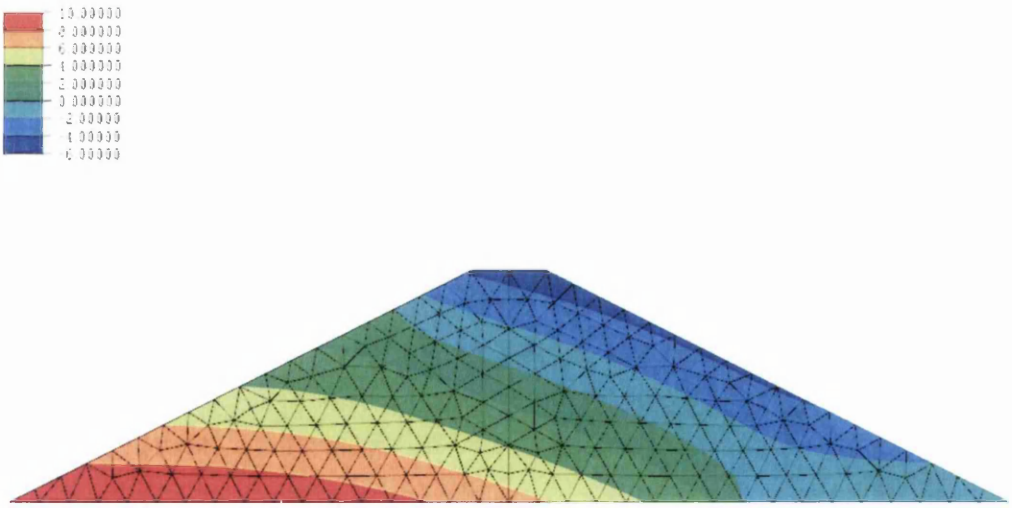

Figure 2.10: Hydraulic head column of an unsaturated isotropic embankment.

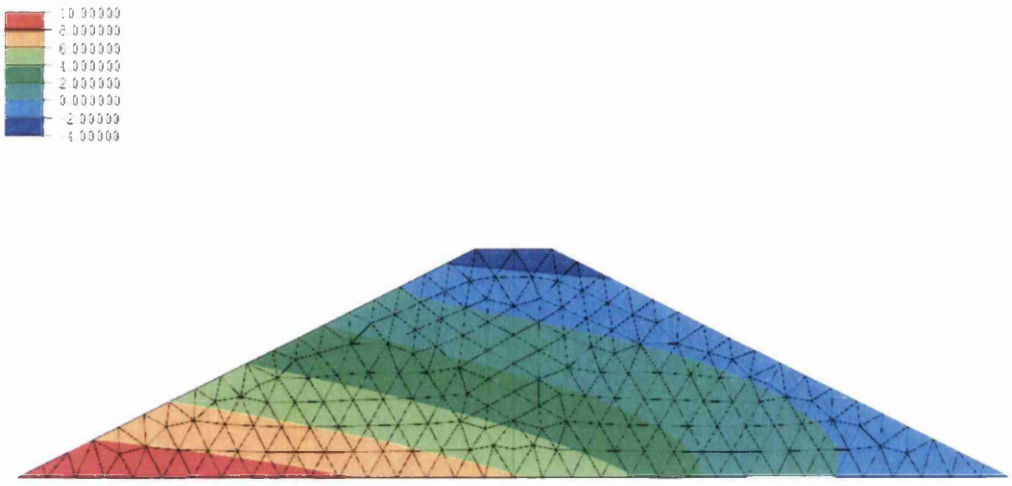

Figure 2.11: Hydraulic head column of an unsaturated anisotropic embankment.

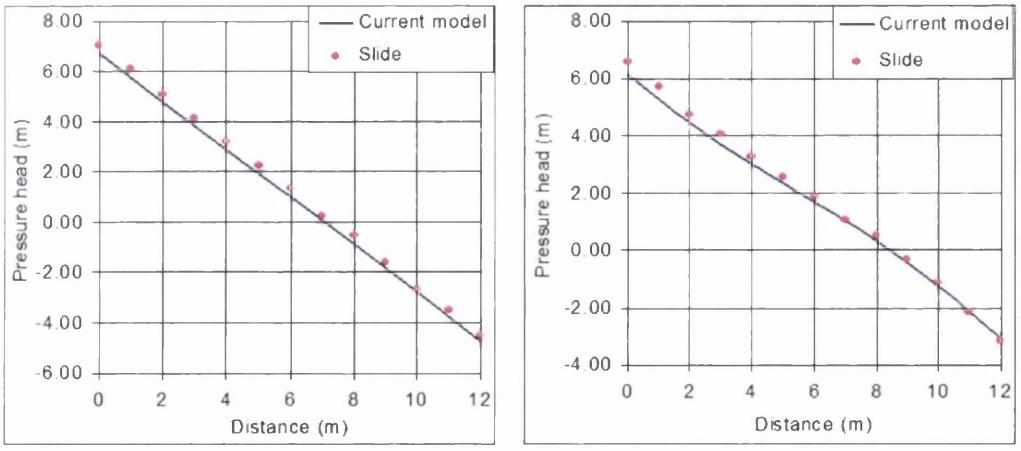

(a) Isotropic (b) Anisotropic

Figure 2.12: Comparison of the head pressures predicted by the current model in the isotropic and anisotropic cases against the ones presented by Slide (2002).

2.6 Effective stress principle

The principle of effective stress, $\boldsymbol{\sigma}'$, is absolutely fundamental to understanding the modifications occurring in the in situ stresses in soils and rocks. Their magnitudes can be modified either by changes occurring in the total stresses, $\boldsymbol{\sigma}$, while pore fluid pressures are constant, or, by alterations in pore fluid pressure, p, while the total stresses are kept constant. Its concept was first introduced by von Terzaghi and Redulic (1934) and von Terzaghi (1936) as:

$$\boldsymbol{\sigma}' = \boldsymbol{\sigma} + \mathbf{I}p \tag{2.25}$$

This is accepted for soils, where, the deformation of the grains is significantly small with respect to the overall skeleton. However, in rock mechanics and in concrete, where the compressibility of the grain is not negligible, it is necessary to extend this concept to take the compressibility into account. It was the works of Biot (1941), (1955), (1956a), (1956b) and (1962), which extended the effective stress principle to consider the grain deformation. The new effective stress was defined as:

$$\boldsymbol{\sigma}'' = \boldsymbol{\sigma} + \alpha\mathbf{I}p \tag{2.26}$$

where, α is the Biot number. This is related to the bulk modulus of the skeleton, K_T, and the bulk modulus of the grain, K_S, through the equation:

$$\alpha = 1 - \frac{K_T}{K_S} \tag{2.27}$$

The relationship between effective stress and total stress, in the general case of partially saturated behavior with air pressure neglected is different from that defined in equation (2.26), since the pore pressure is now dependent on a saturation parameter, S_f. The usual form of the effective stress in soil mechanics can be given as:

$$\boldsymbol{\sigma}'' = \boldsymbol{\sigma} + \alpha S_f\, \mathbf{I}p, \tag{2.28}$$

It can be seen that the relation between effective stress ($\boldsymbol{\sigma}''$) and total stress ($\boldsymbol{\sigma}$) in a multiphase medium is not independent of the soil because of the saturation; whereas in fully saturated soils, where $S_f = 1$, the effective stress principle is unique for all soil types.

2.7 Governing Equations

Continuum mechanics has been extensively used to model the behavior of solids subject to mechanical loads resulting in a set of differential equations whose solution is usually obtained numerically.

In the modeling of a hydraulic fracture in a porous medium, the mechanical behavior and the fluid flow into the fracture is well represented by a set of four governing equations, stated as:

- Momentum balance equation for the partially saturated soil-fluid mixture;
- Momentum balance equation for the fluid alone;
- Mass conservation equation for the fluid flow in the seepage;
- Mass conservation equation for the fluid flow in an individual fracture.

The use of appropriate assumptions, as will be discussed in detail in Sections 2.7.1, 2.7.2 and 2.7.3, allows the elimination of the momentum equilibrium equation for the fluid alone, reducing the number of variables to be solved.

2.7.1 Momentum balance equations

In the present work, particular attention has been given to problems involving phenomena of medium speed and dynamics of lower frequencies. For these kinds of situations as discussed previously by Zienkiewicz et al. (1980), the fluid acceleration relative to the solid and the convection terms can be neglected in the total momentum equilibrium equation for the partially saturated soil-fluid mixture, as shown in the following equation.

$$\sigma_{ij,j} + \rho\ddot{u}_i - \underline{S_f\rho_f[\dot{w}_i + w_j w_{i,j}]} - \rho b_i = 0 \tag{2.29}$$

where σ_{ij} is the total stress, $\ddot{u}_i$ is the solid acceleration, b_i is the body force and w_i is the fluid velocity.

Also, air pressure has been neglected. Assuming that the mass density of the gas phase is negligible, we can write the mass density of the mixture (ρ) as:

$$\rho = nS_f\rho_f + (1-n)\rho_s \tag{2.30}$$

where n is the porosity, ρ_f and ρ_s are the fluid and soil mass density respectively.

The second equation is defining the momentum equilibrium for the fluid alone. Using the same assumptions described for the above equation, we have:

$$p_{sf,i} - \frac{R_i}{n} + S_f \rho_f \ddot{u}_i - \underline{S_f \rho_f [\dot{w}_i + w_j w_{i,j}]/n} - S_f \rho_f b_i = 0 \tag{2.31}$$

where R_i represents the viscous drag force which, assuming the validity of Darcy's seepage law, is given by:

$$\frac{k_{ij}}{\mu} \frac{R_j}{n} = w_i \tag{2.32}$$

In the above, k_{ij} defines the permeability coefficients and μ is the dynamic viscosity.

2.7.2 Mass conservation equations

The third equation is supplied by the mass conservation equation for the seepage flow, described as:

$$\frac{\dot{p}_{sf}}{Q_{sf}} + S_f \alpha \dot{\varepsilon}_{ii} + w_{i,i} + \underline{S_f n \frac{\dot{\rho}_f}{\rho_f}} = 0 \tag{2.33}$$

where $\dot{p}$ is the rate of change of pressure in time. The term Q_{sf} represents the combined compressibilities of the fluid and solid phase which can be related to the bulk modulus of each component and with the saturation of the soil as:

$$\frac{1}{Q_{sf}} = C_s + \frac{nS_f}{K_f} + \frac{(\alpha - n)S_f(S_f + C_s p/n)}{K_s} \tag{2.34}$$

In the final equation, an individual fracture is treated as a single confined aquifer, in which the mass conservation is based on the cubic law of flow in fracture (Snow (1968), Witherspoon (1980)) described as:

$$\frac{\dot{p}_{nf}}{Q_{nf}} + \dot{\varepsilon}_{ii} + \frac{e^2}{12\mu}(p_{nf'j} - \rho_f b_j + \rho_f \ddot{u}_j)_{'i} = 0 \tag{2.35}$$

where, e is the aperture of the fracture (with unit of m) and μ is the viscosity (with unit of Pa.s).The term Q_{nf} represents the storativity of a single fracture, and like a porous medium, reflects the compressibilities of the fluid and rock. However, the rock compressibility term does not reflect the intergranular skeleton, but rather the pressure dependence of the fracture volume, which is simply the normal stiffness of the fracture K_{frac} (with unit of Pa/m). The storativity, Q_{nf}, of the single fracture is obtained as:

$$\frac{1}{Q_{nf}} = \frac{1}{e}\left[\frac{1}{K_{frac}} + eC_f\right] \tag{2.36}$$

and the intrinsic permeability of the fracture (k_{frac}) is given by:

$$k_{frac} = \frac{e^2}{12} \tag{2.37}$$

Remarks:

The cubic law was first derived for solid interfaces with smooth walls (parallel fractures), which are only crude approximations of reality. Iwai (1976a) and (1976b) has derived flow equations for non-parallel wedge shaped fractures based on the same ideas adopted in the derivation of the cubic law. In his work the hydraulic aperture of a wedge-shaped non-parallel aperture has been taken as an equivalent aperture, e, with a modification factor, F, to the mean hydraulic aperture, e_m. The final form of the equivalent aperture can be calculated by:

$$e = \frac{e_m}{F} = e_m \left[\frac{16 r_e^2}{(1 + r_e)^4} \right]^{\frac{1}{3}} \tag{2.38}$$

where, r_e is the ratio between the apertures at the two ends, e_a and e_b, of the wedge-shaped fracture. From a mathematical point of view, the ratio, r_e, and mean hydraulic aperture, e_m, are given by:

$$r_e = \frac{e_a}{e_b} \quad and \quad e_m = \frac{1}{2}(e_a + e_b) \tag{2.39}$$

A number of models have been formulated in order to consider the surface roughness but for simplicity the model described above has been used in the present work.

2.7.3 The u-p formulation

The omission of the underlined terms in equations 2.29, 2.31 and 2.33, allows w_i to be eliminated from the equation system retaining only u_i and p as primary variables. This simplification allows the final forms of the governing equations, which is known as the $\mathbf{u}-p$ formulation, to be written as:

$$\sigma_{ij,j} + \rho \ddot{u}_i - \rho b_i = 0 \tag{2.40}$$

$$\frac{\dot{p}_{sf}}{Q_{sf}} + \alpha \dot{\varepsilon}_{ii} + \frac{k_{ij}}{\mu}(p_{sf'j} - \rho_f S_f b_j + \rho_f S_f \ddot{u}_j)_{'i} = 0 \tag{2.41}$$

The system given by the three governing equations (2.40), (2.41) and (2.35) and the boundary conditions presents a well-defined problem which can be discretized and solved numerically.

Chapter 3

Coupled finite element procedure

The numerical simulation of a hydraulic fracture in a porous medium demands a minimum knowledge of the mathematical and numerical models involved in the process. Among the existing numerical techniques, the Finite Element Method (FEM) is the most commonly used to provide numerical solutions to coupled problems of the type discussed in this thesis. Since the general procedures are described in detail in many texts such as Zienkiewicz and Taylor (2000) and Belytschko et al. (2000), the present work will focus on the concepts and definitions related to the specific subject.

Firstly, a Galerkin (or weighted residual) statement is used to obtain a weak form of the equation system discussed in the previous section. Then, a discretization in space is made by a standard finite element procedure. Finally, a Central Difference method is applied for discretization in time. The general notation of Zienkiewicz and Taylor (2000) are used in the following together with vector notation.

3.1 Principle of virtual work. Weak form.

The momentum and mass conservation equations (2.40), (2.41) and (2.35) described in previous sections cannot be discretized directly by FEM. Firstly, they must be rewritten in another format, called the weak or variational form. Through the weighted residual technique applied to the governing equations, it is possible to obtain after integration an equivalent statement called the principle of virtual work.

The weighted residual technique consists of the product of the governing equations with the test functions, $\hat{u}$, $\hat{p}_{sf}$ and $\hat{p}_{nf}$, respectively and their

integration over the domain, where, the test functions are obtained from the difference between two trial functions.

It is essential that the trial functions must satisfy all the boundary conditions in $\partial\Gamma_u$, $\partial\Gamma_{sf}$ and $\partial\Gamma_{nf}$, and are sufficiently regular to allow the operations of differentiation and integration. The set K_u, K_{sf} and K_{nf} of trial functions that satisfy all the above conditions are known as displacement kinematically admissible and pressure admissible. From a mathematical point of view,

$$\begin{aligned} K_u &= \{u(X,t) \mid \text{is sufficiently regular}, u = \tilde{u} \text{ in } \partial\Gamma_u\} \\ K_{sf} &= \{p_{sf}(X,t) \mid \text{is sufficiently regular}, p_{sf} = \tilde{p}_{sf} \text{ in } \partial\Gamma_{sf}\} \\ K_{nf} &= \{p_{nf}(X,t) \mid \text{is sufficiently regular}, p_{nf} = \tilde{p}_{nf} \text{ in } \partial\Gamma_{nf}\} \end{aligned} \tag{3.1}$$

Therefore, the virtual displacements and pressures fields can be defined as:

$$\begin{aligned} \vartheta_u &= \{\hat{u}(X,t) \mid \text{is sufficiently regular}, \hat{u} = 0 \text{ in } \partial\Gamma_u\} \\ \vartheta_{sf} &= \{\hat{p}_{sf}(X,t) \mid \text{is sufficiently regular}, \hat{p}_{sf} = 0 \text{ in } \partial\Gamma_{sf}\} \\ \vartheta_{nf} &= \{\hat{p}_{nf}(X,t) \mid \text{is sufficiently regular}, \hat{p}_{nf} = 0 \text{ in } \partial\Gamma_{nf}\} \end{aligned} \tag{3.2}$$

Considering the inertia forces , the weak form of the momentum equation states that: "A body is in equilibrium if and only if the effective stress field, σ'', satisfy the equation":

$$\int_{\Omega_u} \left[(\boldsymbol{\sigma}'' - \alpha p_{sf}\mathbf{I}) : \boldsymbol{\nabla}_x \hat{u} - \rho \mathbf{b}\hat{u}\right] d\Omega_u + \int_{\Omega_u} \rho \ddot{\mathbf{u}}\hat{u} d\Omega_u - \int_{\Gamma_u} \mathbf{f_1}\hat{u} d\Gamma_u = 0 \tag{3.3}$$

While, the weak form of the mass conservation equations states that: "If no mass is created or destroyed inside a defined volume, the inflow rate must be in balance with the outflow rate

$$\begin{aligned} &\int_{\Omega_{sf}} \left[\mathbf{w}_{sf} \cdot (\boldsymbol{\nabla}_x \hat{p}_{sf})\right] d\Omega_{sf} + \int_{\Omega_{sf}} \alpha S_f \dot{\varepsilon}_v \hat{p}_{sf} d\Omega_{sf} + \\ &\qquad \int_{\Omega_{sf}} \rho_f \frac{\dot{p}_{sf}}{Q_{sf}} \hat{p}_{sf} d\Omega_{sf} - \int_{\Gamma_{sf}} f_2 \hat{p}_{sf} d\Gamma_{sf} = 0 \end{aligned} \tag{3.4}$$

$$\begin{aligned} &\int_{\Omega_{nf}} \left[\mathbf{w}_{nf} \cdot (\boldsymbol{\nabla}_x \hat{p}_{nf})\right] d\Omega_{nf} + \int_{\Omega_{nf}} \dot{\varepsilon}_v \hat{p}_{nf} d\Omega_{nf} + \\ &\qquad \int_{\Omega_{nf}} \rho_f \frac{\dot{p}_{nf}}{Q_{nf}} \hat{p}_{nf} d\Omega_{nf} - \int_{\Gamma_{nf}} f_3 \hat{p}_{nf} d\Gamma_{nf} = 0'' \end{aligned} \tag{3.5}$$

When the effective stress and flux terms are modified by the constitutive, kinematic, Darcy's law and cubic law the equilibrium problem become a boundary value problem, where the aim is to find the displacement and pressures fields that satisfy the effective stress and flux fields that are in balance with the external forces. So, for a given constitutive equation,

$$\boldsymbol{\sigma}'' = \breve{\boldsymbol{\sigma}}''(\boldsymbol{\varepsilon}^t(\mathbf{u})) \tag{3.6}$$

the boundary value problem is defined as: "Determine the displacement field $u \in K_u$ and pressures field $p_{sf} \in K_{p_{sf}}$ and $p_{nf} \in K_{p_{nf}}$, such that"

$$\begin{aligned}\int_{\Omega_u} \left[(\breve{\boldsymbol{\sigma}}''(\boldsymbol{\varepsilon}^t(\mathbf{u})) - \alpha p_{sf}\mathbf{I}) : \boldsymbol{\nabla}_x \hat{u} - \rho \mathbf{b}\hat{u}\right] d\Omega_u + \\ \int_{\Omega_u} \rho \ddot{\mathbf{u}}\hat{u} d\Omega_u - \int_{\Gamma_u} \mathbf{f_1}\hat{u} d\Gamma_u = 0 \quad \forall \hat{u} \in \vartheta_u\end{aligned} \tag{3.7}$$

$$\begin{aligned}\int_{\Omega_{sf}} \left[\left(\frac{\mathbf{k}}{\mu}\boldsymbol{\nabla}_x p_{sf}\right) \cdot \boldsymbol{\nabla}_x \hat{p}_{sf} - \boldsymbol{\nabla}_x \cdot \left(\frac{\mathbf{k}}{\mu}\rho_f S_f \mathbf{b}\right)\hat{p}_{sf}\right] d\Omega_{sf} + \\ \int_{\Omega_{sf}} \boldsymbol{\nabla}_x \cdot \left(\frac{\mathbf{k}}{\mu}\rho_f S_f \ddot{\mathbf{u}}\right)\hat{p}_{sf} d\Omega_{sf} + \int_{\Omega_{sf}} \alpha S_f \dot{\varepsilon}_v \hat{p}_{sf} d\Omega_{sf} + \\ \int_{\Omega_{sf}} \rho_f \frac{\dot{p}_{sf}}{Q_{sf}}\hat{p}_{sf} d\Omega_{sf} - \int_{\Gamma_{sf}} f_2 \hat{p}_{sf} d\Gamma_{sf} = 0 \quad \forall \hat{p}_{sf} \in \vartheta_{p_{sf}}\end{aligned} \tag{3.8}$$

$$\begin{aligned}\int_{\Omega_{nf}} \left[\left(\frac{e^2}{12\mu}\boldsymbol{\nabla}_x p_{nf}\right) \cdot \boldsymbol{\nabla}_x \hat{p}_{nf} - \boldsymbol{\nabla}_x \cdot \left(\frac{e^2}{12\mu}\rho_f \mathbf{b}\right)\hat{p}_{nf}\right] d\Omega_{nf} + \\ \int_{\Omega_{nf}} \boldsymbol{\nabla}_x \cdot \left(\frac{e^2}{12\mu}\rho_f \ddot{\mathbf{u}}\right)\hat{p}_{nf} d\Omega_{nf} + \int_{\Omega_{nf}} \dot{\varepsilon}_v \hat{p}_{nf} d\Omega_{nf} + \\ \int_{\Omega_{nf}} \rho_f \frac{\dot{p}_{nf}}{Q_{nf}}\hat{p}_{nf} d\Omega_{nf} - \int_{\Gamma_{nf}} f_3 \hat{p}_{nf} d\Gamma_{nf} = 0 \quad \forall \hat{p}_{nf} \in \vartheta_{p_{nf}}\end{aligned} \tag{3.9}$$

The next step consists in finding a solution for the fields $u(x)$, $p_{sf}(x)$ and $p_{nf}(x)$ using the finite element method.

3.2 Incremental finite element procedures

The finite element method is applied to obtain numerical solution of problems such as described in equations (3.3)-(3.5). The method consists in replacing the trial functions sets K_u, K_{sf}, K_{nf}, ϑ_u, ϑ_{sf} and ϑ_{nf} by the discrete

subsets ${}^hK_u$, ${}^hK_{sf}$, ${}^hK_{nf}$, ${}^h\vartheta_u$, ${}^h\vartheta_{sf}$ and ${}^h\vartheta_{nf}$ generated by a finite element discretization h of the domains Ω_u, Ω_{sf} and Ω_{nf}.

$$
\begin{aligned}
{}^hK_u &\equiv \left\{ {}^hu(x,t) = \mathbf{N}_u(x)\mathbf{U}(t) | {}^hu(x,t) = \tilde{u}(x,t) \; if \; x \in \partial\Gamma_u \right\}, \\
{}^hK_{sf} &\equiv \left\{ {}^hp_{sf}(x,t) = \mathbf{N}_p(x)\mathbf{P}_{sf}(t) | {}^hp_{sf}(x,t) = \tilde{p}_{sf}(x,t) \; if \; x \in \partial\Gamma_{sf} \right\}, \\
{}^hK_{nf} &\equiv \left\{ {}^hp_{nf}(x,t) = \mathbf{N}_p(x)\mathbf{P}_{nf}(t) | {}^hp_{nf}(x,t) = \tilde{p}_{nf}(x,t) \; if \; x \in \partial\Gamma_{nf} \right\}, \\
{}^h\vartheta_u &\equiv \left\{ {}^h\hat{u}(x,t) = \mathbf{N}_u(x)\hat{\mathbf{U}}(t) | {}^h\hat{u}(x,t) = 0 \; if \; x \in \partial\Gamma_u \right\}, \\
{}^h\vartheta_{sf} &\equiv \left\{ {}^h\hat{p}_{sf}(x,t) = \mathbf{N}_p(x)\hat{\mathbf{P}}_{sf}(t) | {}^h\hat{p}_{sf}(x,t) = 0 \; if \; x \in \partial\Gamma_{sf} \right\}, \\
{}^h\vartheta_{nf} &\equiv \left\{ {}^h\hat{p}_{nf}(x,t) = \mathbf{N}_p(x)\hat{\mathbf{P}}_{nf}(t) | {}^h\hat{p}_{nf}(x,t) = 0 \; if \; x \in \partial\Gamma_{nf} \right\}
\end{aligned}
\tag{3.10}
$$

In the above, $\mathbf{N}_u(x)$ and $\mathbf{N}_p(x)$ are the matrix and vector of the interpolation functions respectively. $\mathbf{U}$, $\mathbf{P}_{sf}$ and $\mathbf{P}_{nf}$ are vectors of nodal values of displacement, seepage pressure and network pressure respectively. $\hat{\mathbf{U}}$, $\hat{\mathbf{P}}_{sf}$ and $\hat{\mathbf{P}}_{nf}$ are vectors of nodal virtual displacement, seepage pressure and network pressure respectively. For example, in two-dimensional problems the matrix $\mathbf{N}_u(x)$ and the vector $\mathbf{N}_p(x)$ have the form:

$$
\begin{aligned}
\mathbf{N}_u(x) &= \begin{bmatrix} N_1(x) & 0 & N_2(x) & 0 & \cdots & N_{nnode}(x) & 0 \\ 0 & N_1(x) & 0 & N_2(x) & \cdots & 0 & N_{nnode}(x) \end{bmatrix} \\
\mathbf{N}_p(x) &= \begin{bmatrix} N_1(x) & N_2(x) & \cdots & N_{nnode}(x) \end{bmatrix}
\end{aligned}
\tag{3.11}
$$

Often, Lagragian finite elements are used. For this particular type of element, the interpolation functions are such that their value is one at the node and zero in the remain nodes. In this case, the value of the parameters $\mathbf{U}$, $\mathbf{P}_{sf}$ and $\mathbf{P}_{nf}$ are equal to nodal values of the displacement, seepage pressure and network pressure in each degree of freedom.

The approximation by the finite element method of the continuum variational equations (3.7)-(3.9) is then obtained by the substitution of the trial functions sets K_u, K_{sf}, K_{nf}, ϑ_u, ϑ_{sf} and ϑ_{nf} by the subsets of finite dimensions defined above.

3.3 Constitutive problem

To define the constitutive equations, it is necessary to admit that the thermodynamic state of a point can be completely characterized by knowing a set of state variables,

$$\{\mathbf{F}, \theta, \mathbf{g}_t, \boldsymbol{\alpha}_k\} \tag{3.12}$$

where, $\mathbf{F}$ is the deformation gradient, θ is the temperature, $\mathbf{g}_t$ is the temperature gradient and $\boldsymbol{\alpha}_k$ are internal variables, normally used to describe dissipative phenomena. For example, in the following models, the internal variables are typically plastic deformation and hardening. Therefore, based on this assumption the Helmholtz free energy is assumed to have the form:

$$\psi = \psi\left(\mathbf{F}, \theta, \boldsymbol{\alpha}_k\right) \tag{3.13}$$

The substitution of equation (3.13) into the well known Clausius-Duhem inequality, produces an inequality which must be satisfied for any process subject to a change from one state to another:

$$\left[\boldsymbol{\sigma}''\mathbf{F}^{-T} - \rho\frac{\partial\psi}{\partial\mathbf{F}}\right] : \dot{\mathbf{F}} - \rho\left[s + \frac{\partial\psi}{\partial\theta}\right] : \dot{\theta} - \rho\frac{\partial\psi}{\partial\alpha_k}\,\dot{\alpha}_k - \frac{1}{\theta}\,\mathbf{q}_h\,\mathbf{g}_t \geq 0 \tag{3.14}$$

where, s is the entropy per unit of deformed volume and $\mathbf{q}_h$ is the heat flux. In particular, if thermal effects are neglected, we have:

$$\begin{gathered}\psi = \psi\left(\mathbf{F}, \boldsymbol{\alpha}_k\right), \\ \left[\boldsymbol{\sigma}''\mathbf{F}^{-T} - \rho\frac{\partial\psi}{\partial\mathbf{F}}\right] : \dot{\mathbf{F}} - \rho\frac{\partial\psi}{\partial\boldsymbol{\alpha}_k}\,\dot{\boldsymbol{\alpha}}_k \geq 0\end{gathered} \tag{3.15}$$

This inequality defines the limits of the thermodynamic process and therefore, defines rules that the constitutive equations to be developed must satisfy. Analyzing the inequality (3.15) considering dissipative or non-dissipative processes, it is possible to find a set of general expressions to the constitutive equations, such that, these satisfy the thermodynamical principles. These are:

$$\begin{aligned}\psi &= \psi\left(\mathbf{F}, \boldsymbol{\alpha}_k\right), \\ \boldsymbol{\sigma}'' &= \rho\frac{\partial\psi}{\partial\mathbf{F}}, \\ \dot{\boldsymbol{\alpha}}_k &= f(\mathbf{F}, \boldsymbol{\alpha}_k)\end{aligned} \tag{3.16}$$

In the infinitesimal case, as occurs in the problems that the present work is particularly interested in, the deformation gradient, $\mathbf{F}$, can be replaced by the infinitesimal strain tensor, $\boldsymbol{\varepsilon}$, and the effective stress tensor $\boldsymbol{\sigma}''$ of the infinitesimal theory replaces the effective first Piola-Kirchhoff stress. We then can rewrite the general constitutive law as:

$$\begin{aligned}\psi &= \psi\left(\boldsymbol{\varepsilon}, \boldsymbol{\alpha}_k\right), \\ \boldsymbol{\sigma}'' &= \rho\frac{\partial\psi}{\partial\boldsymbol{\varepsilon}}, \\ \dot{\boldsymbol{\alpha}}_k &= f(\boldsymbol{\varepsilon}, \boldsymbol{\alpha}_k)\end{aligned} \tag{3.17}$$

The first equation denotes that the effective stress state can be defined as the derivative of a potential (Helmholz free energy) with respect to the strain tensor. The second equation defines the evolution law for the internal variables. This set of equations defines the "constitutive problem", and it is given in terms of rates, i.e., temporal derivatives of the variables.

The constitutive problem is described as: "Given the history of the deformation gradient, find the free-energy and effective stress according to the constitutive law conceptually expressed by (3.16) or (3.17)".

Assuming that the constitutive equations of the material model are path dependent, i.e., the effective stress tensor depends on the history of the deformations to which the material has been subjected, and not only on its instantaneous values, it can be concluded that the effective stress tensor is then obtained through the solution of the constitutive problem (3.17), and a solution can be found, using the integration algorithms of the constitutive equations, given in temporal rate forms of the variables required.

The choice of a particular technique for integration of a constitutive law will be dependent on the considered model. In general, algorithms to integrate the rate constitutive equations are obtained by the adoption of some kind of time discretization, along with some assumption on the deformation path between adjacent time stations [de Souza Neto et al. (2002)]. In formulations involving small strains, the algorithm defines an incremental constitutive function in the following format:

$$\boldsymbol{\sigma}''_{(n+1)} = \breve{\boldsymbol{\sigma}}''(\boldsymbol{\alpha}_{(n)}, \boldsymbol{\varepsilon}_{(n+1)}) \tag{3.18}$$

i.e., given the set of internal variables, $\boldsymbol{\alpha}_{(n)}$, the infinitesimal strain tensor, $\boldsymbol{\varepsilon}_{(n+1)}$, will determine the effective stress tensor, $\boldsymbol{\sigma}''$, uniquely through an incremental constitutive function, $\breve{\boldsymbol{\sigma}}''$, defined by some kind of numerical integration algorithm of the constitutive equations of the model.

The incremental constitutive law is, in general, non-linear and path independent in an increment, i.e., in each increment $\boldsymbol{\sigma}''_{(n+1)}$ depends only on $\boldsymbol{\varepsilon}_{(n+1)}$ (note that $\boldsymbol{\alpha}_{(n)}$ is constant in each load increment). Also, the algorithm must define an incremental constitutive function for the internal variables of the model:

$$\boldsymbol{\alpha}_{(n+1)} = \breve{\boldsymbol{\alpha}}(\boldsymbol{\alpha}_{(n)}, \boldsymbol{\varepsilon}_{(n+1)}) \tag{3.19}$$

3.4 Hypoelastic-plastic models

These models precede historically the hyperelastic-plastic models and are still frequently used in the majority of commercial codes. For this type of models there is in general no energy conservation in a closed elastic strain

cycle. However, for the case of small elastic strains, the energy error is insignificant, so that it makes their use possible, for example, in hydraulic fracture problems in porous media.

For these constitutive models, the deformation rate, $\mathbf{D}$, is decomposed into an elastic part $\mathbf{D}^e$ and a plastic part, $\mathbf{D}^p$ [Belytschko et al. (2000)]:

$$\mathbf{D} = \mathbf{D}^e + \mathbf{D}^p \tag{3.20}$$

Following this decomposition, an equation for the effective stress in terms of rates is defined, i.e., the variation in time of effective stress measure, $\dot{\boldsymbol{\Sigma}}''$, depends on the elastic strain rate:

$$\dot{\boldsymbol{\Sigma}}'' = \mathbf{C}^e : \mathbf{D}^e \tag{3.21}$$

where, $\dot{\boldsymbol{\Sigma}}''$ denotes some kind of objective rate of some effective stress measure $\boldsymbol{\Sigma}''$ and $\boldsymbol{C}^e$ is the elastic tangential modulus.

On the other hand, the plastic strain rate is calculated by the derivative of the plastic flow potential, $\Psi(\boldsymbol{\Sigma}'', \mathbf{A})$:

$$\mathbf{D}^p = \dot{\gamma}\frac{\partial \Psi(\boldsymbol{\Sigma}'', \mathbf{A})}{\partial \boldsymbol{\Sigma}''} \tag{3.22}$$

The above equation defines that the direction of yielding is given by the derivative of a function of the plastic flow potential in relation to the effective stress measure chosen, while the magnitude of the plastic strain rate is defined by the plastic multiplier $\dot{\gamma}$.

Finally, an evolution law for the internal variables, $\boldsymbol{\alpha}_k$ is obtained by the derivative of the plastic flow potential, Ψ, with respect to the set of thermodynamic forces, $\mathbf{A}$, frequently represented by hardening parameters, shown as:

$$\dot{\boldsymbol{\alpha}} = -\dot{\gamma}\frac{\partial \Psi(\boldsymbol{\Sigma}'', \mathbf{A})}{\partial \mathbf{A}} \tag{3.23}$$

The plastic loading/unloading condition is defined by the following criterion, known as the complementarity condition:

$$\Phi(\boldsymbol{\sigma}'', \mathbf{A}) \leq 0, \quad \dot{\gamma} \geq 0, \quad \dot{\gamma}\Phi = 0 \tag{3.24}$$

The function $\Phi(\boldsymbol{\sigma}'', \mathbf{A})$ is the yield function. Condition (3.24) has the following meaning: If the state of a material point is such that $\Phi < 0$, then the point is in the elastic region and plasticity can not occur, i.e., $\dot{\gamma} = 0$. If, on the other hand, plasticity occurs, $\dot{\gamma} > 0$, the state of a material point must lie on the yield surface, i.e., $\Phi(\boldsymbol{\sigma}'', \mathbf{A}) = 0$.

In the present case, the yield functions, Φ, will be chosen as the Mohr-Coulomb function which will be detailed in Subsection 3.5.1. Also, if it is assumed that the plastic flow potential, Ψ, coincides with the yield function, Φ, i.e.,

$$\Psi = \Phi \tag{3.25}$$

then the model is said to be associative. For non-associative models, the flow potential is generally different from the yield function.

The integration of equations (3.21) to (3.23) using appropriate techniques during a load increment, allows us to find an expression for the incremental constitutive equation in which the general symbolic format is given by expression (3.17). Finally, it is important to remark that the effective stress rate, $\dot{\boldsymbol{\Sigma}}''$, has to satisfy the principle of material objectivity, i.e., " the material response is independent of the observer". This property is not satisfied, for example, by the rate of effective Cauchy stress tensor, i.e., $\dot{\boldsymbol{\sigma}}''$ is not an objective stress rate.

Many objective effective stress rates are defined in the literature, as Jaumann, Truesdell and Green-Naghdi rates. This last one is particularly attractive because the incrementally objective integration algorithm is simple when compared to others. The Green-Naghdi rate of the effective Cauchy stress tensor, $\check{\boldsymbol{\sigma}}''$, is obtained by rotating the effective Cauchy stress tensor to the reference configuration, taking the time material derivative of the rotated quantity and then rotating the resulting derivative back to the deformed configuration [de Souza Neto et al. (2002)], i.e.,

$$\check{\boldsymbol{\sigma}}'' \equiv \mathbf{R}\left[\frac{d}{dt}(\mathbf{R}^T\boldsymbol{\sigma}''\mathbf{R})\right]\mathbf{R}^T = \dot{\boldsymbol{\sigma}}'' - \boldsymbol{\Omega}\boldsymbol{\sigma}'' + \boldsymbol{\sigma}''\boldsymbol{\Omega} \tag{3.26}$$

where, the skew-symmetric tensor is the spin of the Eulerian triad relative to the Lagragian triad, defined as:

$$\boldsymbol{\Omega} \equiv \dot{\mathbf{R}}\mathbf{R}^T \tag{3.27}$$

and the proper orthogonal tensor $\mathbf{R}$ is the local rotation tensor.

In soils and rocks, the incremental effective stress $(d\check{\sigma}''_{ij})$ is responsible for all major deformations in the skeleton and is related to the incremental strain $(d\varepsilon_{ij})$ and rotation $(d\Omega_{kl})$ by means of an incremental constitutive relationship, of the form,

$$d\check{\sigma}''_{ij} = D_{ijkl}(d\varepsilon_{kl} - d\varepsilon^0_{kl}) + d\sigma''_{ik}d\Omega_{kj} + d\sigma''_{jk}d\Omega_{ki} \tag{3.28}$$

where, the last two terms account for the rotational stress changes, the term D_{ijkl} is a fourth order tensor and is defined by state variables and the direction of the increment. Finally, $d\varepsilon^0_{ij}$ represents the increment initial strain tensor due to thermal or autogeneous strain of the grain compression.

3.5 Classic yield criteria

Given the effective stress state in a body, when this achieves a critical value established by a yield criterion, plastic flow may occur. This principle can be understood as: given a yield function, if this is negative, only elastic strain will occur. However, if the functions achieve a value equal to zero, plastic flow may occur.

The yield function Ψ is defined as a function of the effective stress state (given by $\boldsymbol{\sigma}''$), and a set of thermodynamic forces of hardening, $\mathbf{A}$. The condition is:

$$\Psi(\boldsymbol{\sigma}'', \mathbf{A}) \leq 0 \tag{3.29}$$

A state ($\boldsymbol{\sigma}''$, $\mathbf{A}$) is said to be in the elastic domain whilst the potential $\Psi < 0$. If, on the other hand, it is in a state such that $\Psi(\boldsymbol{\sigma}'', \mathbf{A}) = 0$, it is said to be on the yield surface, where plastic straining may take place.

Often, the behavior of rocks and soils are described by pressure-sensitive yield criteria such as the Mohr-Coulomb model. In this, the effective hydrostatic pressure state to which the material is subjected, defines a specific yield limit where plasticity may initiate. A more detailed description of the above yield criterion will follow.

3.5.1 Mohr-Coulomb yield criterion

The criterion was developed with the intent of predicting the macroscopic plastic yielding resulting from the frictional sliding between material particles. This states that "*plastic yielding begins when, on a plane in the body, the effective shear stress, τ'', is higher than the yield limit for a given effective normal stress, σ_n''.*

It is important to emphasize that, there are basically two mechanisms that could trigger the plastic yielding in a Mohr-Coulomb model. The first can be a consequence of volumetric changes occurring in the body which could cause modifications in the effective hydrostatic pressure, initiating the plastic yielding. The second can be due to the shearing of the material which affects the effective deviatoric stresses of the material. Therefore, assuming that the material behavior in the elastic zone is linear, the elastic strain-energy, ψ^e, defined by a stress tensor, σ, can be decomposed as a sum of two parts:

$$\psi^e = \psi_d^e + \psi_v^e \tag{3.30}$$

The first part is the contribution of the distortion or shearing energy, ψ_d^e,:

$$\rho\psi_d^e = \frac{1}{2G}\mathbf{S}_{\sigma''} : \mathbf{S}_{\sigma''} = \frac{1}{G}J_2(\mathbf{S}_{\sigma''}) \tag{3.31}$$

where, G is the shear modulus, $\mathbf{S}_{\sigma''}$ is the component of the effective deviatoric stress, defined as:

$$\mathbf{S}_{\sigma''} = \boldsymbol{\sigma}'' - \frac{1}{3}tr(\boldsymbol{\sigma}'')\mathbf{I} \tag{3.32}$$

and $J_2(S_{\sigma''})$ is the second invariant, defined as:

$$J_2(\mathbf{S}_{\sigma''}) = \frac{1}{2}\mathbf{S}_{\sigma''} : \mathbf{S}_{\sigma''} \tag{3.33}$$

The second part is the density of the volumetric strain energy, ψ_v^e,:

$$\rho\psi_v^e = \frac{1}{K_V}(p'')^2 \tag{3.34}$$

where, K_V is the bulk modulus and p'' is the effective hydrostatic stress component defined as:

$$p'' = \frac{1}{3}(\sigma_1'' + \sigma_2'' + \sigma_3'') \tag{3.35}$$

with, σ_1'', σ_2'' and σ_3'', being the effective principal stresses.

The invariant representation of the Mohr-Coulomb yield function can be expressed as [see Owen and Hinton (1980)]:

$$\Phi = \left(\cos(\theta) - \frac{1}{\sqrt{3}}\sin\theta\,\sin\phi\right)\sqrt{J_2(S_{\sigma''})} + p''(\boldsymbol{\sigma}'')\,\sin\phi - c\,\cos\phi - \sigma_y'' \tag{3.36}$$

where, c, ϕ and σ_y'' are the cohesion coefficient, friction angle and the effective yield limit stress respectively. The *Lode angle*, θ, is a function of the effective deviatoric stress (through its second $J_2(\mathbf{S}_{\sigma''})$ and third $(J_3(\mathbf{S}_{\sigma''}))$ invariants) defined as,

$$\theta = \theta(\mathbf{S}_{\sigma''}) \equiv \frac{1}{3}\sin^{-1}\left(\frac{-3\sqrt{3}\;J_3(\mathbf{S}_{\sigma''})}{2[J_2(\mathbf{S}_{\sigma''})]^{\frac{2}{3}}}\right) \tag{3.37}$$

where the third invariant reads:

$$J_3(\mathbf{S}_{\sigma''}) \equiv \det[\mathbf{S}_{\sigma''}] \tag{3.38}$$

Although the invariant representation of the Mohr-Coulomb yield function is often used in computational plasticity, its computational costs are higher and its numerical algorithm is more complex when compared to the

multi-surface representation. The multi-surface representation is expressed by means of six functions:

$$\begin{aligned}
\Phi_1(\boldsymbol{\sigma}'', c) &= \sigma_1'' - \sigma_3'' + (\sigma_1'' + \sigma_3'') \sin\phi - 2\, c \cos\phi \\
\Phi_2(\boldsymbol{\sigma}'', c) &= \sigma_2'' - \sigma_3'' + (\sigma_2'' + \sigma_3'') \sin\phi - 2\, c \cos\phi \\
\Phi_3(\boldsymbol{\sigma}'', c) &= \sigma_2'' - \sigma_1'' + (\sigma_2'' + \sigma_1'') \sin\phi - 2\, c \cos\phi \\
\Phi_4(\boldsymbol{\sigma}'', c) &= \sigma_3'' - \sigma_1'' + (\sigma_3'' + \sigma_1'') \sin\phi - 2\, c \cos\phi \\
\Phi_5(\boldsymbol{\sigma}'', c) &= \sigma_3'' - \sigma_2'' + (\sigma_3'' + \sigma_2'') \sin\phi - 2\, c \cos\phi \\
\Phi_6(\boldsymbol{\sigma}'', c) &= \sigma_1'' - \sigma_2'' + (\sigma_1'' + \sigma_2'') \sin\phi - 2\, c \cos\phi
\end{aligned} \tag{3.39}$$

each defining a plane in the stress space, which corresponds to a face in the Mohr-Coulomb pyramid represented in Figure 3.1.

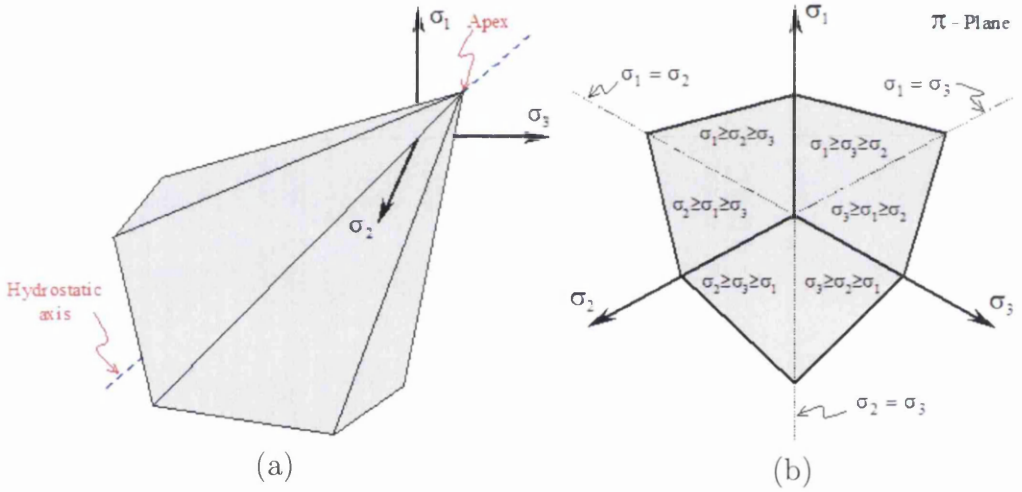

Figure 3.1: The Mohr-Coulomb yield criteria in principal stress space. (a) 3D yield surface. (b) Pi-plane cross section. [Klerck (2000)]

3.6 Solid-Seepage-Hydro-Fracture boundary value problem

The initial boundary value problem states that the momentum equilibrium equation (2.40) and the mass conservation equations (2.41) and (2.35) must be satisfied in all the domains Ω_u, Ω_{sf} and Ω_{nf} respectively. While the prescribed boundary conditions must be satisfied on the boundaries Γ_u, Γ_{sf} and Γ_{nf}. Depending on the kind of boundary condition, the boundaries Γ_u, Γ_{sf} and Γ_{nf} are separated by different regions. The part of the boundary where

prescribed displacement ($\tilde{u}$) and prescribed pressures ($\tilde{p}_{sf}$ and $\tilde{p}_{nf}$) exist are known as Dirichlet boundaries and denoted by $\partial\Gamma_u$, $\partial\Gamma_{sf}$ and $\partial\Gamma_{nf}$ respectively. On the other hand, the parts of $\partial\Gamma_u$, $\partial\Gamma_{sf}$ and $\partial\Gamma_{nf}$, where traction ($\mathbf{f}_t$) and flow ($\mathbf{Q}_{sf}$ and $\mathbf{Q}_{nf}$) are prescribed, are called natural boundaries and denoted by $\partial\Gamma_t$, $\partial\Gamma_{Q_{sf}}$ and $\partial\Gamma_{Q_{nf}}$ respectively. These conditions are written as:

$$\begin{aligned} u &= \tilde{u} \text{ in } \partial\Gamma_u \\ \boldsymbol{\sigma}\mathbf{n} &= \mathbf{f}_t \text{ in } \partial\Gamma_t \\ p_{sf} &= \tilde{p}_{sf} \text{ in } \partial\Gamma_{sf} \\ \mathbf{w}_{sf}\mathbf{n} &= \mathbf{Q}_{sf} \text{ in } \partial\Gamma_{Q_{sf}} \\ p_{nf} &= \tilde{p}_{nf} \text{ in } \partial\Gamma_{nf} \\ \mathbf{w}_{nf}\mathbf{n} &= \mathbf{Q}_{nf} \text{ in } \partial\Gamma_{Q_{nf}} \end{aligned} \tag{3.40}$$

In the solid deformation problem, traction and displacements can not be prescribed in the same region while, in fluid flow problems, pressures and flows can not be prescribed in the same region. On the other hand, the union of these regions defines the boundary of the problem:

$$\begin{aligned} \partial\Gamma_u \cap \partial\Gamma_t &= 0 \\ \partial\Gamma_u \cup \partial\Gamma_t &= \Gamma_u \\ \partial\Gamma_{sf} \cap \partial\Gamma_{Q_{sf}} &= 0 \\ \partial\Gamma_{sf} \cup \partial\Gamma_{Q_{sf}} &= \Gamma_{sf} \\ \partial\Gamma_{nf} \cap \partial\Gamma_{Q_{nf}} &= 0 \\ \partial\Gamma_{nf} \cup \partial\Gamma_{Q_{nf}} &= \Gamma_{nf} \end{aligned} \tag{3.41}$$

The initial boundary value problem in a coupled solid-seepage-hydrofracture problem is obtained through the introduction of the constitutive law discretized in time into the weak form of the momentum equilibrium equation. So, for a given set of internal variables, $\alpha_{k(n)}$, in time, $t_{(n)}$, and the external forces in time, $t_{(n+1)}$, i.e., $f_{1(n+1)}$, $f_{2(n+1)}$, $f_{3(n+1)}$ and $b_{(n+1)}$, find the kinematically admissible displacement and admissible pressures, such that,

$$\int_{\Omega_u} \left[(\breve{\boldsymbol{\sigma}}''(\boldsymbol{\alpha}_{k(n)}, \boldsymbol{\varepsilon}(\mathbf{u}_{(n+1)})) - \alpha p_{sf(n+1)} \mathbf{I}) : \boldsymbol{\nabla}_x \hat{u} - \rho \mathbf{b}_{(n+1)} \hat{u} \right] d\Omega_u + \int_{\Omega_u} \rho \ddot{\mathbf{u}}_{(n)} \hat{u} d\Omega_u - \int_{\Gamma_u} \mathbf{f}_{1(n+1)} \hat{u} d\Gamma_u = 0 \quad \forall \hat{u} \in \vartheta_u \tag{3.42}$$

$$\int_{\Omega_{sf}} \left[\left(\frac{\mathbf{k}}{\mu} \boldsymbol{\nabla}_x p_{sf(n+1)} \right) \cdot \boldsymbol{\nabla}_x \hat{p}_{sf} - \boldsymbol{\nabla}_x \cdot \left(\frac{\mathbf{k}}{\mu} \rho_f S_f \mathbf{b}_{(n+1)} \right) \hat{p}_{sf} \right] d\Omega_{sf} + \int_{\Omega_{sf}} \boldsymbol{\nabla}_x \cdot \left(\frac{\mathbf{k}}{\mu} \rho_f S_f \ddot{\mathbf{u}}_{(n)} \right) \hat{p}_{sf} d\Omega_{sf} + \int_{\Omega_{sf}} \alpha S_f \dot{\varepsilon}_{v(n+1/2)} \hat{p}_{sf} d\Omega_{sf} + \int_{\Omega_{sf}} \rho_f \frac{\dot{p}_{sf(n+1/2)}}{Q_{sf}} \hat{p}_{sf} d\Omega_{sf} - \int_{\Gamma_{sf}} f_{2(n+1)} \hat{p}_{sf} d\Gamma_{sf} = 0 \quad \forall \hat{p}_{sf} \in \vartheta_{p_{sf}} \tag{3.43}$$

$$\int_{\Omega_{nf}} \left[\left(\frac{e^2_{(n+1)}}{12\mu} \boldsymbol{\nabla}_x p_{nf(n+1)} \right) \cdot \boldsymbol{\nabla}_x \hat{p}_{nf} \right] d\Omega_{nf} - \int_{\Omega_{nf}} \left[\boldsymbol{\nabla}_x \cdot \left(\frac{e^2_{(n+1)}}{12\mu} \rho_f \mathbf{b}_{(n+1)} \right) \hat{p}_{nf} \right] d\Omega_{nf} + \int_{\Omega_{nf}} \boldsymbol{\nabla}_x \cdot \left(\frac{e^2_{(n+1)}}{12\mu} \rho_f \ddot{\mathbf{u}}_{(n)} \right) \hat{p}_{nf} d\Omega_{nf} + \int_{\Omega_{nf}} \dot{\varepsilon}_{v(n+1/2)} \hat{p}_{nf} d\Omega_{nf} + \int_{\Omega_{nf}} \rho_f \frac{\dot{p}_{nf(n+1/2)}}{Q_{nf}} \hat{p}_{nf} d\Omega_{nf} - \int_{\Gamma_{nf}} f_{3(n+1)} \hat{p}_{nf} d\Gamma_{nf} = 0 \quad \forall \hat{p}_{nf} \in \vartheta_{p_{nf}} \tag{3.44}$$

3.7 Discretization of the governing equations

We shall introduce a spatial approximation of the primary variables $\mathbf{u}$, $\mathbf{p}_{sf}$ and $\mathbf{p}_{nf}$ in the form

$$\begin{aligned} \mathbf{u} &\approx \mathbf{u}(t) = \mathbf{N}_u \bar{\mathbf{u}}(t) \\ \mathbf{p}_{sf} &\approx \mathbf{p}_{sf}(t) = \mathbf{N}_{p_{sf}} \bar{\mathbf{p}}_{sf}(t) \\ \mathbf{p}_{nf} &\approx \mathbf{p}_{nf}(t) = \mathbf{N}_{p_{nf}} \bar{\mathbf{p}}_{nf}(t) \end{aligned} \tag{3.45}$$

where, $\mathbf{N}_u$, $\mathbf{N}_{p_{sf}}$ and $\mathbf{N}_{p_{nf}}$ are 'basis' or 'shape' functions, which have to possess C_0 continuity, and $\bar{\mathbf{u}}$, $\bar{\mathbf{p}}_{sf}$ and $\bar{\mathbf{p}}_{nf}$ the nodal values of the interpolated variables.

The replacement of the primary variables with their spatial approximations transforms the initial boundary value problem defined in equations (3.42), (3.43) and (3.44) into a set of discrete equations in space with only time derivatives remaining. The resulting approximation is, for equation (3.42),

$$\int_{\Omega_u} (\nabla \mathbf{N}_u)^T \boldsymbol{\sigma}'' \, d\Omega_u - \mathbf{Q}\bar{\mathbf{p}}_{sf} + \mathbf{M}\ddot{\bar{\mathbf{u}}} = \bar{\mathbf{f}}_1, \tag{3.46}$$

for equation (3.43),

$$\mathbf{H}_{sf}\bar{\mathbf{p}}_{sf} + \mathbf{Q}_{sf}^{\mathbf{T}}\dot{\bar{\mathbf{u}}} + \mathbf{S}_{sf}\dot{\bar{\mathbf{p}}}_{sf} = \bar{\mathbf{f}}_2, \tag{3.47}$$

and for equation (3.44),

$$\mathbf{H}_{nf}\bar{\mathbf{p}}_{nf} + \mathbf{Q}_{nf}^{\mathbf{T}}\dot{\bar{\mathbf{u}}} + \mathbf{S}_{nf}\dot{\bar{\mathbf{p}}}_{nf} = \bar{\mathbf{f}}_3. \tag{3.48}$$

with the constitutive equation supplying the increments of σ''_{ij}.
In a linearized form the system reads

$$\begin{bmatrix} \mathbf{M} & \mathbf{0} & \mathbf{0} \\ \mathbf{0} & \mathbf{0} & \mathbf{0} \\ \mathbf{0} & \mathbf{0} & \mathbf{0} \end{bmatrix} \begin{bmatrix} \ddot{\bar{\mathbf{u}}} \\ \ddot{\bar{\mathbf{p}}}_{sf} \\ \ddot{\bar{\mathbf{p}}}_{nf} \end{bmatrix} + \begin{bmatrix} \mathbf{0} & \mathbf{0} & \mathbf{0} \\ \mathbf{Q}_{sf}^{\mathbf{T}} & \mathbf{S}_{sf} & \mathbf{0} \\ \mathbf{Q}_{nf}^{\mathbf{T}} & \mathbf{0} & \mathbf{S}_{nf} \end{bmatrix} \begin{bmatrix} \dot{\bar{\mathbf{u}}} \\ \dot{\bar{\mathbf{p}}}_{sf} \\ \dot{\bar{\mathbf{p}}}_{nf} \end{bmatrix} +$$

$$\begin{bmatrix} \mathbf{K} & -\mathbf{Q}_{sf} & \mathbf{0} \\ \mathbf{0} & \mathbf{H}_{sf} & \mathbf{0} \\ \mathbf{0} & \mathbf{0} & \mathbf{H}_{nf} \end{bmatrix} \begin{bmatrix} \bar{\mathbf{u}} \\ \bar{\mathbf{p}}_{\mathbf{s}} \\ \bar{\mathbf{p}}_{\mathbf{f}} \end{bmatrix} = \begin{bmatrix} \bar{\mathbf{f}}_1 \\ \bar{\mathbf{f}}_2 \\ \bar{\mathbf{f}}_3 \end{bmatrix} \tag{3.49}$$

with matrices and vectors defined below:

$$\mathbf{M} = \int_{\Omega_u} (\mathbf{N}_u)^T \rho \mathbf{N}_u d\Omega_u$$

$$\mathbf{K} = \int_{\Omega_u} (\nabla \mathbf{N}_u)^T \mathbf{D} \nabla \mathbf{N}_u d\Omega_u$$

$$\mathbf{Q}_{sf} = \int_{\Omega_{sf}} (\nabla \mathbf{N}_u)^T \alpha S_f \mathbf{m} \mathbf{N}_{p_{sf}} d\Omega_{sf}$$

$$\mathbf{S}_{sf} = \int_{\Omega_{sf}} (\mathbf{N}_{p_{sf}})^T \frac{1}{Q_{sf}} \mathbf{N}_{p_{sf}} d\Omega_{sf}$$

$$\mathbf{H}_{sf} = \int_{\Omega_{sf}} (\nabla \mathbf{N}_{p_{sf}})^T \frac{\mathbf{k}}{\mu} \nabla \mathbf{N}_{p_{sf}} d\Omega_{sf} \tag{3.50}$$

$$\mathbf{S}_{nf} = \int_{\Omega_{nf}} (\mathbf{N}_{p_{nf}})^T \frac{1}{Q_{nf}} \mathbf{N}_{p_{nf}} d\Omega_{nf}$$

$$\mathbf{Q}_{nf} = \int_{\Omega_{nf}} (\nabla \mathbf{N}_u)^T \mathbf{m} \mathbf{N}_{p_{nf}} d\Omega_{nf}$$

$$\mathbf{H}_{nf} = \int_{\Omega_{nf}} (\nabla \mathbf{N}_{p_{nf}})^T \frac{e^2}{12\mu} \nabla \mathbf{N}_{p_{nf}} d\Omega_{nf}$$

$$\mathbf{f}_1 = \int_{\Omega_u} (\mathbf{N}_u)^T \rho \mathbf{b} d\Omega_u + \int_{\Gamma_u} (\mathbf{N}_u)^T \bar{t} d\Gamma_u$$

$$\mathbf{f}_2 = -\int_{\Omega_{sf}} (\mathbf{N}_{p_{sf}})^T \nabla^T (\frac{\mathbf{k}}{\mu} S_f \rho_f \mathbf{b}) d\Omega_{sf} + \int_{\Omega_{sf}} (\mathbf{N}_{p_{sf}})^T \nabla^T (\frac{\mathbf{k}}{\mu} S_f \rho_f \ddot{\mathbf{u}}) d\Omega_{sf} + \int_{\Gamma_{sf}} (\mathbf{N}_{p_{sf}})^T \bar{q} d\Gamma_{sf}$$

$$\mathbf{f}_3 = -\int_{\Omega_{nf}} (\mathbf{N}_{p_{nf}})^T \nabla^T (\frac{e^2}{12\mu} \rho_f \mathbf{b}) d\Omega_f + \int_{\Omega_{nf}} (\mathbf{N}_{p_{nf}})^T \nabla^T (\frac{e^2}{12\mu} \rho_f \ddot{\mathbf{u}}) d\Omega_{nf} + \int_{\Gamma_{nf}} (\mathbf{N}_{p_{nf}})^T \bar{q} d\Gamma_{nf}$$

From the above system, it is not too clear that the mass conservation equation for the fluid in the fracture in the discretized form is coupled with the other two. However, it can be observed that:

1. The displacements provided by the equation (3.46) are affected by an external force caused by the fluid pressure in the fracture, which is applied as a traction boundary condition in the solid/fracture interface. On the other hand, the calculated displacements define the apertures in the existing fractures and the opening of new ones.

2. The coupling between the fluid flow in the seepage/fracture interface is made using a master/slave procedure. In this procedure the nodes in the hydraulic fractures are considered as master and the nodes of the seepage problem which are on the seepage/fracture interface are slaves. The mass matrices and the internal and external force vectors of the slaves are added into the master. Then, the equations of the slave nodes are modified by the ones related with the specific master nodes. Finally, the equations are solved and mass conservation is enforced on the interface. A more detailed description will be given in Chapter 4.

3.8 Time discretization

To complete the numerical solution it is necessary to integrate the ordinary differential equations (3.28), (3.46), (3.47) and (3.48), in time.

In the present work, a Central Difference method has been used due to its robustness and simplicity. In spite of its conditional stability, its use has been preferable compared to implicit schemes, mainly in problems involving contact and remeshing due to the need to include new fractures. This class of problems tend to exhibit difficult convergence characteristics for implicit methods, increasing the overall computational costs making it an unaffordable solution.

In the scheme we shall use the following notation. Let the time of the simulation $0 \leq t \leq t_E$ be subdivided into time steps Δt_n, $n = 1$ to n_{TS} where n_{TS} is the number of time steps and t_E is the end of the simulation. The superscript indicates that the time step: t^n, u^n and p^n are the time, displacement and pressure, respectively, at time step n.

We consider here an algorithm with a variable time step, which is necessary in most practical calculations since the stable time step is modified by mesh deformations and the wave speed changes caused by the effective stress [Belytschko et al. (2000)]. For this purpose, we define time increments by:

$$\Delta t^{n+1/2} = \frac{1}{2}\left(\Delta t^n + \Delta t^{n-1}\right) \tag{3.51}$$

Using the central difference formula to integrate equations (3.28), (3.46), (3.47) and (3.48) in time leads to

$$\ddot{\bar{\mathbf{u}}}^n = \frac{\bar{\mathbf{f}}_1^n - \left(\int_{\Omega_u} (\nabla \mathbf{N_u})^T \boldsymbol{\sigma}'' \, d\Omega_u\right)^n - \mathbf{Q}_{sf}\bar{\mathbf{p}}_{sf}^{n-1}}{\mathbf{M}^n}$$

$$\dot{\bar{\mathbf{u}}}^{n+1/2} = \dot{\bar{\mathbf{u}}}^{n-1/2} + \Delta t^{n+1/2}\ddot{\bar{\mathbf{u}}}^n \tag{3.52}$$

$$\bar{\mathbf{u}}^{n+1} = \bar{\mathbf{u}}^n + \Delta t^{n+1}\dot{\bar{\mathbf{u}}}^{n+1/2}$$

$$\dot{\bar{\mathbf{p}}}_{sf}^{n+1/2} = \frac{\bar{\mathbf{f}}_2^n - \mathbf{H}_{sf}\bar{\mathbf{p}}_{sf}^n + \mathbf{Q}_{sf}^T\dot{\bar{\mathbf{u}}}^{n+1/2}}{\mathbf{S}_{sf}^n} \tag{3.53}$$

$$\bar{\mathbf{p}}_{sf}^{n+1} = \bar{\mathbf{p}}_{sf}^n + \Delta t^{n+1}\dot{\bar{\mathbf{p}}}_{sf}^{n+1/2}$$

$$\dot{\bar{\mathbf{p}}}_{nf}^{n+1/2} = \frac{\bar{\mathbf{f}}_3^n - \mathbf{H}_{nf}\bar{\mathbf{p}}_{nf}^n + \mathbf{Q}_{nf}^T\dot{\bar{\mathbf{u}}}^{n+1/2}}{\mathbf{S}_{nf}} \tag{3.54}$$

$$\bar{\mathbf{p}}_{nf}^{n+1} = \bar{\mathbf{p}}_{nf}^{n} + \Delta t^{n+1} \dot{\bar{\mathbf{p}}}_{nf}^{n+1/2}$$

The overall implementation to solve the coupled problem is presented in the flowchart given in Box 3.1.

Box 3.1 - Flowchart for explicit time integration

1. Initial conditions and initialization: set $\dot{\mathbf{u}}^0$, $\dot{\boldsymbol{\sigma}}^0$, $\bar{\mathbf{p}}_{sf}^0$ and $\bar{\mathbf{p}}_{nf}^0$, and initial values of the constitutive model of the solid skeleton state variables;

$$\bar{\mathbf{u}}^0 = 0,\ n = 0,\ t = 0;\ \text{compute } \mathbf{M}^0,\ \mathbf{S}_{sf}^0,\ \mathbf{S}_{nf}^0$$

2. Calculate internal force vector ($\mathbf{f}_{int(1)}^n$, $\mathbf{f}_{int(2)}^n$ and $\mathbf{f}_{int(3)}^n$) and lumped mass matrices $\mathbf{M}^n$, $\mathbf{S}_{sf}^n$ and $\mathbf{S}_{nf}^n$

$$\mathbf{f}_{int(1)}^n = \left(\int_{\Omega_u} (\nabla \mathbf{N}_\mathbf{u})^T \boldsymbol{\sigma}'' \, d\Omega_u \right)^n - \mathbf{Q}_{sf} \bar{\mathbf{p}}_{sf}^n$$

$$\mathbf{f}_{int(2)}^n = \mathbf{H}_{sf} \bar{\mathbf{p}}_{sf}^n$$

$$\mathbf{f}_{int(3)}^n = \mathbf{H}_{nf} \bar{\mathbf{p}}_{nf}^n$$

$$\mathbf{M}^n = \left(\int_{\Omega_u} (\mathbf{N}_u)^T \rho^n \mathbf{N}_u \, d\Omega_u \right)^n$$

$$\mathbf{S}_{sf} = \left(\int_{\Omega_{sf}} (\mathbf{N}_{p_{sf}})^T \frac{1}{Q_{sf}^n} \mathbf{N}_{p_{sf}} \, d\Omega_{sf} \right)^n$$

$$\mathbf{S}_{nf} = \left(\int_{\Omega_{nf}} (\mathbf{N}_{p_{nf}})^T \frac{1}{Q_{nf}^n} \mathbf{N}_{p_{nf}} \, d\Omega_{nf} \right)^n$$

3. Compute Δt^e_{crit}, if $\Delta t^e_{crit} < \Delta t_{crit}$ then

$$\Delta t_{crit} = \Delta t^e_{crit}$$

4. Calculate external force vector ($\mathbf{f}^n_{ext(1)}$, $\mathbf{f}^n_{ext(2)}$ and $\mathbf{f}^n_{ext(3)}$).

$$\mathbf{f}^n_{ext(1)} = \int_{\Omega_u} (\mathbf{N}_u)^T \rho \mathbf{b} d\Omega_u + \int_{\Gamma_u} (\mathbf{N}_u)^T \bar{\mathbf{t}} d\Gamma_u + \int_{\Gamma_c} (\mathbf{N}_u)^T \bar{\mathbf{f}}_c d\Gamma_c$$

$$\mathbf{f}^n_{ext(2)} = -\int_{\Omega_{sf}} (\mathbf{N}_{p_{sf}})^T \boldsymbol{\nabla}^T \left(\frac{\mathbf{k}}{\mu} S_{sf} \rho_f \mathbf{b} \right) d\Omega_{sf} + \int_{\Gamma_{sf}} (\mathbf{N}_{p_s})^T \bar{\mathbf{q}} d\Gamma_{sf}$$

$$\mathbf{f}^n_{ext(3)} = -\int_{\Omega_{nf}} (\mathbf{N}_{p_{nf}})^T \boldsymbol{\nabla}^T \left(\frac{e^2}{12\mu} \rho_f \mathbf{b} \right) d\Omega_{nf} + \int_{\Gamma_{nf}} (\mathbf{N}_{p_f})^T \bar{\mathbf{q}} d\Gamma_{nf}$$

5. Time update.

$$t^{n+1} = t^n + \Delta t^{n+1}$$

$$t^{n+1/2} = \frac{1}{2}(t^n + t^{n+1})$$

$$\Delta t^{n+1/2} = \frac{\Delta t^{n+1} + \Delta t^n}{2}$$

6. Compute skeleton accelerations.

$$\ddot{\bar{\mathbf{u}}}^n = \frac{\bar{\mathbf{f}}^n_{ext(1)} - \bar{\mathbf{f}}^n_{int(1)}}{\mathbf{M}^n}$$

7. Compute skeleton velocities.

$$\dot{\bar{\mathbf{u}}}^{n+1/2} = \dot{\bar{\mathbf{u}}}^{n-1/2} + \Delta t^{n+1/2} \ddot{\bar{\mathbf{u}}}^n$$

8. Update nodal displacements.

$$\bar{\mathbf{u}}^{n+1} = \bar{\mathbf{u}}^n + \Delta t^{n+1} \dot{\bar{\mathbf{u}}}^{n+1/2}$$

9. Transfer coordinates from the structure to other fields. Update aperture (e) and volumetric strain rate ($\dot{\varepsilon}_v$) in the fracture and seepage fields respectively.

10. Add to the internal force vector ($\mathbf{f}^n_{int(2)}$) the contribution from the volumetric strain rate. Also, add to the external force vector ($\mathbf{f}^n_{ext(2)}$) the contribution from the structure acceleration.

$$\mathbf{f}^n_{int(2)} = \mathbf{Q}^T_{sf}\dot{\bar{\mathbf{u}}}^{n+1/2}$$

$$\mathbf{f}^n_{ext(2)} = \int_{\Omega_{sf}} (\mathbf{N}^{p_{sf}})^T \boldsymbol{\nabla}^T (\mathbf{k}\mathbf{S}_{sf}\ddot{\bar{\mathbf{u}}}^n) d\Omega_{sf}$$

11. Add contribution from slaves internal and external forces and specific storativity ($\mathbf{f}^n_{ext(2S)}$, $\mathbf{f}^n_{int(2S)}$, $\mathbf{S}^n_{sf(S)}$) to master internal and external forces and specific storativity ($\mathbf{f}^n_{ext(3M)}$, $\mathbf{f}^n_{int(3M)}$, $\mathbf{S}^n_{nf(M)}$) nodes.

$$\mathbf{f}^n_{ext(3M)} = \mathbf{f}^n_{ext(3M)} + \mathbf{f}^n_{ext(2S)}$$
$$\mathbf{f}^n_{int(3M)} = \mathbf{f}^n_{int(3M)} + \mathbf{f}^n_{int(2S)}$$
$$\mathbf{S}^n_{nf(M)} = \mathbf{S}^n_{nf(M)} + \mathbf{S}^n_{sf(S)}$$

12. Compute pressure rate to seepage and fracture fields.

$$\dot{\bar{\mathbf{p}}}^n_{sf} = \frac{\bar{\mathbf{f}}^n_{ext(2)} - \bar{\mathbf{f}}^n_{int(2)}}{\mathbf{S}^n_{sf}}$$

$$\dot{\bar{\mathbf{p}}}^n_{nf} = \frac{\bar{\mathbf{f}}^n_{ext(3)} - \bar{\mathbf{f}}^n_{int(3)}}{\mathbf{S}^n_{nf}}$$

13. Update nodal pressures to seepage and fracture fields.

$$\bar{\mathbf{p}}^{n+1}_{sf} = \bar{\mathbf{p}}^n_{sf} + \Delta t^{n+1}\dot{\bar{\mathbf{p}}}^{n+1/2}_{sf}$$

$$\bar{\mathbf{p}}^{n+1}_{nf} = \bar{\mathbf{p}}^n_{nf} + \Delta t^{n+1}\dot{\bar{\mathbf{p}}}^{n+1/2}_{nf}$$

14. Repeat items (3) and (4) to calculate internal and external force vectors at n+1.

3.8.1 Numerical stability

Explicit time integration schemes are well known to be conditionally stable, i.e., the time increment must not exceed a critical time step.

In general, the determination of a critical time step, Δt_{crit}, is based on the analysis of a linear system, and then, extrapolated to nonlinear cases by examining linearized models of nonlinear systems. A stable time step, Δt, is defined by Courant's condition for a mesh with constant strain element and rate-independent material as:

$$\Delta t = \alpha_t \Delta t_{crit}, \quad \Delta t_{crit} = \frac{2}{\omega_{max}} \equiv \min\left(l_{(e)}/c_{(e)}\right) \tag{3.55}$$

where α_t is a reduction factor that accounts for the destabilizing effects of non-linearities, ω_{max} is the maximum eigenvalue of the system, $l_{(e)}$ and $c_{(e)}$ are the characteristic length and the current wave speed in element (e) respectively.

The problems treated in this work are rate-dependent phenomena and contain a series of non-linearities which could lead to the solution error to growing unboundedly. A practical measure to reduce the instabilities caused by these factors is to introduce an extra reduction factor, Q_t, related to the artificial viscosity by,

$$Q_t = Q_l \; c_{(e)} - Q_q \; l_{(e)} \; \min(tr[\dot{\boldsymbol{\varepsilon}}], 0) \tag{3.56}$$

where, Q_l and Q_q are the linear and quadratic bulk viscosity and $tr[\dot{\boldsymbol{\varepsilon}}]$ is the volumetric strain rate. So, the final form for the critical time step can be written as:

$$\Delta t_{crit} = \frac{l_{(e)}}{Q_t + \sqrt{Q_t^2 + c_{(e)}^2}} \tag{3.57}$$

The coupling between three different fields (mechanical, seepage and network flow) requires that the choice of the critical time step must be based on the minimum critical time step from all fields,

$$\Delta t_{crit} = \min\left[\Delta t^u_{crit}, \Delta t^{sf}_{crit}, \Delta t^{nf}_{crit}\right] \tag{3.58}$$

where, $\Delta t^u_{crit}, \Delta t^{sf}_{crit} and \Delta t^{nf}_{crit}$ are the critical time step for the mechanical, seepage and network flow respectively.

The main difference in the calculation of the critical time for the three main fields is the definition of the wave speed, $c_{(e)}$, for each. Also, in the seepage and network fields it is necessary to take into account the influence of the volumetric load term as will be seen.

For the mechanical field, the critical time step is obtained from equation (3.57), where, the wave speed is defined for the plane stress case as:

$$c_{(e)} = \sqrt{\frac{E}{\rho\,(1-2\nu^2)}}\,, \tag{3.59}$$

and for the plane strain, axisymmetric and 3D cases as:

$$c_{(e)} = \sqrt{\frac{E(1-\nu)}{\rho(1+\nu)(1-2\nu)}} \tag{3.60}$$

where, E is the Young's Modulus, ν is the Poisson's ratio.

In seepage and network fields, the critical time step is influenced by an extra stiffness introduced in the system as a result of the volumetric load term. Therefore, the critical time step for the seepage and network flow respectively is obtained from:

$$\begin{aligned} \Delta t^{sf}_{crit} &= \min\left[\Delta t^{sf}_{crit(K)}, \Delta t^{sf}_{crit(V)}\right] \text{ and} \\ \Delta t^{nf}_{crit} &= \min\left[\Delta t^{nf}_{crit(K)}, \Delta t^{nf}_{crit(V)}\right] \end{aligned} \tag{3.61}$$

where, $\Delta t^{sf}_{crit(K)}$ and $\Delta t^{nf}_{crit(K)}$ are the critical time steps associated with the uncoupled stiffness of the fields, and, $\Delta t^{sf}_{crit(V)}$ and $\Delta t^{nf}_{crit(V)}$ are the critical time steps associated with the volumetric load term. These are defined as:

$$\begin{aligned} \Delta t^{sf}_{crit(K)} &= \frac{l^2_{(e)}\; Q_{sf}\; \mu}{2\; k^{(e)}_{min}} \\ \Delta t^{nf}_{crit(K)} &= \frac{6\; l^2_{(e)}\; Q_{nf}\; \mu}{e^2} \\ \Delta t^{sf}_{crit(V)} &= \frac{l_{(e)}}{Q_t + \sqrt{Q_t^2 + c^2_{v_{sf}(e)}}} \\ \Delta t^{nf}_{crit(V)} &= \frac{l_{(e)}}{Q_t + \sqrt{Q_t^2 + c^2_{v_{nf}(e)}}} \end{aligned} \tag{3.62}$$

In which $k^{(e)}_{min}$ is the lowest component of the element permeability. Finally, the wavespeed terms $c_{v_{sf}(e)}$ and $c_{v_{nf}(e)}$ are given by:

$$c_{v_{sf}(e)} = \sqrt{\frac{(E + E_{v_{sf}(e)})(1-\nu)}{\rho(1+\nu)(1-2\nu)}} \qquad (3.63)$$
$$c_{v_{nf}(e)} = \sqrt{\frac{(E + E_{v_{nf}(e)})(1-\nu)}{\rho(1+\nu)(1-2\nu)}}$$

The terms $E_{v_{sf}(e)}$ and $E_{v_{nf}(e)}$ are related to the extra stiffness added to the seepage and network flow fields respectively, and are defined as:

$$\begin{aligned} E_{v_{sf}(e)} &= 3\frac{Q_{sf}}{\alpha}\,(1-2\nu) \text{ and} \qquad (3.64) \\ E_{v_{nf}(e)} &= 3\,Q_{nf}\,(1-2\nu) \end{aligned}$$

3.9 Hourglass control

The efficiency and simplicity of the explicit time integration scheme are directly related with the use of one point quadrature elements. Although, it reduces substantially the computational costs when compared to a 2x2 quadrature in quadrilateral and 2x2x2 quadrature in hexahedral elements, undesirable mesh instabilities can occur due to spurious zero-energy modes. These modes lead to oscillatory solutions in which nodal pressures alternate in sign spatially, and the growth of these modes can cause disastrous results.

Several procedures have been developed in order to overcome this phenomenon in the last few decades. In particular, the work developed by Liu and Belytschko (1984) and Belytschko et al. (1984) have proven to be very attractive and has been used to solve problems with thermal applications. In this type of problem the governing equation is of a Laplacian form, which makes such a technique applicable to the problems treated in the present work. The method is shown to be very efficient and simple to implement. This has been the major reason for its adoption here.

In the procedure, the element conductivity matrix using a one-point quadrature, $\mathbf{K}_1^{(e)}$, is augmented by a stabilization matrix, $\mathbf{K}_{stab}^{(e)}$, which is orthogonal to all linear fields and its magnitude is determined by a stabilization parameter. In fact, the accuracy has been shown to be almost independent of the value of the stabilization parameter and a value equal to 1 is enforced in the present work, leading to the fully integrated finite element operator. A description of the implementation in quadrilateral elements is given below, while, in Appendix A the implementation procedure for hexahedral elements is provided.

The form of the augmented element conductivity matrix, $\mathbf{K}^{(e)}$, can be written as:

$$\mathbf{K}^{(e)} = \mathbf{K}_1^{(e)} + \mathbf{K}_{stab}^{(e)} \tag{3.65}$$

Expanding the pressure gradient,∇p, by a Taylor series:

$$\nabla p(\xi,\eta) = \mathbf{B}_a(0)p_a + \mathbf{B}_{a,\xi}(0)p_a\ \xi + \mathbf{B}_{a,\eta}(0)p_a\ \eta\ , \qquad a = 1,\ldots,4 \tag{3.66}$$

where, ξ and η are the natural coordinates of the bi-unit square and 0 denotes 'evaluated at $(\xi,\ \eta) = (0,0)$'; $\mathbf{B}_a$ are the generalized gradient operators of the shape functions N_a given by:

$$\begin{aligned} \mathbf{B}_a &= \begin{bmatrix} N_{a,x} \\ N_{a,y} \end{bmatrix} \quad \text{and} \\ N_a &= \frac{1}{4}(1+\xi_a)(1+\eta_a) \end{aligned} \tag{3.67}$$

then the general form of $\mathbf{K}_1^{(e)}$ and $\mathbf{K}_{stab}^{(e)}$ can be written as:

$$\begin{aligned} \mathbf{K}_1^{(e)} &= A\ \mathbf{B}_a^T(0)\ \frac{\mathbf{k}}{\mu}\ \mathbf{B}_b(0) \\ \mathbf{K}_{stab}^{(e)} &= \frac{1}{3}\ A\ \mathbf{B}_{a,\xi}^T(0)\ \frac{\mathbf{k}}{\mu}\ \mathbf{B}_{b,\xi}(0) + \frac{1}{3}\ A\ \mathbf{B}_{a,\eta}^T(0)\ \frac{\mathbf{k}}{\mu}\ \mathbf{B}_{b,\eta}(0) \end{aligned} \tag{3.68}$$

where, A is the area of the element. The computation of $\mathbf{K}_1^{(e)}$ requires the evaluation of $\mathbf{B}_a(0)$ gradient submatrices, which can be written explicitly as:

$$\mathbf{B}_a(0) = \begin{bmatrix} b_{1a} \\ b_{2a} \end{bmatrix}, \tag{3.69}$$

where,

$$\begin{aligned} \mathbf{b}_1 &= b_{1a} = \frac{1}{2A}[y_{24}, y_{31}, y_{42}, y_{13}]^T, \\ \mathbf{b}_2 &= b_{2a} = \frac{1}{2A}[x_{42}, x_{13}, x_{24}, x_{31}]^T, \\ x_{ab} &= x_a - x_b; \qquad y_{ab} = y_a - y_b \end{aligned} \tag{3.70}$$

and

$$A = \frac{1}{2}(x_{31}\ y_{42} + x_{24}\ y_{31}). \tag{3.71}$$

Finally, it is necessary to compute the $\mathbf{K}_{stab}^{(e)}$ submatrices, which requires the evaluation of $\mathbf{B}_{a,\xi}$ and $\mathbf{B}_{a,\eta}$ at the same quadrature point, namely '0'.

Denoting,

$$\begin{aligned} \mathbf{x} &= [x_1, x_2, x_3, x_4]^T; \\ \mathbf{y} &= [y_1, y_2, y_3, y_4]^T; \\ \boldsymbol{\xi} &= [-1, 1, 1, -1]^T; \\ \boldsymbol{\eta} &= [-1, -1, 1, 1]^T; \\ \mathbf{h} &= [1, -1, 1, -1]^T; \end{aligned} \tag{3.72}$$

where, $\mathbf{h}$ is known as the hourglass vector. After some algebra, the explicit expressions of the $\mathbf{B}^T_{a,\xi}(0)$ and $\mathbf{B}^T_{a,\eta}(0)$ submatrices can be shown to be:

$$\mathbf{B}_{a,\xi}(0) = \begin{bmatrix} b_{1,\xi a} \\ b_{2,\xi a} \end{bmatrix}; \qquad \mathbf{B}_{a,\eta}(0) = \begin{bmatrix} b_{1,\eta a} \\ b_{2,\eta a} \end{bmatrix}, \tag{3.73}$$

where,

$$\begin{aligned} \mathbf{b}_{1,\xi} &= b_{1,\xi a} = -\frac{\boldsymbol{\xi}^T \mathbf{y}}{4A}[\gamma_1, \gamma_2, \gamma_3, \gamma_4]^T, \\ \mathbf{b}_{2,\xi} &= b_{2,\xi a} = \frac{\boldsymbol{\xi}^T \mathbf{x}}{4A}[\gamma_1, \gamma_2, \gamma_3, \gamma_4]^T, \\ \mathbf{b}_{1,\eta} &= b_{1,\eta a} = \frac{\boldsymbol{\eta}^T \mathbf{y}}{4A}[\gamma_1, \gamma_2, \gamma_3, \gamma_4]^T \quad \text{and} \\ \mathbf{b}_{2,\eta} &= b_{2,\eta a} = -\frac{\boldsymbol{\eta}^T \mathbf{x}}{4A}[\gamma_1, \gamma_2, \gamma_3, \gamma_4]^T. \end{aligned} \tag{3.74}$$

The $\boldsymbol{\gamma}$-vector is obtained simply by partial differentiation and is related to $\mathbf{b}_1$ and $\mathbf{b}_2$ by:

$$\boldsymbol{\gamma} = \mathbf{h} - (\mathbf{h}^T \mathbf{x})\mathbf{b}_1 - (\mathbf{h}^T \mathbf{y})\mathbf{b}_2 \tag{3.75}$$

Finally, with the above definitions the augmented element matrix can be assembled by the summation of $\mathbf{K}^{(e)}_1$ and $\mathbf{K}^{(e)}_{stab}$, which guarantees a rank sufficient matrix.

In order to check the accuracy and efficiency of the overall implementation, a similar patch test to that used by Liu and Belytschko (1984) is evaluated.

3.9.1 Patch test problem

Patch-test problems have been used by several authors to evaluate the consistency of proposed procedures to eliminate hourglass modes.

In the present work, the example consists of a circular plate with fluid injected in the center at a constant pressure equal to 20 Pa and a no flow

boundary condition enforced on the outer radius. Due to its symmetry only a quarter of the problem needs to be solved. The radius of the plate is 5 metres and the thickness is 1 metre. Firstly, a plane strain analysis is carried out and then a fully 3D model is tested. The layout of the problem and input parameters are shown in Figure 3.2 and Table 3.1 respectively.

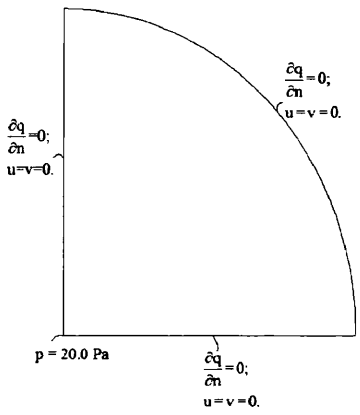

Figure 3.2: Layout of the problem.

Input parameters	
Young's modulus	1.3 MPa
Poisson	0.4
Fluid mass density	1000 Kg/m^3
Solid mass density	2000 Kg/m^3
Fluid bulk modulus	1.0 GPa
Grain bulk modulus	1.0 GPa
Fluid viscosity	0.001 Pa.s
Porosity	0.2975
Permeability	1.0e-10 m^2

Table 3.1: Input parameters.

The rank insufficiency of the conductivity matrix caused by one point quadrature in quadrilateral (2D) and hexahedral (3D) elements is responsible for spurious zero-energy modes, as can be seen in Figures 3.3(a) and 3.3(c). It can be noted that the nodal pressures are oscillating in different nodal positions on the plate between values of 0 and 20 Pa.

On the other hand, the use of a hourglass control procedure as described above to augment the conductivity matrix, overcomes this problem as shown in Figures 3.3(b) and 3.3(d). When a steady state is achieved, the nodal pressures in the whole plate are 20 Pa as expected.

The results have shown that the stabilization method used in the present work provides an efficient and accurate solution eliminating the hourglass modes in underintegrated elements.

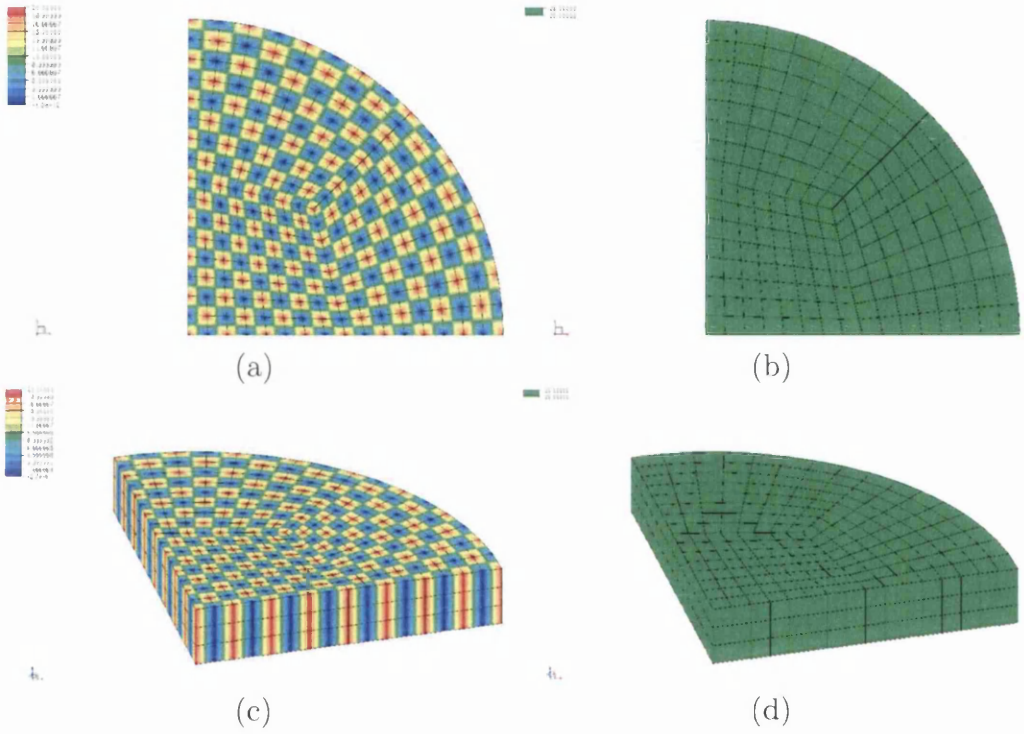

Figure 3.3: Nodal pressure plots in a 2D and 3D circular plate. (a) Hourglass modes in a 2D plate. (b) Hourglass modes have been eliminated in a 2D plate. (c) Hourglass modes in a 3D plate. (d) Hourglass modes have been eliminated in a 3D plate.

Chapter 4

Overall coupling procedure

A variety of computational models have been proposed in recent years to simulate hydraulic fracture flow in porous media. From a computational point of view, these are particularly very complex problems, since a strong coupling between the rock deformation, seepage flow and network flow exists. In order to tackle the problem, a finite element method is employed to discretize the governing equations which involve these three main fields and a central difference method is used for time integration.

The aim of the present chapter is to present a detailed description of the overall coupling procedure adopted, as a series of parallel developments have been made in order to optimize the solution procedure. Also, the advantages and disadvantages of a master-slave coupling procedure to link fluid flow between porous rock and hydraulic fracture is investigated.

In the following sections, some of the existing models are described together with some of their particular features. Then, a detailed description of the coupling procedure adopted in the present work is given. Finally, a numerical example to show the robustness of the model is presented.

4.1 Background

Hydraulic fracture flow in a porous medium involves the coupling of three main fields: structural, seepage and network. The inter-dependence of different phenomena are shown in Figure 4.1. In order to understand the complex interplay between the different phenomena, several approaches and theories have been proposed in the literature.

One strategy aims to model the flow through cracks without taking into account the flow within the material itself. This simplification is reasonable for soils or rock-like materials with low permeabilities, since the flow through

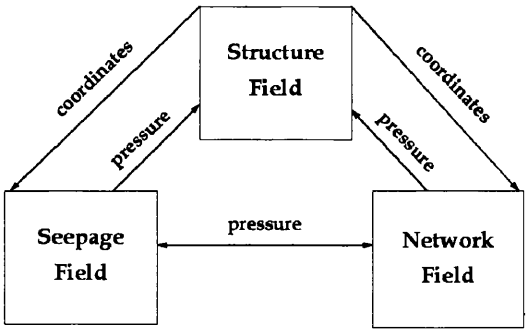

Figure 4.1: Coupling procedure.

the fractures is dominant. There are many models in the literature which have been developed to study fluid flow in a fractured network following this approach. In the simplest models, there is no interaction between structural and network fields. The fractures are considered to have constant aperture and length, as described in detail in Endo et al. (1984) and Smith and Schwartz (1984). Recent models, such as Papanastasiou (1997b) and Jing et al. (2001), are more realistic due to the fact that the hydro-mechanical coupling is considered.

However, an accurate analysis of the *in situ* stress field can only be obtained if the soil or rock-like material is treated as a porous medium. This is particularly noticeable for materials with high permeabilities where the seepage behaviour becomes prominent. In this case, the fluid flow through the fractured media is responsible for changes in the pore pressure and consequently modifies the *in situ* stress field.

The numerical models developed to date where leak-off effects have been considered can be classified into three main groups: effective continuum approximation, double porosity models and discrete fracture flow models.

The effective continuum approximation has been adopted in the work developed by Pruess et al. (1990). In this approach equivalent porous medium properties are based on intuitive notions for the behaviour of such systems and an insight gained from previous numerical simulations. They are acceptable for applications of large space and time scales where the rock matrix is highly permeable. However, a break down of this approach can be seen in processes involving rapidly transient conditions, very low permeability of the blocks and large fracture spacing.

Moench (1984) has adopted a double porosity concept to model the groundwater flow in a fractured porous medium. In these models, a fractured rock mass consists of primary porosity blocks (continuum of low permeabil-

ity) and secondary porosity fissures (continuum of high permeability). Each of these are characterized by their own porous medium properties, such as, porosity, compressibility and permeability. Also, it assumes that the flow in each continuum is governed by Darcy's law. The main shortcoming of this approach is that the porous matrix blocks are assumed to be of simple geometry with uniform size and shape.

The use of discrete fracture flow models seems particularly attractive. In this case, the flow through discontinuities is modelled using interface elements of zero-thickness. A number of works have been based on this approach, where the differences are related to the treatment of the transversal flow. Based on that, the models can be classified as: single, double and triple noded.

Single noded models are the most commonly used due to their simplicity, (see Figure 4.2 (a)). An existing continuum element mesh that accounts for the flow in the porous rock is superimposed by 'pipe' elements which represent the discretized fracture system. Consequently, specific storativities, internal and external forces at superimposed nodes are added, so that leak-off flux terms are balanced off and their explicit calculation is no longer required. The procedures developed by Sudicky and McLaren (1992) and Woodbury and Zhang (2001) have adopted this approach. Their results have yielded an accurate numerical solution to the problem of groundwater flow and solute transport. One of the limitations of using this model to link seepage and network flow fields is the fact that apertures are restricted to an initial fixed value due to a continuum mesh.

To circumvent problems where variations in apertures and potential drop between seepage and network flows play a crucial role in the analysis, double noded models have been developed by Ng and Small (1997), Segura and Carol (2004) and (2005) (Figure 4.2 (b)). In the most recent double-noded model proposed, longitudinal and transversal flows are obtained from the use of an auxiliary element on the interface mid-plane. First, the head jump between the two adjacent sides of the continuity is averaged. Then, longitudinal and transversal flows are calculated based on given longitudinal and transversal conductivities. Shortcomings of this approach are related to problems where potential drops are related with particle deposition, and a more sophisticated approach has to be adopted.

A more advanced approach has been proposed by Guiducci et al. (2002) (Figure 4.2(c)). In their triple noded model, a pipe element is used on the interface mid-plane to calculate longitudinal flow, and two transversal conductivities are defined in between the pipe and top and bottom continuum interfaces, so that transversal flows can be obtained through their head drops independently, without any assumptions. One of the major advantages of

this formulation in comparison with the others is that in complex problems where, for example, a filter cake is built-up in between the rock and continuum interface, a more realistic and accurate analysis can be performed with the use of this model, since the increase of the filter cake thickness will lead to a decrease in the aperture, consequently affecting the longitudinal flow along the fracture. An inconvenience is related to the computational cost due to an increase in the number of variables of the problem.

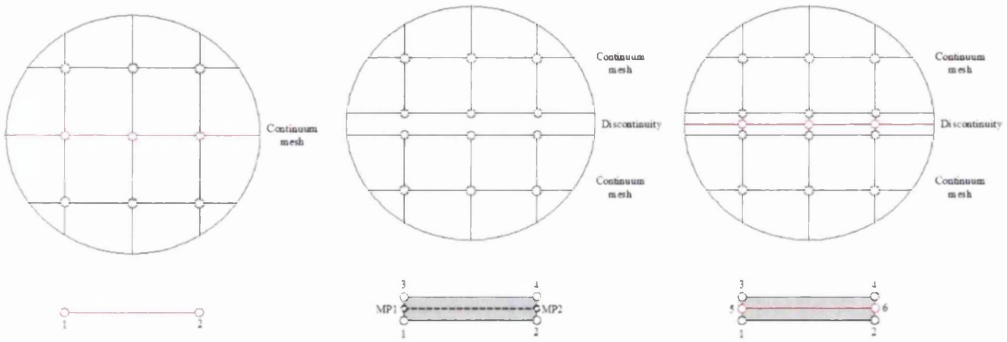

Figure 4.2: Zero thickness interface elements in a 2D continuum mesh. (a) Single-noded. (b) Double-noded. (c) Triple-noded.

4.2 Coupling between fields

One of the major difficulties with coupled problems is related to the management of the large amount of data transferred between fields and with the link between seepage and network flows.

In order to provide a better overview of the interaction between the fields, Subsections 4.2.1 and 4.2.2 will give a detailed description of the overall procedure. Special attention will be given to the link between seepage and network flows (Subsection 4.2.2), where an alternative approach is presented.

4.2.1 Links between structural, seepage and network flows

The links between structural, seepage and network flows are explicitly described by Equations (3.46), (3.47) and (3.48) respectively. These are well defined and the difficulties relate to the management of the data transfer.

From the numerical point of view, the updated coordinates given by the displacements, which were calculated from the previous pore pressure in the

rock, fluid pressure in the fracture, mass, internal and external forces, are passed to the seepage field and network fields. With the new coordinates, volumetric strain rates are obtained for seepage and network fields using a midpoint rule. Together with the specific storativities, internal and external forces, a new pore pressure in the rock and fluid pressure in the fracture are calculated. A detailed description is given in Box 4.1.

Box 4.1 - Link between structural, seepage and network flows.

1. Given the previous pore pressure in the rock ($\mathbf{p}^n_{(sf)}$), fluid pressure in the fracture ($\mathbf{p}^n_{(nf)}$), mass ($\mathbf{M}^n$), internal ($\mathbf{f}^n_{int(u)}$) and external forces ($\mathbf{f}^n_{ext(u)}$). Compute accelerations ($\ddot{\mathbf{u}}^{\mathbf{n}}$) to the structural field.

$$\ddot{\mathbf{u}}^n = \frac{\mathbf{f}^n_{ext(u)} + \int_{\Gamma_u}(\mathbf{N}_u)^T\mathbf{p}^n_{(nf)}d\Gamma_u - \mathbf{f}^n_{int(u)} + \mathbf{Q}_{sf}\mathbf{p}^n_{(sf)}}{\mathbf{M}^n}$$

   where, n is the n^{th} increment, $\mathbf{N}_u$ are the shape functions, $\mathbf{M}^n$ and $\mathbf{Q}_{sf}$ are defined in Eq. 3.50.

2. Compute new velocities ($\dot{\bar{\mathbf{u}}}^{n+1/2}$) to the structure field.

$$\dot{\bar{\mathbf{u}}}^{n+1/2} = \dot{\bar{\mathbf{u}}}^{n-1/2} + \Delta t^{n+1/2}\ddot{\bar{\mathbf{u}}}^n$$

3. Update nodal displacements ($\bar{\mathbf{u}}^{n+1}$) and coordinates ($\mathbf{x}^{n+1}$).

$$\bar{\mathbf{u}}^{n+1} = \bar{\mathbf{u}}^n + \Delta t^{n+1}\dot{\bar{\mathbf{u}}}^{n+1/2}$$

$$\mathbf{x}^{n+1} = \mathbf{x}^n + \bar{\mathbf{u}}^{n+1}$$

4. Given new coordinates, calculate volumetric strain rates of seepage ($\dot{\varepsilon}_{v(sf)}$) and network ($\dot{\varepsilon}_{v(nf)}$) fields as:

$$\dot{\varepsilon}^{n+1/2}_{v(sf)} = \frac{2}{\Delta t^{n+1}}\left(\frac{V^{n+1}_{(sf)} - V^n_{(sf)}}{V^{n+1}_{(sf)} + V^n_{(sf)}}\right)$$

$$\dot{\varepsilon}^{n+1/2}_{v(nf)} = \frac{2}{\Delta t^{n+1}}\left(\frac{V^{n+1}_{(nf)} - V^n_{(nf)}}{V^{n+1}_{(nf)} + V^n_{(nf)}}\right)$$

5. Compute pressure rate for seepage and network fields.

$$\dot{\bar{\mathbf{p}}}^n_{sf} = \frac{\bar{\mathbf{f}}^n_{ext(sf)} - \bar{\mathbf{f}}^n_{int(sf)} + \mathbf{Q}^T_{sf}\ \dot{\varepsilon}^{n+1/2}_{v(sf)}}{\mathbf{S}^n_{sf}}$$

$$\dot{\bar{\mathbf{p}}}^n_{nf} = \frac{\bar{\mathbf{f}}^n_{ext(nf)} - \bar{\mathbf{f}}^n_{int(nf)} + \mathbf{Q}^T_{nf}\ \dot{\varepsilon}^{n+1/2}_{v(nf)}}{\mathbf{S}^n_{nf}}$$

6. Update nodal pressures to seepage and network fields.

$$\bar{\mathbf{p}}^{n+1}_{sf} = \bar{\mathbf{p}}^n_{sf} + \Delta t^{n+1}\dot{\bar{\mathbf{p}}}^n_{sf}$$

$$\bar{\mathbf{p}}^{n+1}_{nf} = \bar{\mathbf{p}}^n_{nf} + \Delta t^{n+1}\dot{\bar{\mathbf{p}}}^n_{nf}$$

4.2.2 Seepage-Network flows

The use of zero-thickness interface elements to model the longitudinal flow in the fracture has lead to the development of double noded and triple noded formulations that includes transversal flow effects. These models are particularly attractive in simulations of more complex problems where, for instance, a potential drop between seepage and network flow exists. However, the computational costs in these models are higher, due to an increase in the number of unknowns to be determined.

As a first approach to the problems that the present work is aimed at, the potential drop between the fields will be neglected. So that, in the interface between porous rock and a fracture, the fluid pressure is unique, i.e., it must satisfy the pressure fields in both seepage and network fields. Therefore, the use of a triple-noded formulation mixed with the superimposed nodal assumption from the single-noded scheme seems to be particularly attractive from a computational cost point of view, since the number of variables to be solved will be reduced from six or four from standard triple-noded and double-noded 2D formulations respectively to just two; this difference is even larger in 3D formulations.

The new method proposed in the present work to satisfy the above conditions is to use a master-slave procedure to link seepage and network flows. This method is particularly attractive due to its simplicity, efficiency and robustness, as will be demonstrated by the numerical examples. In the proposed method, a discontinuity is discretized using 'pipe' elements to calculate longitudinal flows. The nodes in these elements, as a matter of choice, will

be considered master (M), but equally it could be either the nodes belonging to bottom (b) or top (t) interfaces of the porous rock. Consequently, nodes located in the porous rock interface are assumed as slaves (S), as show in Figure 4.3.

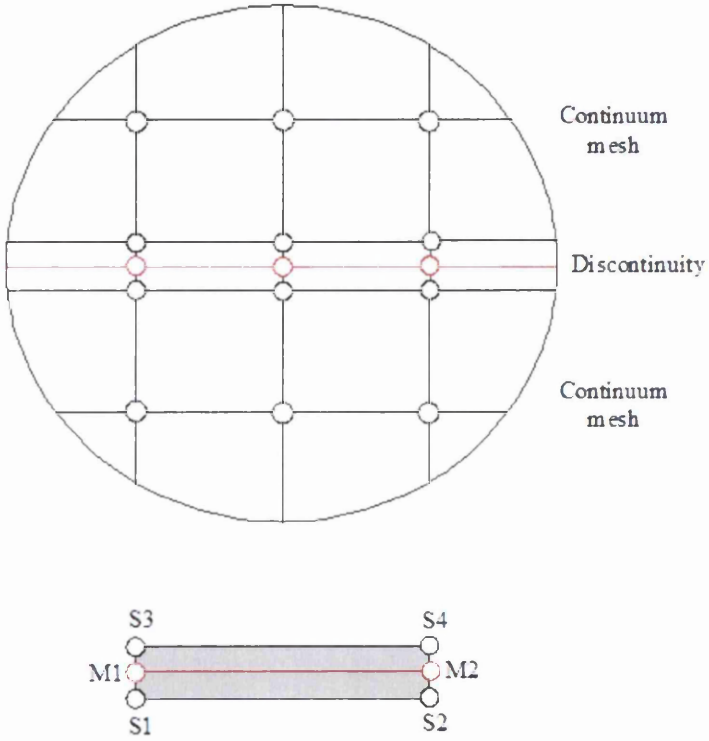

Figure 4.3: Master-slave procedure to link seepage and network flows in a 2D continuum mesh.

In a similar form to the single noded approach, specific storativities ($\mathbf{S}$), leak-off flux ($\mathbf{Q}_{lo}$), internal ($\mathbf{f}_{int}$) and external ($\mathbf{f}_{ext}$) forces from slaves nodes are added into master nodes. From a mathematical point of view, it can be expressed as:

$$\begin{aligned}
\mathbf{S}^{M}_{(nf)} &= \mathbf{S}^{M}_{(nf)} + \mathbf{S}^{S(t)}_{(sf)} + \mathbf{S}^{S(b)}_{(sf)} \\
\mathbf{f}^{M}_{int(nf)} &= \mathbf{f}^{M}_{int(nf)} + \mathbf{f}^{S(t)}_{int(sf)} + \mathbf{f}^{S(b)}_{int(sf)} \\
\mathbf{f}^{M}_{ext(nf)} &= \mathbf{f}^{M}_{ext(nf)} + \mathbf{f}^{S(t)}_{ext(sf)} + \mathbf{f}^{S(b)}_{ext(sf)} \\
\mathbf{Q}^{M}_{lo(nf)} &= \mathbf{Q}^{-M}_{lo(nf)} + \mathbf{Q}^{+S(t)}_{lo(sf)} + \mathbf{Q}^{+S(b)}_{lo(sf)} = 0
\end{aligned} \tag{4.1}$$

As can be seen from the equations described above, leak-off flux terms

are balanced off and their explicit calculation is no longer required. Also, it can be noted that, a reduction in the number of equations occurs, since equations related to slaves nodes do not need to be solved. The pressures are calculated only for master nodes and then prescribed to slaves nodes, respecting an unique pressure condition in the interface between seepage and network fields.

4.3 Explicit-explicit subcycling scheme

Explicit methods are attractive due to their simplicity in advancing the solution without solving a system of equations. However, their time increment are restricted to small values, i.e., they are conditionally stable.

On the other hand, with implicit methods large time steps can be achieved due to their unconditionally stable condition, but a large memory is required, since, a matrix system must be solved every time step causing a significant computational cost per step. Also, in problems where fracture initiation and propagation, contact, adaptivity and remeshing are present, convergence may become effectively impossible making the procedure inadequate for this class of problems.

In order to tackle these difficulties two major solutions have been proposed. The first one is the so-called "implicit-explicit" methods proposed by Belytschko and Mullen (1978), Hughes and Liu (1978b) and Hughes and Liu (1978a), in which the computational domain is partitioned into two parts and implicit or explicit methods are applied to each part according to its "stiffness". The second alternative approach is an explicit-explicit subcycling proposed by Mizukami (1986) and Neal and Belytschko (1989), in which the elements or nodes are separated into groups with different time step limit in each group. The group associated with the stiffer part is integrated with a time increment Δt, while the other part with a greater time increment $m\ \Delta t$ $(m > 1)$.

Therefore, the use of an explicit-explicit subcycling scheme seems particularly attractive. Since problems involving contact, fracture initiation and propagation are of interest here.

In the calculation of a critical time step using equations (3.57) and (3.62), it can be noted that mass density and Young's Modulus of the skeleton, permeability, storativity and viscosity of seepage and network fields, element size and volumetric strains are the parameters which determine the size of the time increment.

In the problems investigated so far, it has been noted that only small changes in the critical time step of the structural fields have occurred. On

the other hand, in problems where large increases in apertures takes place or the rock is highly permeable, the critical time steps have been controlled by the time increment related to the network and seepage fields respectively. In the fracture, the permeability and storativity are functions of the aperture as described in Eqs. (2.36) and (2.37). As can be seen in Figure 4.4, an increase in aperture means a quadratic increase in the permeability of the fracture and an asymptotic reduction in its storativity. Consequently, a dramatic decrease in the critical time step occurs as shown in Figure 4.5. In the seepage field, not many changes are seen during the advance of the analysis, but the permeability and storativity of the rock are crucial in defining the size of the time increment.

In the explicit-explicit subcycling procedure proposed, the overall analysis has been divided into two main parts. The first part is associated with the structural analysis which normally exhibits a large time increment ($\Delta t_{(u)}$). The other part relates to seepage and network fields with a small time increment ($min(\Delta t_{(sf)}, \Delta t_{(nf)})$). In seepage and network analysis the only term which is directly related with the change of the structure time increment is the volumetric strain rate. Therefore, the following procedure described in Box 4.2 can easily be adopted.

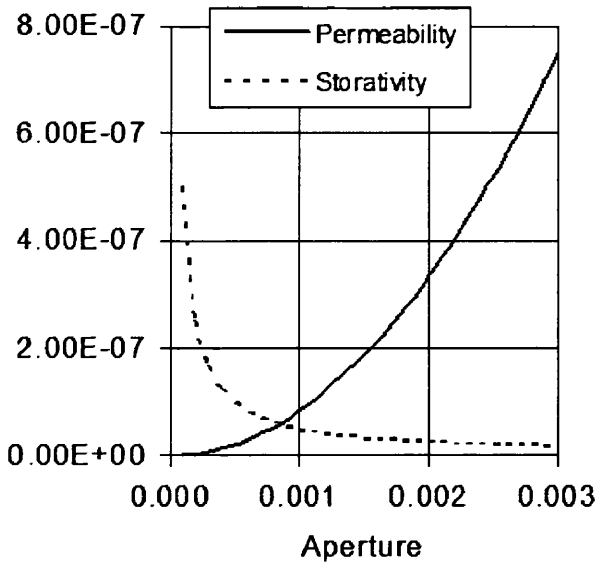

Figure 4.4: Intrinsic permeability and storativity of the fracture as a function of the aperture.

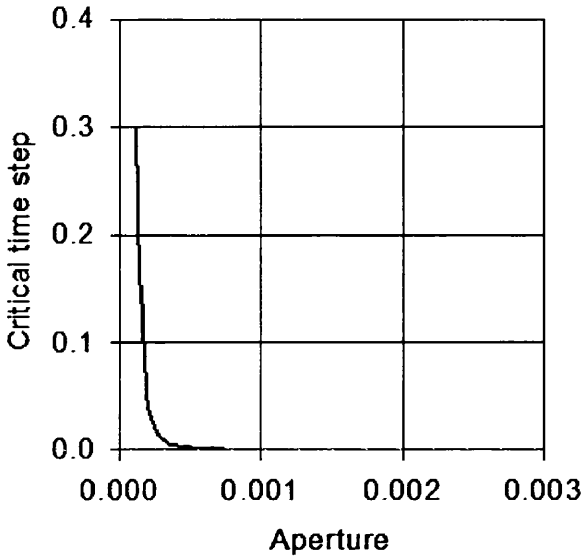

Figure 4.5: Critical time step as a function of the aperture.

Box 4.2 - Flowchart for explicit-explicit subcycling scheme.

1. Given the new displacements obtained at $t_{(u)}^{n+1}$, calculate the volumetric strain rate of seepage ($\dot{\varepsilon}_{v(sf)}$) and network ($\dot{\varepsilon}_{v(nf)}$) fields during a time increment ($\Delta t_{(u)}$) as:

$$\dot{\varepsilon}_{v(sf)}^{n+1/2} = \frac{2}{\Delta t_{(u)}} \left(\frac{V_{(sf)}^{n+1} - V_{(sf)}^{n}}{V_{(sf)}^{n+1} + V_{(sf)}^{n}} \right)$$

$$\dot{\varepsilon}_{v(nf)}^{n+1/2} = \frac{2}{\Delta t_{(u)}} \left(\frac{V_{(nf)}^{n+1} - V_{(nf)}^{n}}{V_{(nf)}^{n+1} + V_{(nf)}^{n}} \right)$$

where, n is the n^{th} increment, $V_{(sf)}$ and $V_{(nf)}$ are the volumes of seepage and network fields respectively.

2. Obtain the minimum time increment between seepage ($\Delta t_{(sf)}$) and network ($\Delta t_{(nf)}$) fields,

$$\Delta t_{(snf)} = min(\Delta t_{(sf)}, \Delta t_{(nf)})$$

3. Check if subcycling is necessary,

$$IF\ ((\Delta t_{(u)} - \Delta t_{(snf)}) > TOL)\ SUBCYCLING\ is\ TRUE$$

4. Initialize subcycling loop;
   a) Calculate the volumetric strain for seepage ($\varepsilon_{v(sf)}$) and network ($\varepsilon_{v(nf)}$) fields, as:

$$\varepsilon_{v(sf)}^{n+\Delta t_{(snf)}} = \Delta t_{(snf)} \dot{\varepsilon}_{v(sf)}^{n+1/2}$$

$$\varepsilon_{v(nf)}^{n+\Delta t_{(snf)}} = \Delta t_{(snf)} \dot{\varepsilon}_{v(nf)}^{n+1/2}$$

   b) Given internal forces ($f_{int(sf)}^{n}$, $f_{int(nf)}^{n}$), external forces ($f_{ext(sf)}^{n}$, $f_{ext(nf)}^{n}$) and storativities ($S_{(sf)}^{n}$, $S_{(nf)}^{n}$) for seepage and network fields, calculate the pore pressure in the rock $p_{(sf)}^{n+\Delta t_{(snf)}}$ and fluid pressure in the fracture $p_{(nf)}^{n+\Delta t_{(snf)}}$.

   c) Calculate for the next increment internal forces ($f_{int(sf)}^{n+\Delta t_{(snf)}}$, $f_{int(nf)}^{n+\Delta t_{(snf)}}$), external forces ($f_{ext(sf)}^{n+\Delta t_{(snf)}}$, $f_{ext(nf)}^{n+\Delta t_{(snf)}}$) and storativities ($S_{(sf)}^{n+\Delta t_{(snf)}}$, $S_{(nf)}^{n+\Delta t_{(snf)}}$) for seepage and network fields.

   d) Update time ($t_{(snf)}$) and check if this is the last subcycling increment ($\Delta t_{(snf)}^{n+1}$).

$$t_{(snf)}^{n+\Delta t_{(snf)}} = t_{(snf)}^{n} + \Delta t_{(snf)}$$

$$IF\ \Delta t_{(snf)}^{n+1}\ GOTO\ (e)$$

$$IF\ ((t_{(u)} - t_{(snf)}^{n+\Delta t_{(snf)}}) < TOL)\ \Delta t_{(snf)}^{n+1}\ is\ TRUE$$

$$\Delta t_{(snf)}^{n+1} = t_{(u)} - t_{(snf)}$$

   e) End of subcycling loop.

4.4 Numerical results

In order to shown the robustness and efficiency of the overall coupling procedure a dynamic filtration test will be solved. This problem is particularly appropriate to check whether mass conservation of the system is satisfied. Also, it will demonstrate the advantages of the proposed subcycling scheme.

4.4.1 Dynamic Filtration

The following example consists of pumping fluid through a pre-existing fracture and allowing the fluid to drain through the top and bottom surface of the two rock masses, as shown in Figure 4.6. Vertical displacements are prescribed on the top and bottom surfaces of the blocks and horizontal displacements are neglected at the lateral faces.

A 2D plane strain analysis is investigated. A linear elastic model is adopted and blocks have dimension of 5 x 20 metres and thickness of 1 metre. Also, top and bottom blocks exhibit different intrinsic permeabilities of 50 and 500 Darcys respectively. These values are artificially chosen for very highly permeable soils, but it makes steady state conditions achievable in a very short time. The fluid injected is water at a flow rate of 0.005 m^3/s and a viscosity of 0.001 Pa.s. The initial aperture is 0.2 millimetres along the whole fracture length. A detailed description of the parameters used in the example is given in Table 4.1.

Injected flow is compared against outflow to check mass balance. Also, apertures and pressures are recorded during the process. Finally, a comparison of CPU times with and without subcycling is made.

Input data	Value
Young's modulus	0.2 GPa
Poisson ratio	0.25
Bulk modulus of the grain	31.0 GPa
Bulk modulus of the fluid	2.0 GPa
Normal stiffness of the fracture	20.0 GPa/m
Dynamic viscosity of the fluid	0.001 Pa.s
Residual aperture	0.2 mm
Initial fluid pressure	0.0 Pa
Grain mass density	2500 kg/m^3
Fluid mass density	1000 kg/m^3

Table 4.1: Input data for dynamic filtration test.

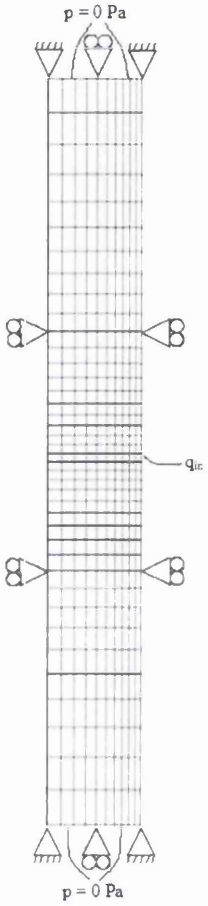

Figure 4.6: Layout of the dynamic filtration test.

In Figure 4.7(a), the flux in is compared with the flux out. As the analysis reaches a steady state it is possible to verify a match between the fluxes. Also, the ratio between flux coming out at the top and bottom faces are exactly as expected, since they have the same magnitude as the ratio between top and bottom permeability.

A good agreement has been observed in the volume check shown in Figure 4.7(b). The volume of injected fluid is in balance with the volume leaving the system, confirming that mass conservation is satisfied.

The aperture profile of the fracture at the injection point (5 metres) is given in Figure 4.7(c). An increase in the aperture is noticed until a steady state condition is reached, then no further major changes are seen.

Figure 4.7(d) presents pressure profiles from different points in the fracture. The fracture points are located at distances along the fracture length

from left (0 m) to right (5 m). High pressures have been observed closest to the injected point (5 m). Further from this point, they start to decrease due to leak-off effects.

Finally, a significant reduction in the computational cost can be seen through the use of the subcycling coupling scheme proposed. CPU times have been reduced from 394 minutes to 63 minutes.

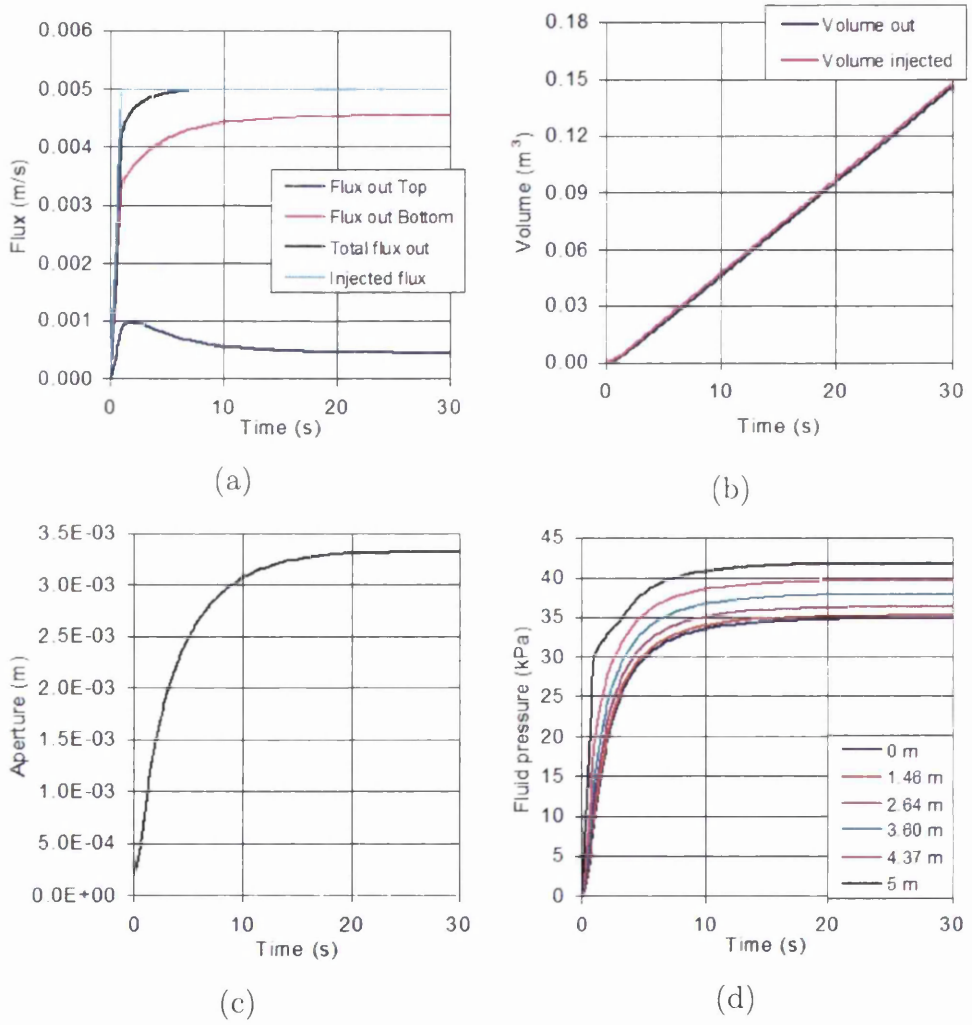

Figure 4.7: Dynamic filtration results for 2D plane strain analysis: (a) Flux balance. (b) Volume check. (c) Aperture profile in the fracture. (d) Fluid pressure profile in the fracture.

Chapter 5

Oil production

In recent years, massive investments have been made by oil producers in order to optimise the cost of oil extraction. Part of the efforts has been used in the development of numerical simulation schemes, as these have shown to be a powerful tool to assist analysts to have a better understanding of the mechanisms involved in such processes.

Although there is a wide range of applications in oil production where computational models could be used, the present work is particularly directed at hydraulic fractures in porous rock. Firstly, a brief description of the recent studies that are related to the topic will be given. Then, an explanation of the overall procedure and mechanisms involved in the propagation of a hydraulic fracture will follow. Finally, numerical examples will be presented and compared against experimental and field data.

5.1 Background

The decreasing rate in the production of oil from a well or a field in time is caused by the reduction of the natural energy that forces the oil through the subsurface reservoir and into the well. According to Hyne (2001), the ultimate recovery of oil from reservoirs varies from 5% to 80% but average only 30%. This means that 70% of the oil still remains in the pressure depleted reservoir.

In order to reduce the losses and extract some of the remaining oil from the oilfields there are a large variety of methods normally used in these situations such as, waterflood, enhanced oil recovery and others. The waterflood process consists of pumping water under pressure down the injection wells to force some of the remaining oil through the reservoir toward the producing wells, as show in Figure 5.1. Enhanced oil recovery works in a similar form, but

instead of using water, a non-natural fluid, such as carbon dioxide or steam, is used in order to increase the production.

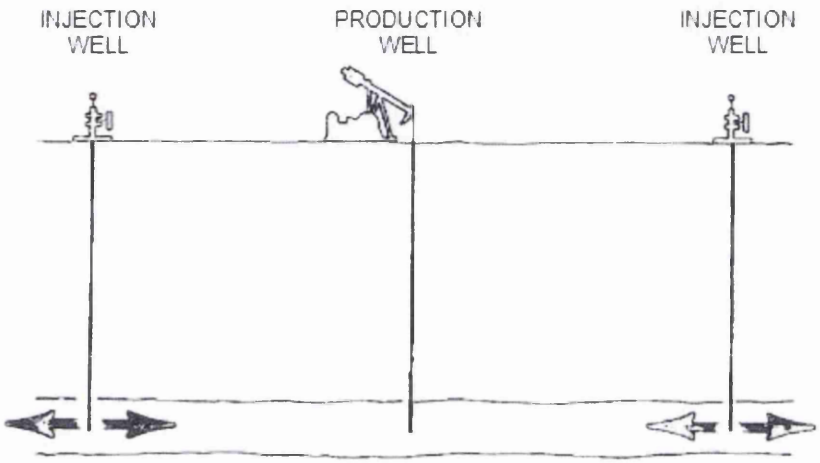

Figure 5.1: Waterflood (Hyne (2001)).

Hydraulic fracturing has been first applied in the oil industry in 1948 to increase the productivity of oil-bearing formations with low permeability, Atkinson (1987). Since then, it has been used in water well and gas stimulation, geothermal energy extraction to induce heat exchange surfaces, in coal gasification pilot projects, and for in *situ* stress measurements. It consists of pumping water or some other non-viscous fluid with some additives in sealed-off boreholes to generate new fractures and to open existing ones. These kinds of applications are the ones at which the present work is particularly aimed at, using the numerical tools which have been developed as explained in detail in Chapter 4.

There are a large number of approximations which have been proposed in the last few decades to estimate the pressure values necessary to induce and propagate tensile fractures, and to predict the final length and width of the fractures. These can be divided into two main groups: analytical and numerical models. A literature review of some of the main models existing in each area will follow summarising their limitations and assumptions.

Most analytical solutions have been based on simplified geometrical conditions, since a closed three-dimensional solution for the general complex problem is not yet available. The three main approaches using simplified approximations which yield two-dimensional models are:

- *Plane strain or KGD model* - has been introduced by Khristianovic and Zheltov (1955) and Geerstma and de Klerk (1969). In this model

the fracture propagation and deformation are assumed to evolve in a plane strain situation where the fracture geometry is shown in Figure 5.2. Also, the fluid flow and fracture propagation are one-dimensional.

- *PKN model* - is very similar to the above model. The main difference is associated with the fracture geometry. It assumes that the fracture has constant height and elliptic cross-section, as can be seen in Figure 5.3. Also, each vertical cross-section is deforming under plane strain conditions which implies that the lateral stiffness in the fracture length direction is ignored. This model has been developed by Perkins and Kern (1961) and Nordgren (1972).

- *Penny-shape or radial model* - has been firstly solved by Sneddon (1946) considering a constant fluid pressure. It is applicable to a homogeneous reservoir where the injection region is practically a point source, i.e., the wellbore radius is negligible compared to the fracture radius, as shown in Figure 5.4.

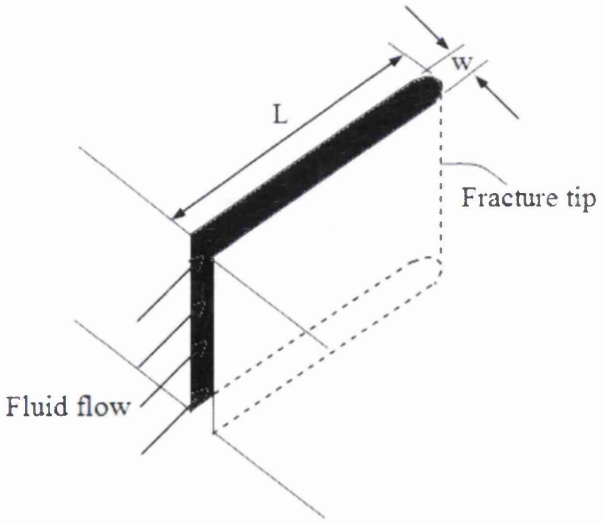

Figure 5.2: Plane strain model.

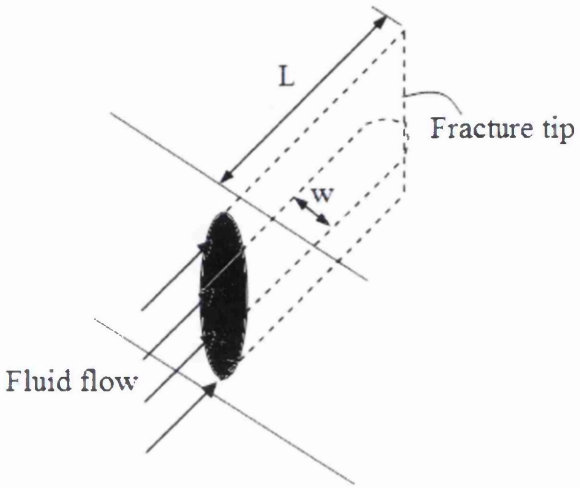

Figure 5.3: PKN model.

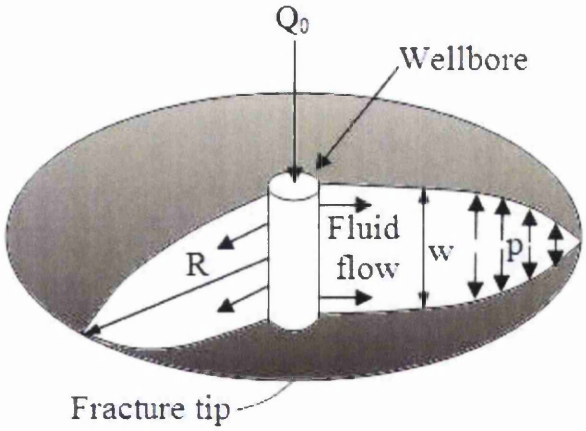

Figure 5.4: Penny-shaped or radial model.

Based on these simplified geometrical conditions, several analytical models have been formulated. Detournay et al. (1990) have derived a mathematical formulation based on the PKN model considering poroelastic effects induced by leak-off of the fracturing fluid. Then, an explicit finite difference scheme has been used to solve the system of equations containing six unknown variables: pressure, width, leak-off velocity, length, flow rate per unit of length and fracture arrival time at a point. Comparison of a permeable and impermeable rock has been investigated and the results have suggested that a poroelastic process could be responsible for a significant increase of the fracture pressure, but has little influence on the geometry of the fracture (width and length) as a consequence of assuming a leak-off formula which is pressure independent.

In a parallel development with the previous work, Detournay and Cheng (1991) presented a plane strain analysis of a constant length hydraulic fracture embedded in an infinite poroelastic domain. The uniform load in the crack walls caused by the injection of fluid is decomposed into two modes, consisting of a unit step for the normal stress and a unit step for the pore pressure along the fracture. The results also have pointed out that a higher hydraulic fracturing pressure is predicted when poroelasticity effects are incorporated. In addition to that, the leak-off volume calculated via poroelasticity theory has been shown to be nearly identical to that computed by the diffusion equation, as the fracturing fluid is assumed to be identical to that of the reservoir.

A more recent analysis of the propagation regimes of a penny-shaped hydraulic fracture in an impermeable elastic rock has been carried out by Savitski and Detournay (2002). They have developed an analytical solution based on a dimensionless crack opening, net pressure and fracture propagation radius obtained through a scaling procedure. The final form of the scaled equations has indicated that the regimes of fracture propagation are controlled by only one parameter, a dimensionless toughness. The results have shown that fracture propagation can be dominated by three different regimes. The two extremes regimes, i.e. dimensionless toughness equal to zero and equal to infinity, are defined by the viscosity-dominated regime and toughness-dominated regime, and the third is obtained during the transition between the previous two, as defined by a mixed-regime.

Although a large number of contributions have been made by analytical methods to the treatment of hydraulic fracture problems, there is still a large gap between the formulations developed to solve some particular hydraulic fracture problem and a realistic closed-form solution to deal with problems, where for example, multi-fractures are present in the rock. Therefore, it is reasonable to accept that more insight into the nature of the pore pressure

field in the vicinity of a hydraulic fracture can only be provided by the advance of numerical models.

Boone et al. (1991) have developed a poroelastic numerical model which provides a full coupling between rock deformation, fluid flow in the fracture and in the rock mass. Also, it includes a nonlinear, Dugdale-Barenblatt fracture model. In this work, the influence of poroelastic effects in the stress measurement have been investigated as well as the kinematics of fracture closure and reopening. They have noted that poroelastic mechanisms have caused a significant increase in the breakdown pressure for a borehole when compared to the value provided by the strength of materials approach, Equation (5.1). This effect has been attributed to higher rates of pressurization and to the diffusion of pore pressure from the borehole. The first is related to the rate dependent effect caused by the fluid's viscous flow resistance. The second is due to the fact that at loading rates which are fast relative to the diffusion of the pore pressure, the vertical stress varies from tension at the borehole wall to compression in a short distance away from it, decreasing the rate of fracture propagation.

A series of works developed by Papanastasiou (1997b), (1999a), (1999b) and (2000) have investigated the influence of plasticity in the opening and closure of a hydraulically driven fracture. A strongly coupled numerical simulator based on a finite element method to model the rock deformation and a finite difference scheme to solve the fluid flow in the hydraulic fracture has been used. The constitutive behaviour of the rock was represented by the well known Mohr-Coulomb surface and a cohesive crack model was employed as a propagation criterion. The effective fracture toughness has been obtained by the path independent J-integral. The major contributions provided are related to the mechanisms involved in the plastic yielding near the tip of a propagating fracture, and with the closure pattern of an elasto-plastic fracture. The analysis has shown that an increase by more than one order of magnitude in the rock effective fracture toughness is attributed to an effective shielding caused by the plastic yielding near the tip of a propagating fracture. This is influenced by the rock strength, elastic modulus, deviator of the in situ-stresses and pumping parameters. It has also been shown that a pressurized stationary elasto-plastic fracture closes uniformly with decreasing pressure, whereas the closure pattern of a propagated elastic fracture makes surface contact first at the tip and subsequently towards the wellbore.

5.2 Hydraulic fracture

5.2.1 Introduction

The use of hydraulic fracture to stimulate oil production in reservoirs is a very complex problem. The process starts with the injection of fluid into an existing pre-fractured sedimentary rock in order to open it in the first instance. At this stage, the pressure in the fracture is increased until it overcomes the minimum compressive stress acting in the formation. A further increase in pressure leads to the development of a tensile stress directly ahead of the crack tip, but at some offset from it, in a plane perpendicular to the direction of fracture propagation, strongly compression stresses still acts. This kind of stress condition causes the shearing of the rock mass, and consequently, leads to the development of a plastic zone. The representation of a hydraulic fracture growth in a plexiglas cube loaded biaxially in a triaxial press is shown in Figure 5.5.

The solution for the stress distribution around a circular hole in a homogeneous, isotropic, elastic material subject to a compression load proposed by Kirsch (1898) has been used by Hubbert and Willis (1957) to define a breakdown pressure, p_b, in hydraulic fracture applications. They stated that a fracture will initiate in a borehole wall if the minimum tangential stress and tensile strength of the material are lower than the fluid pressure acting in the hole. In vertical boreholes drilled from the surface, p_b is frequently obtained by the relation

$$p_b = 3\,\sigma_{h_{min}} - \sigma_{h_{max}} + \sigma_f - p_s \tag{5.1}$$

where, $\sigma_{h_{min}}$ and $\sigma_{h_{max}}$ are minimum and maximum horizontal compressive stresses, σ_f is the tensile strength of the material and p_s is the pore pressure. Also, it is assumed that fracture propagates in the direction of the minimum compressive stress, i.e, least resistance.

5.2.2 Hydraulic fracture analysis

Rocks and soils found in nature contain a large number of pre-existing fractures which are subject to the penetration of pressurized fluid. This effect is neglected by the classical approach described above and it is extremely important to the determination of a failure limit to the material, since it contributes to an increase in the stress intensity at the crack tip prior to fracturing. Therefore, it is reasonable to assume that the hydraulic fracture problem is more related to the definition of a critical condition for the growth

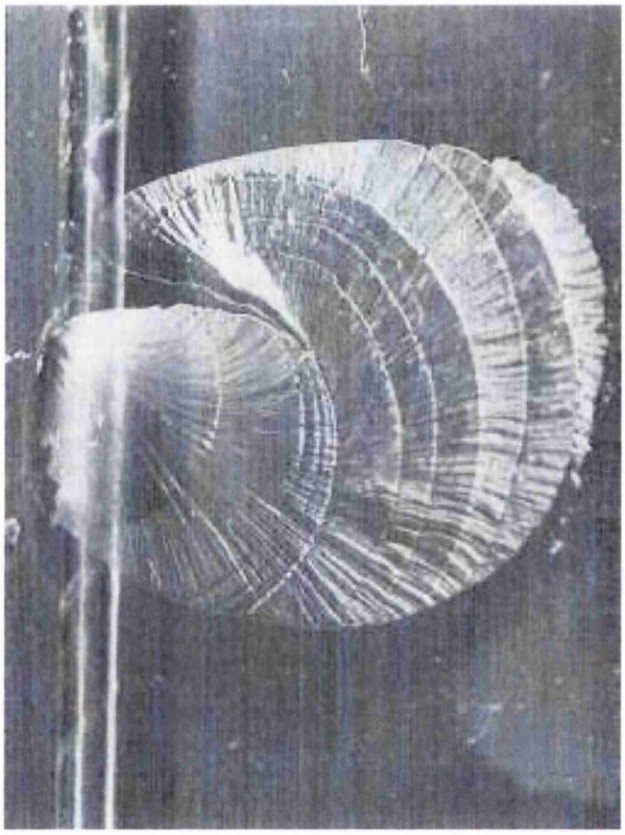

Figure 5.5: Hydraulic fracture growth in a biaxially loaded cube (Atkinson (1987)).

of existing fractures, rather than predicting crack initiation within idealized materials.

One analytical solution from extremes of very slow to very fast fracture propagation for the pore pressure fields has been derived from the well known potential theory and the work developed by Ruina (1978) respectively. The dimensions and boundary conditions employed in the solution of the pore pressure field can be seen in Figure 5.6 (a) and (b).

The potential theory assumes that the crack walls are permeable and steady state conditions have been reached. The solution for the pore pressure field is given by (Boone et al. (1991)):

$$p = \frac{F}{\pi}\,\varphi, \quad \varphi = \tan^{-1}\left\{\frac{2r^{1/2}}{r-1}\cos\left(\frac{\theta}{2}\right)\right\}, \quad 0 \le \varphi \le \pi, \tag{5.2}$$

where, F is the pressure applied at the crack face, r is the radial distance from the crack tip, normalized with respect to the crack length and θ is the

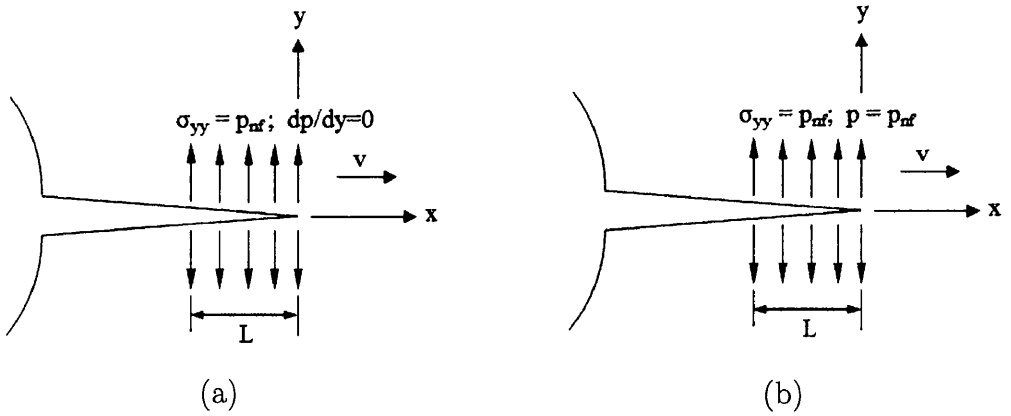

Figure 5.6: Boundary conditions applied to analytical solutions. (a) Ruina's model. (b) Classical potential flow theory.

angle measured with respect to the crack path. Under these conditions, the pore pressure field is positive everywhere.

On the other hand, the work developed by Ruina (1978) assumed that the crack faces are impermeable and the solution for the pore pressure field in the near tip region of a semi-infinite fracture moving at a constant rate is obtained as:

$$p = \frac{-K_Q}{\sqrt{2\pi r}} \left\{1 - e^{vr(1+\cos\theta)/(2c)}\right\} \cos\left(\frac{\theta}{2}\right), \tag{5.3}$$

where, K_Q is the apparent fracture toughness of the rock and v is the velocity of the fracture. The diffusivity coefficient c is a poroelastic constant and appears commonly in both analytical solution and numerical approximations and is expressed as:

$$c = \frac{2GB^2K(1-\nu)(1+\nu_u)^2}{9(\nu_u - \nu)(1-\nu_u)} \tag{5.4}$$

where, G is the shear modulus, ν is the drained Poisson's ratio, ν_u is the undrained Poisson's ratio, B is the Skempton pore pressure coefficient and K is the hydraulic conductivity.

From a computational point of view, the hydraulic fracture problem involves the coupling of five different fields as described below:

- *Structural* - is responsible for the displacements occurring in the rock and in the fracture. Together with the use of the well known kinematic and constitutive relations this phenomenon determines the deformations and stresses acting in the reservoir.

- *Seepage* - The fluid flow in porous rock is primarily responsible for changes occurring with pore pressure and saturation in the rock mass. These variables are crucial in the determination of the stress state in the rock mass. Consequently, seepage plays an important role in the determination of a failure limit.

- *Network flow* - the amount of fluid pumped into the fracture is a major factor responsible for its opening, closure or extension. The pressure in the fracture acts as a traction boundary condition affecting the deformations and stresses in the rock mass. Also, it affects the fluid flow in the rock mass.

- *Thermal* - the heat exchange between fluid injected, gases, oil and porous rock causes a variation in the material properties of the fluids and rock, such as mass density, viscosity, strength among others, influencing the overall analysis.

- *Mass transport* - non-natural fluids injected into fractures have present in their composition solid particles which are deposited along the crack walls to avoid closure. These creates a "*shield*" around the fracture reducing the flow into the rock mass and increasing the pressure in the fracture.

As a first approach, the analysis has been restricted to the coupling of structural, seepage and network flow fields, which will provide a good insight into the overall problem. The two remaining fields will be left for a future extension of the presented research.

5.3 Numerical results

Two numerical examples have been used to validate the numerical model proposed. First the numerical predictions are compared to experimental results in a small scale problem as published by van Dam et al. (1997). Secondly, comparison is made against a more realistic field scale problem as proposed by Papanastasiou (1999a).

In the following two examples poroelastic and poroelasto-plastic effects have been investigated.

5.3.1 Hydraulic fracture propagation in a small scale problem

The numerical results based on experiments published by van Dam et al. (1997) have been used to validate the numerical model. The experiment consists of cubic blocks 0.30 m in size which are loaded in a true triaxial machine to simulate in-situ stress states. After reaching the desired stress field (Table 5.3), a high pressure pump injects fluid to propagate the crack. Artificial rock samples made of cement, plaster and diatomite have been used. The fracturing fluid employed was silicon oil which behaves approximately as a Newtonian fluid.

The simulations presented here were carried out using a commercial Finite/Discrete Element code (Elfen (2005)) with custom routines that couple the rock deformation with fluid flow through both the rock and the fracture and the material properties (Table 5.1) correspond to a soft plaster. An axisymetric model was used and the boundary conditions adopted are shown in Figure 5.7. Due to symmetry, one half of the problem was modeled.

Four different cases have been considered: elastic, elastoplastic, poroelastic and poroelasto-plastic analysis. In the elastic and elastoplastic cases the vertical stress (σ_{yy}) and the width (e) profiles have been compared with the ones provided by van Dam et al. (1997). In the poroelatic and poroelastoplastic cases, different permeabilities for the rock were evaluated in order to assess the influence of the leak-off upon parameters such as length, aperture and vertical stress of the fracture. The permeability varies from 0 to 1000 miliDarcy (mD).

The mechanical behavior of the rock is described through the Mohr-Coulomb model which employs the well known Newton-Raphson method in the return mapping scheme. The cohesion coefficient (c), friction angle (ϕ) and dilation angle (ψ) are given as a function of the effective plastic strain (ε^{ps}), as shown in Table 5.2.

An interface law based on a cohesive-zone model has been used to describe the rupture process at the fracture tip. In this model, the softening curve is obtained through the energy release rate (G_f). Within this framework, the fracture is opened when the tensile strength (σ_f) and opening displacement (δ) reach a critical value.

Fluid has been injected into the fracture in the elastic and elasto-plastic cases in impermeable rocks for 101.1 and 107.1 seconds respectively. These were the times necessary for the fracture to propagate and the crack tip reaches a distance of 0.075 metres. The poroelastic and poroelasto-plastic analysis have been based on the same analysis time of the elastic and elastoplastic cases described above.

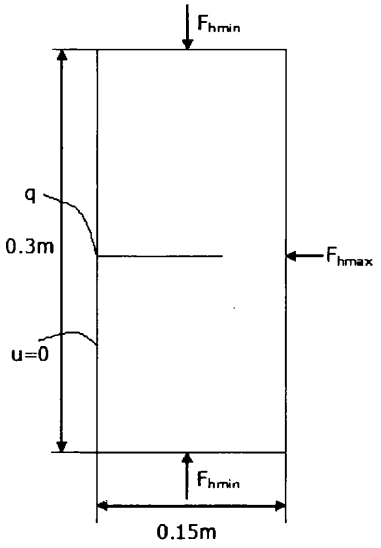

Figure 5.7: Schematic diagram

Input parameters	
Young's modulus	5.6 GPa
Poisson	0.2
Fluid mass density	1000 Kg/m^3
Solid mass density	2500 Kg/m^3
Fluid bulk modulus	2.0 GPa
Grain bulk modulus	3.11 GPa
Fluid viscosity	100 Pa.s
Tensile strength	1.0 MPa
Energy release rate	100.0 Pa.m
Porosity	0.2
Permeability	4.935e-14 m^2
Flow rate	2.5 cm^3/s
Initial aperture	62 μm

Table 5.1: Input parameters

ε^{ps}	c (Pa)	ϕ	ψ
0.0	2600	28°	28°
0.001	2.6	28°	14°
0.01	2.6	28°	0°

Table 5.2: Hardening properties.

Effective in situ stresses	Value (MPa)
Minimum horizontal	2.5
Maximum horizontal	4.0
Vertical	4.0

Table 5.3: In situ stresses.

Figures 5.8 and 5.9 show that the aperture profiles of the current model (σ_{yy}) agrees well with van Dam et al. (1997) for an elastic and elasto-plastic analysis respectively in an impermeable rock (k = 0 md). However, the vertical stresses exhibit some differences mainly close to the crack tip. These are a consequence of the model used by van Dam et al. (1997) which assumes the existence of a dry zone ahead of the crack tip obtained through a prescribed pressure equal to zero at this point. This approach is responsible for the development of a higher vertical stress gradient in this zone when compared to the current model as can be seen in Figures 5.10 and 5.11.

The aperture in the elasto-plastic case in an impermeable rock is larger than in the elastic case due to the development of inelastic deformations. Consequently, it requires a higher pressure for the propagation of the fracture. These plastic deformations are responsible for the softening of the material which affects the size of the aperture and in situ stresses. The vertical stresses in the elasto-plastic case are higher near the fracture tip and lower close to the crack mouth when compared to the elastic case. This can be seen in

the vertical stress profile, where an increase in σ_{yy} is experienced near the fracture tip in the elasto-plastic analysis and a lower value is found in the crack mouth.

Figures 5.8 and 5.10 show the aperture and vertical stress profiles in the poroelastic analysis for rocks with different permeabilities. It can be seen that in rocks with higher permeabilities, the length and width of the fracture reduces as expected, as a consequence of an increase in the leak-off from the fracture to the porous rock. Also, vertical stresses in highly permeable rocks exhibit a more linear distribution along the fracture with high net pressures located at the wellbore. As a consequence, net pressures need to be higher to propagate fracture in rocks with higher permeabilities, as noticed previously by Boone et al. (1991).

In contrast with the geometry presented by the poroelastic case, the apertures in the poroelasto-plastic case have shown a different behaviour. The length reached by the crack tip of rocks with higher permeabilities are shorter than the previous one, but the apertures have increased, as shown in Figure 5.9. In highly permeable rocks the diffusion of the fluid into the rock is higher, consequently, it affects the effective stresses in far field regions causing a more widespread development of the inelastic deformations. The σ_{yy} in rocks with high permeabilities is more likely to present a steep gradient near the crack tip and a more uniform distribution near the wellbore region, as can be seen in Figure 5.11.

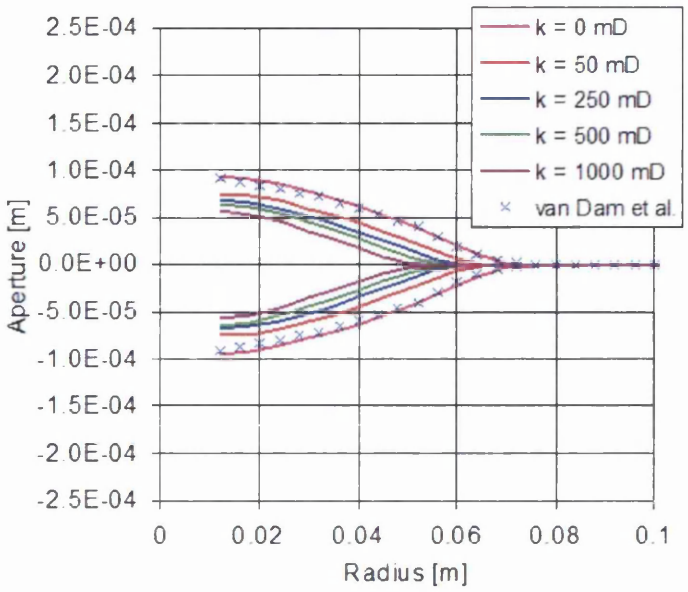

Figure 5.8: Influence of the leak-off in the size of the fracture in a poroelastic medium.

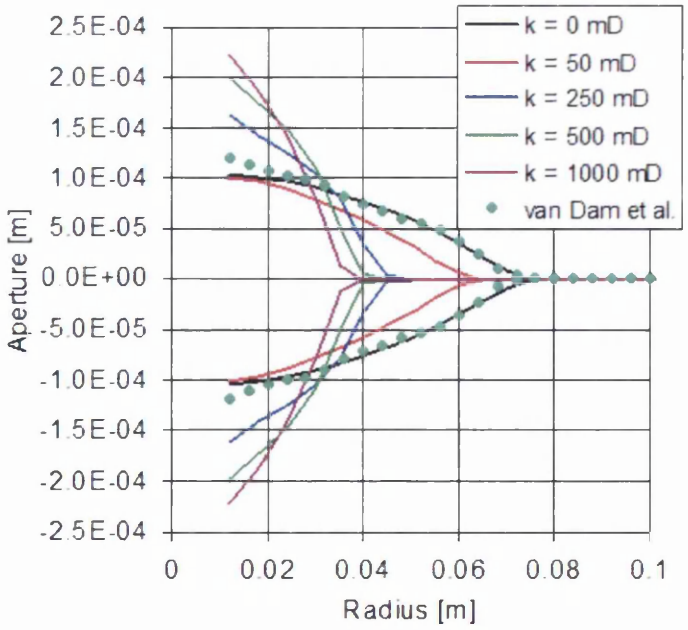

Figure 5.9: Influence of the leak-off in the size of the fracture in a poroelasto-plastic medium.

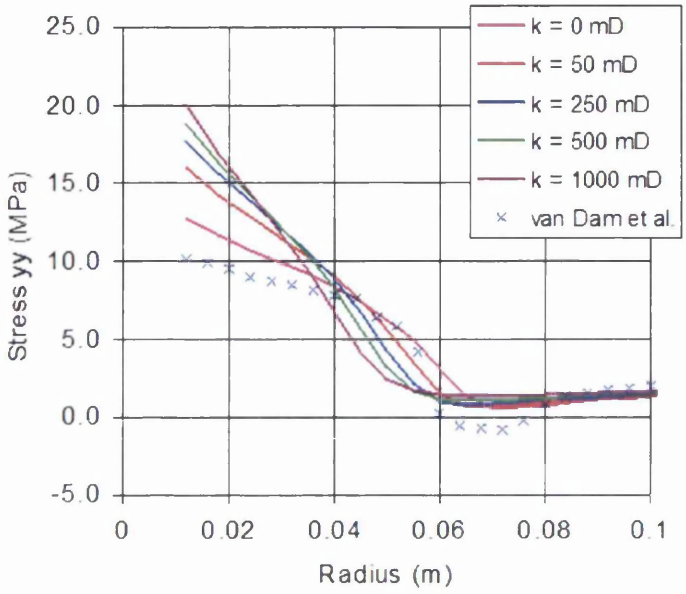

Figure 5.10: Influence of the leak-off in the vertical stresses in the plane of the fracture in a poroelastic medium.

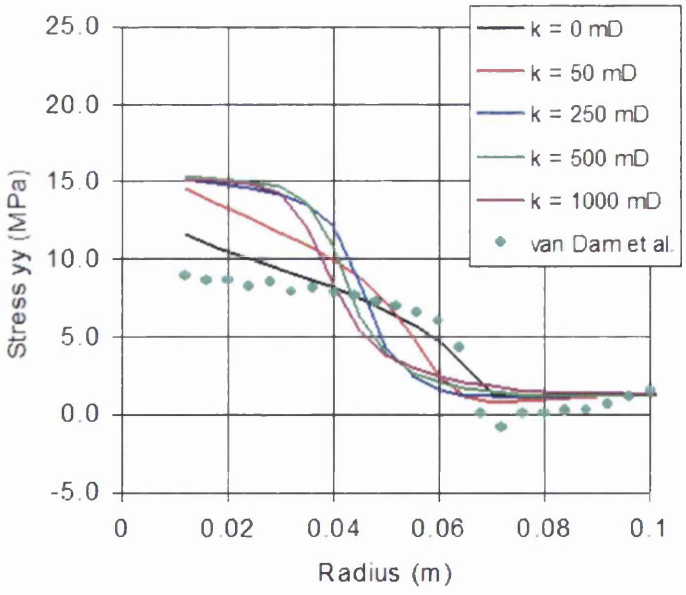

Figure 5.11: Influence of the leak-off in the vertical stresses in the plane of the fracture in a poroelasto-plastic medium.

5.3.2 Hydraulic fracture propagation in a field scale problem

The following example has been taken from Papanastasiou (1999b), and used as a reference to validate and calibrate the proposed numerical model for further 2D and 3D analysis which will take into account leak-off effects.

The problem consists of a vertical hydraulic fracture which propagates horizontally in a deep rock formation where the maximum in situ stress acts in the vertical direction. The hydraulic fracture zone is located at 1500 metres deep in a poorly consolidated sandstone. Some of the parameters, such as in situ stresses, Young's Modulus, Poisson ratio, tensile strength, fluid viscosity and flow rate, were taken from real field data extracted from specialized coring, logging and stress measurements, while, others have been "best estimated" (Tables 5.4 and 5.6). The hardening curve adopted is shown in Table 5.5 and is calibrated in a way such that the rock is initially elastic but very close to a yielding state.

Firstly, a 2D plane strain analysis in an impermeable elastic and elasto-plastic rock is carried out. Then, an extra degree of complexity is added through the inclusion of poroelastic and poroelasto-plastic effects. Finally, a full 3D model is verified against results obtained in the 2D plane strain analysis. In order to obtain a similar geometry to that provided by the 2D plane strain model, the thickness value adopted in the 3D case is 1 metre.

The constitutive behaviour of the rock is modeled by the well known pressure-sensitive Mohr-Coulomb surface. A cohesive crack zone model based on the energy release which takes into account the softening behaviour of rocks is employed as a propagation criterion.

The analysis consists of pumping fluid into the fracture until the crack tip reaches a distance of 8 metres. Then, an aperture profile is obtained and compared against the results published by Papanastasiou (1999b). Once, the model is calibrated, the influence of leak-off effects are investigated. Other important aspects verified are the pore pressure distribution and the development of the effective plastic strain, since, these are expected to strongly influence the fluid pressures.

The analysis time for the crack tip to reach the 8 metres distance required in the elastic and elasto-plastic analysis was 37.8 seconds and 49.5 seconds respectively. The permeability of the rock formation in the poroelastic analysis has been considered to be 50 miliDarcy (mD) and analysis time was 45 s. In the poroelasto-plastic case, two different permeabilities (50 mD and 200 mD) have been considered with analysis time of 61.9 seconds and 118 seconds respectively. The initial pore pressure was assumed to be equal to 2 MPa in both cases.

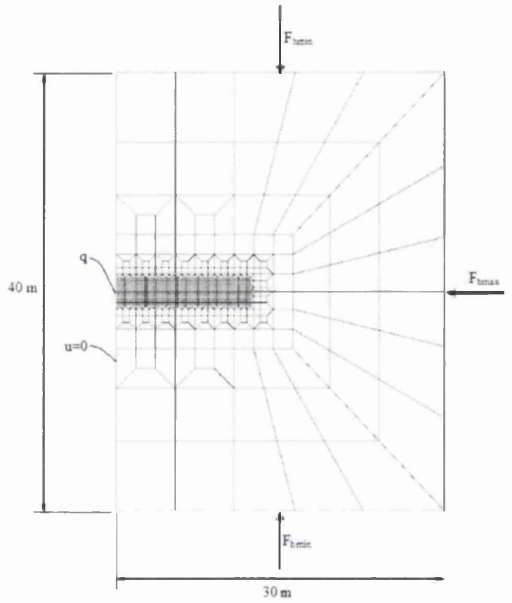

Figure 5.12: Schematic diagram

Input parameters	
Young's modulus	16.2 GPa
Poisson	0.3
Fluid mass density	1000 Kg/m^3
Solid mass density	2500 Kg/m^3
Fluid bulk modulus	2.0 GPa
Grain bulk modulus	31.1 GPa
Fluid viscosity	0.1 Pa.s
Tensile strength	0.5 MPa
Energy release rate	112 Pa.m
Porosity	0.2
Permeability	4.935e-14 m^2
Flow rate	0.0005 m^3/s
Initial aperture	62 μm

Table 5.4: Input parameters

ε^{ps}	c (Pa)	ϕ	ψ
0.0	2000000	28°	28°
0.0012	2000	28°	14°
0.001	200	28°	0°

Table 5.5: Hardening properties.

Effective in situ stresses	Value (MPa)
Minimum horizontal	3.7
Maximum horizontal	9.0
Vertical	14.0

Table 5.6: In situ stresses.

A good agreement between the aperture in an elastic impermeable rock and the results presented by Papanastasiou (1999c) has been obtained, as shown in Figure 5.13. Also, in the poroelastic case the aperture has been shown to be slightly smaller near the wellbore and about the same size near the crack tip. These are attributed to a higher leak-off in the region near the wellbore which causes an increase in the stiffness of the rock as a consequence of the higher pore pressures located in that zone.

In the elasto-plastic case of an impermeable rock the aperture has been shown to be smaller than those produced by Papanastasiou (1999c), mainly near to the wellbore region as shown in Figure 5.14. This is attributed to the initial conditions applied by the reference, in which an analytical solution proposed by Desroches et al. (1994) was employed to set initial values of aperture and pressure for an initial fracture length. In a previous work Papanastasiou (1997a) has shown that in his proposed numerical model "*the initial fracture length had an effect on the fracture profiles in the initial fracture length interval, but, the fracture profiles were correctly calculated in the regions where the fractures were propagated*". Even though the present

work has tried the same approach for the initial fracture length, no significant differences have been observed against the parameters used by the present analysis. Another possible reason is the choice of hardening properties, since in Papanastasiou (1997b) the linear hardening plasticity modulus has been derived from the loading and unloading Young's modulus.

In a poroelasto-plastic analysis, Figure 5.14, the apertures have shown two distinctive behaviours. For $k = 50$ mD, the aperture was smaller than that obtained for $k = 0$ mD near the wellbore and slightly wider near the crack tip. However, for $k = 200$ mD, the aperture was shown to be wider throughout the entirely fracture length.

The explanation arises from the fact that near the wellbore the increase in the effective plastic strains generated by the increase of the effective normal stresses and consequently reduction of the yield stresses are not sufficient to overcome the extra stiffness induced by the increase of pore pressure in the rock with $k = 50$ mD. On the other hand, in the rock with $k = 200$ mD, the pore pressure effects are not predominant compared to the inelastic deformations, causing an increase in the width of the fracture.

Near the crack tip, the formation of a fluid lag region is noticed in permeable rocks as shown in Figures 5.22 and 5.23, but not in the impermeable case, Figure 5.21. These are responsible for a higher pressure gradient in that region, mainly for the rock with $k = 200$ mD. Consequently, higher fluid pressure is required in order to open the fracture, leading to a higher shearing of the rock. This causes the permeable rocks to present a wider opening in that zone.

Figures 5.15, 5.16 and 5.17 show the development of the effective plastic strains. For $k = 0$ mD, the effective plastic strains are mostly generated by the shear stresses in the rock near the crack tip region, as a result of the characteristic loading developed by the pressurized fluid in the fracture as explained previously. In the permeable cases, as the material model has been calibrated so as to be very close to a yielding state, as soon as the fluid starts to leak-off from the fracture to the rock, a yielding state is achieved as a result of the increase of the effective normal stress. This is responsible for the development of the effective plastic strain in almost the full extension of the fracture. However, at the crack tip, where shear loads are also present, the rock with $k = 50$ mD seems to be less affected by the shearing of the rock when compared to the rock with $k = 200$ mD.

Finally, in Figure 5.24 the fluid pressure distributions along the fracture are presented. As can be seen, the poroelasto-plastic rocks have exhibited higher fluid pressures when compared to the others cases, showing that not only plasticity plays an important role, but also that leak-off effects cannot be neglected.

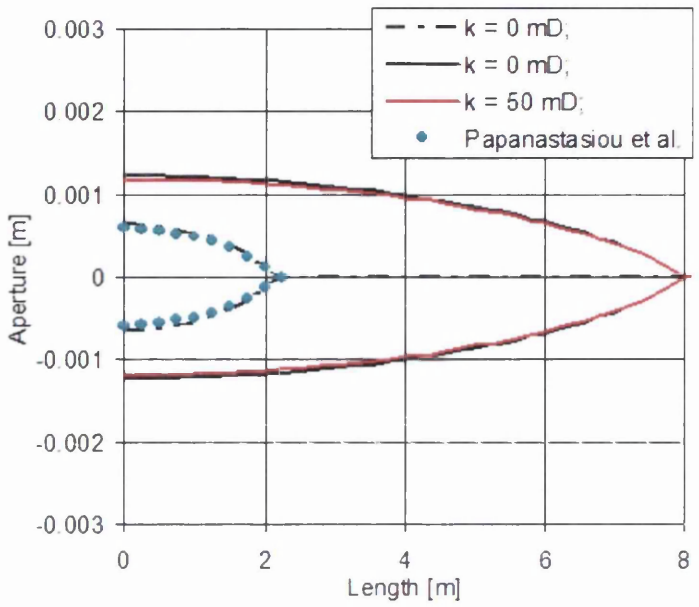

Figure 5.13: Influence of the leak-off in the width of the fracture in a poroelastic medium.

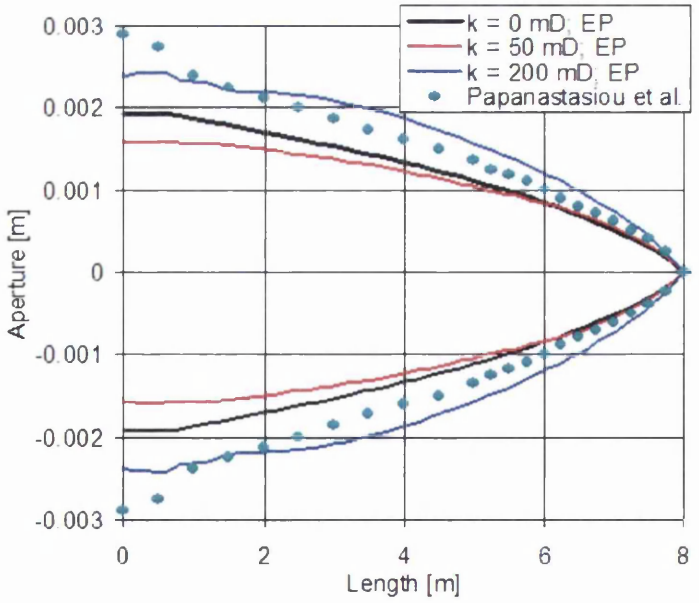

Figure 5.14: Influence of the leak-off in the width of the fracture in a poroelasto-plastic medium.

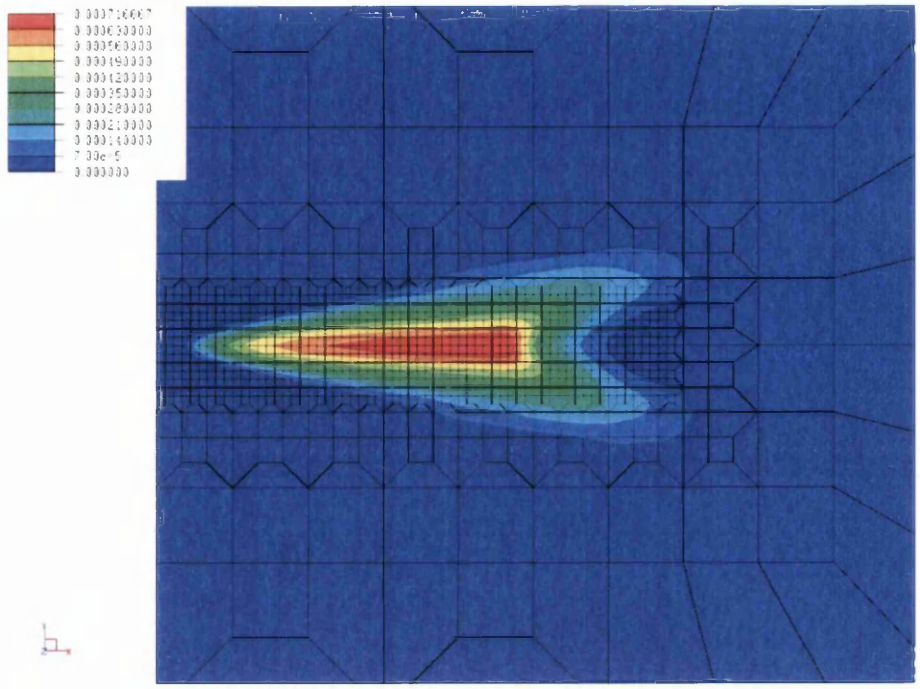

Figure 5.15: Effective plastic strains in an impermeable rock ($k = 0$ mD).

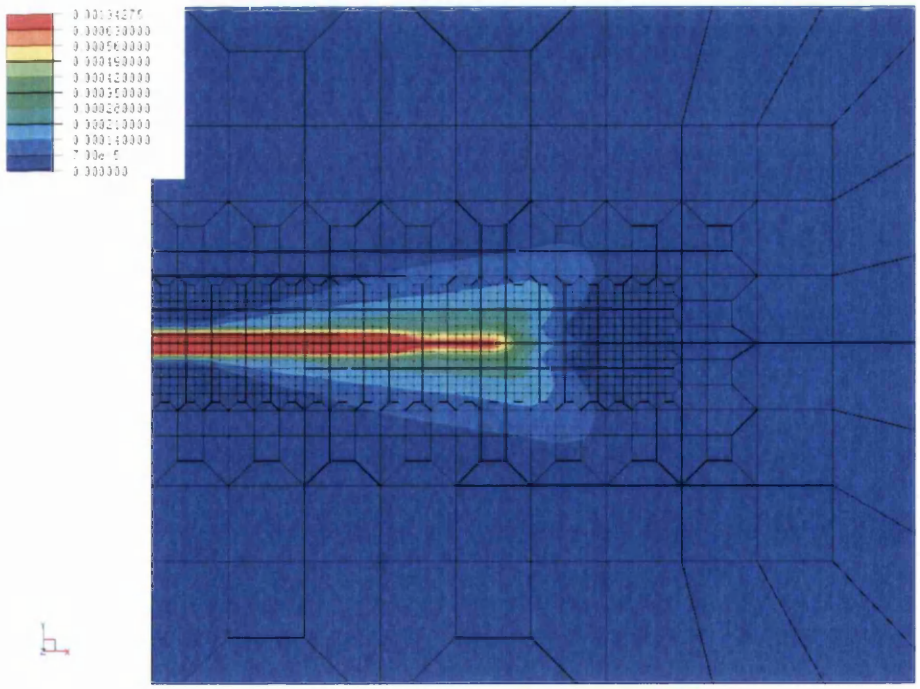

Figure 5.16: Effective plastic strains in a permeable rock ($k = 50$ mD).

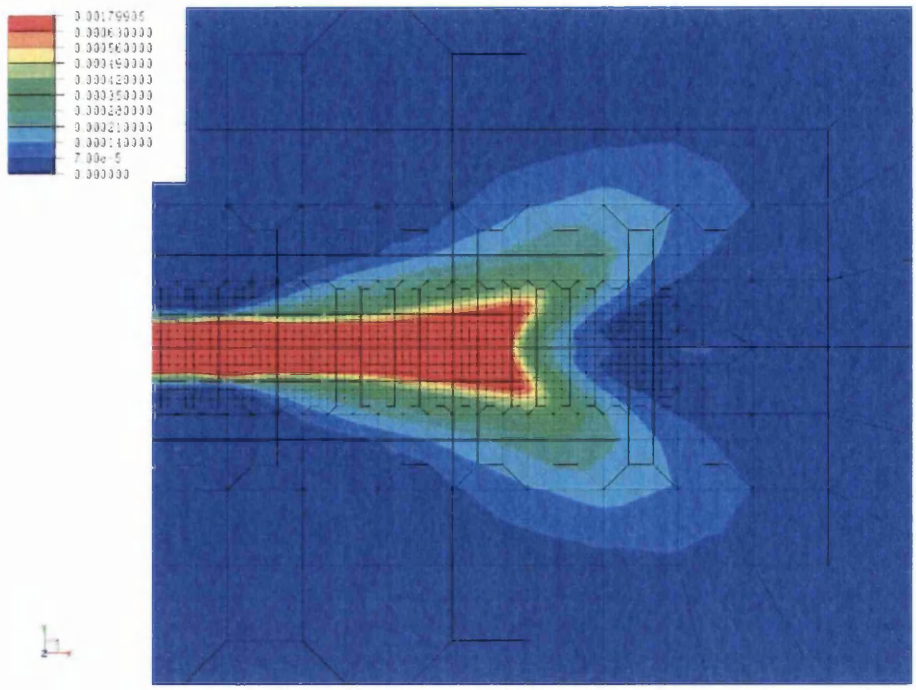

Figure 5.17: Effective plastic strains in a permeable rock ($k = 200$ mD).

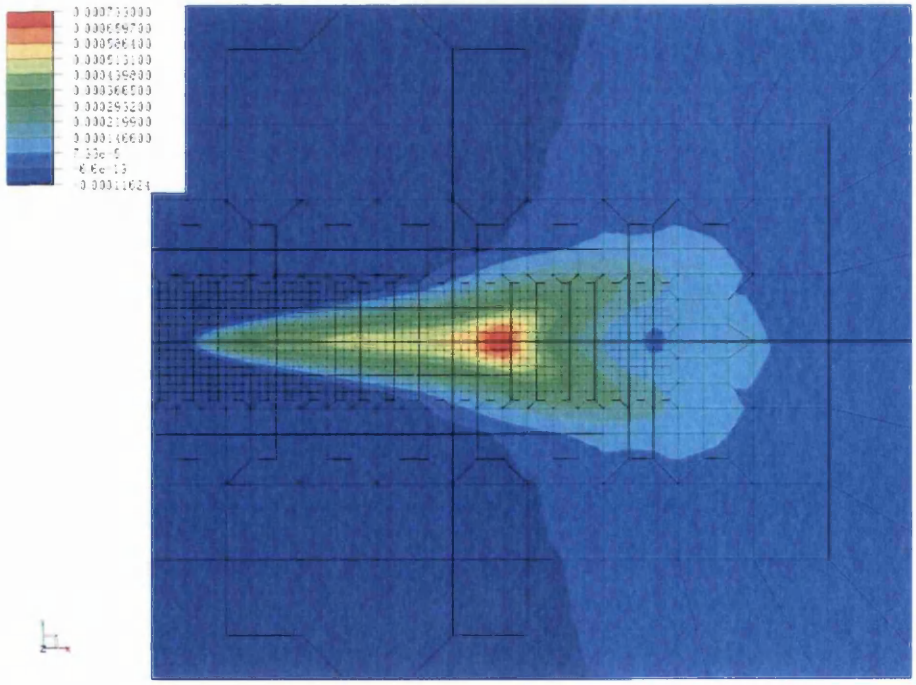

Figure 5.18: Volumetric strains in an impermeable rock ($k = 0$ mD).

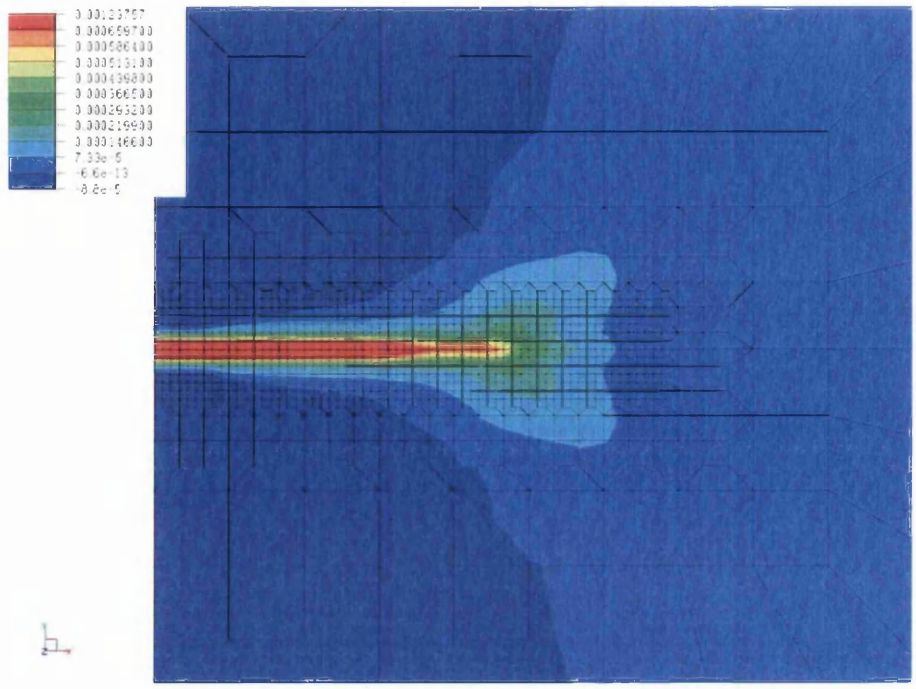

Figure 5.19: Volumetric strains in a permeable rock ($k = 50$ mD).

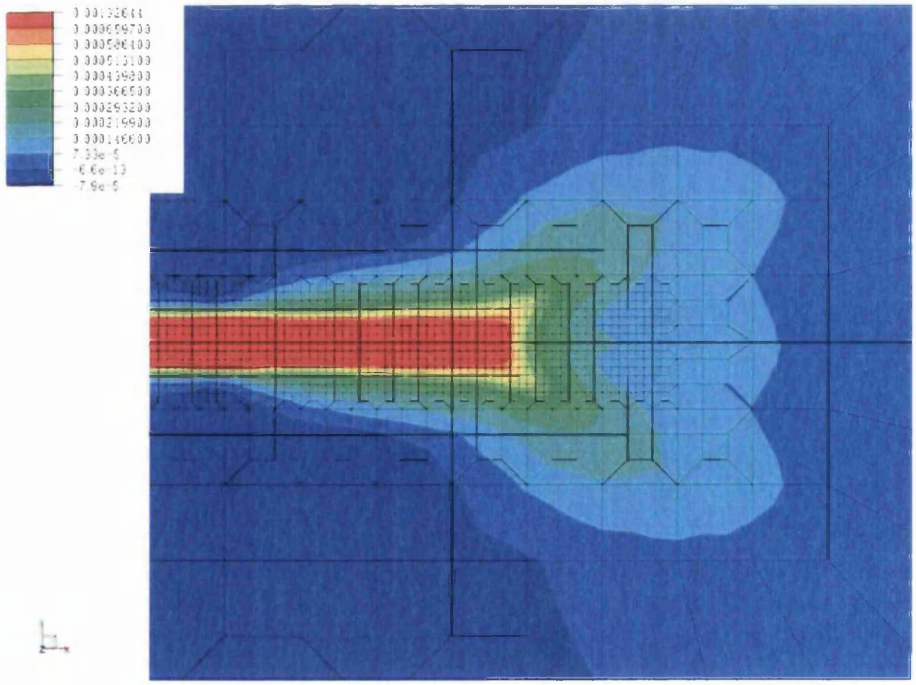

Figure 5.20: Volumetric strains in a permeable rock ($k = 200$ mD).

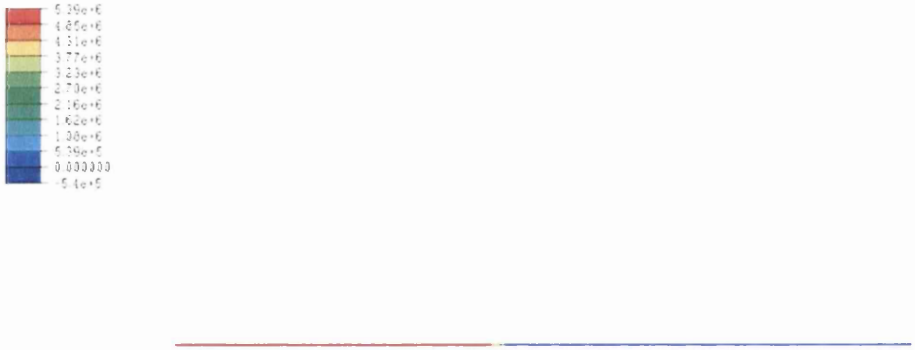

Figure 5.21: Fluid pressures in an impermeable rock ($k = 0$ mD).

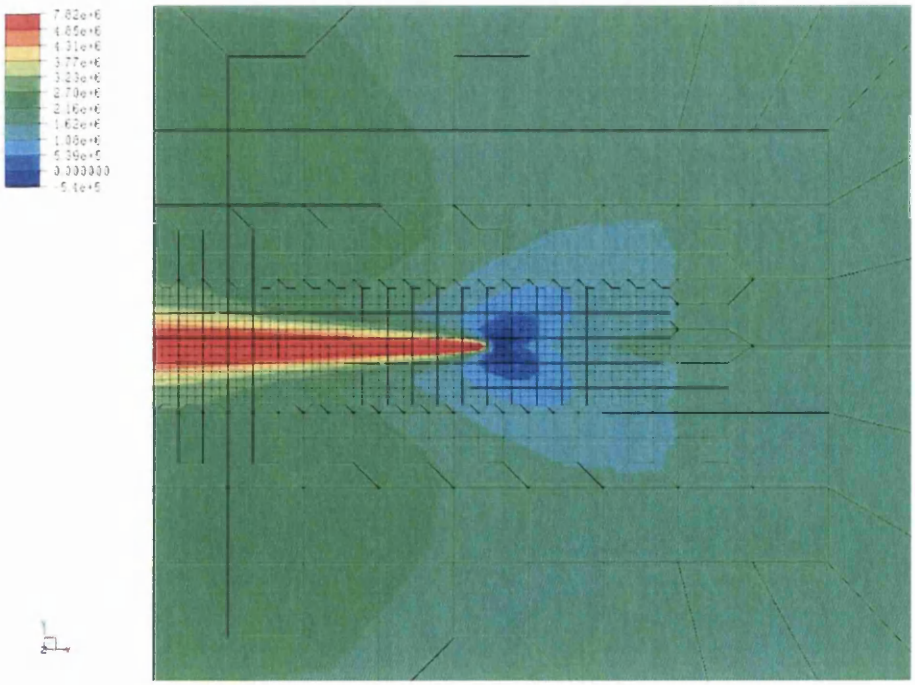

Figure 5.22: Pore pressures in a permeable rock ($k = 50$ mD).

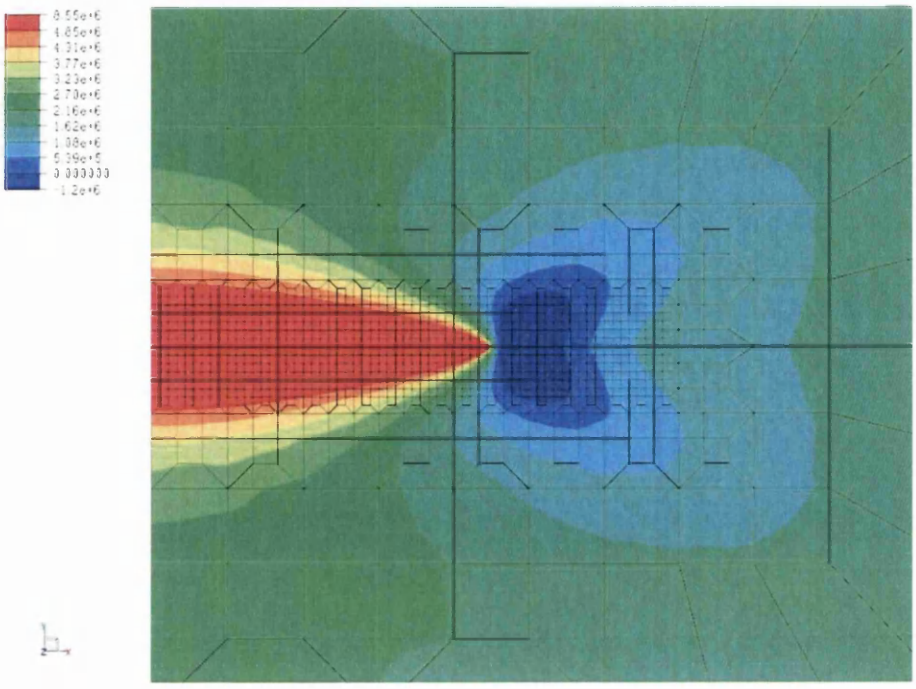

Figure 5.23: Pore pressures in a permeable rock ($k = 200$ mD).

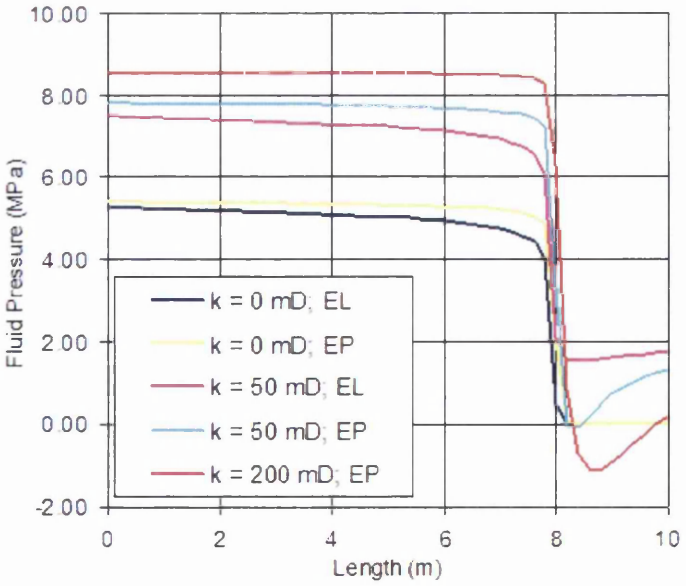

Figure 5.24: Fluid pressures along the fracture (2D case).

Figures 5.25 and 5.26 show a comparison between the aperture profiles obtained through 2-D and 3-D analysis in impermeable and permeable rocks. The results show very small differences which are associated with the corner contact in discrete elements. It seems that the tensile strength in the 3-D case has been slightly reduced in comparison with the 2-D case, causing a further increase in the length of the fracture.

The fluid pressures in the fracture are represented in Figure 5.27 for an impermeable rock and in Figure 5.28 for the permeable case ($k = 50$ mD). They show a good agreement with the ones presented by the 2D analysis.

Finally, the fluid pressure distributions along the fracture has been compared against the 2-D case. As expected, the fluid pressure for the 3-D analysis has shown to be slightly lower than the 2-D case, as a consequence of the reduction in tensile strength caused by the corner contact in discrete elements.

The results obtained have shown a good agreement with the ones presented by Papanastasiou (1999c), proving the robustness of the numerical procedure adopted.

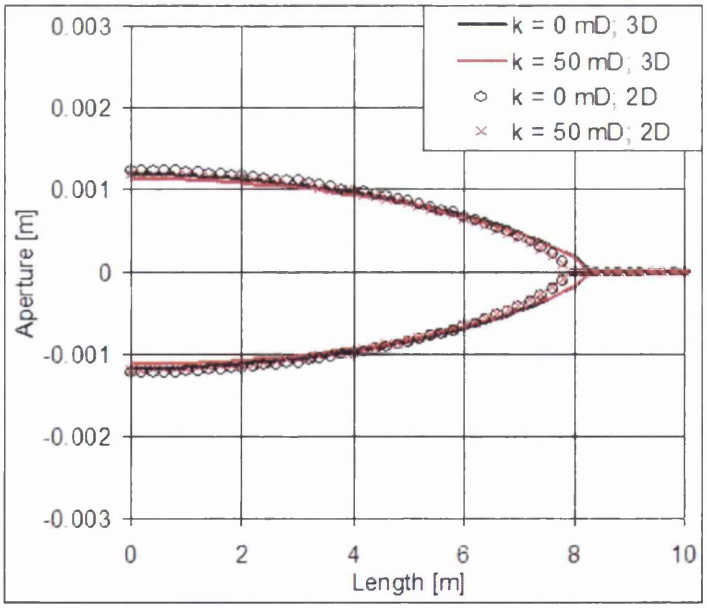

Figure 5.25: 2D versus 3D aperture profiles in impermeable and permeable elastic rocks.

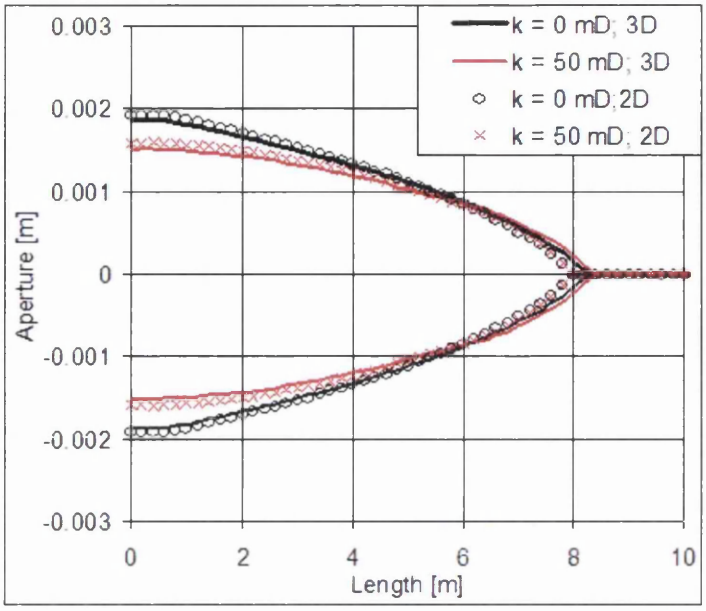

Figure 5.26: 2D versus 3D aperture profiles in impermeable and permeable elasto-plastic rocks.

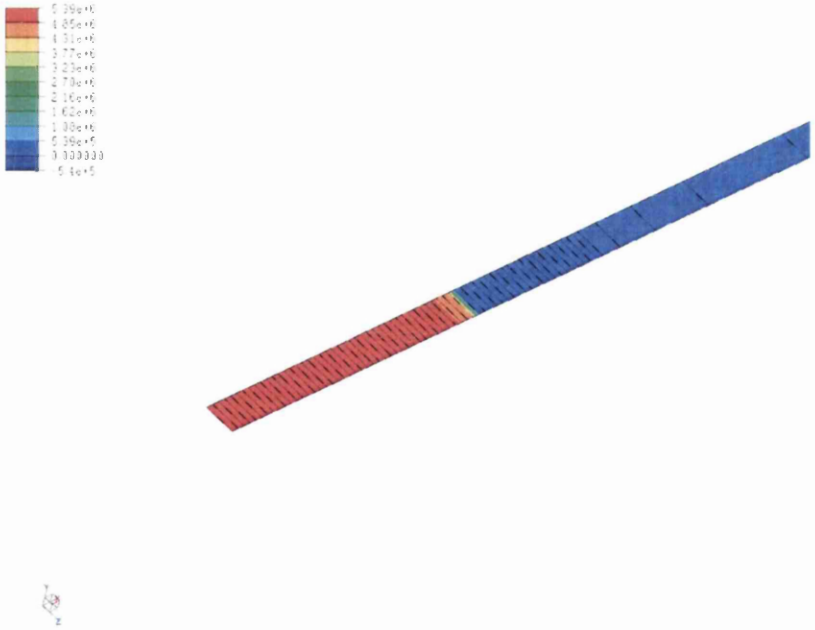

Figure 5.27: Fluid pressures in an impermeable rock ($k = 0$ mD).

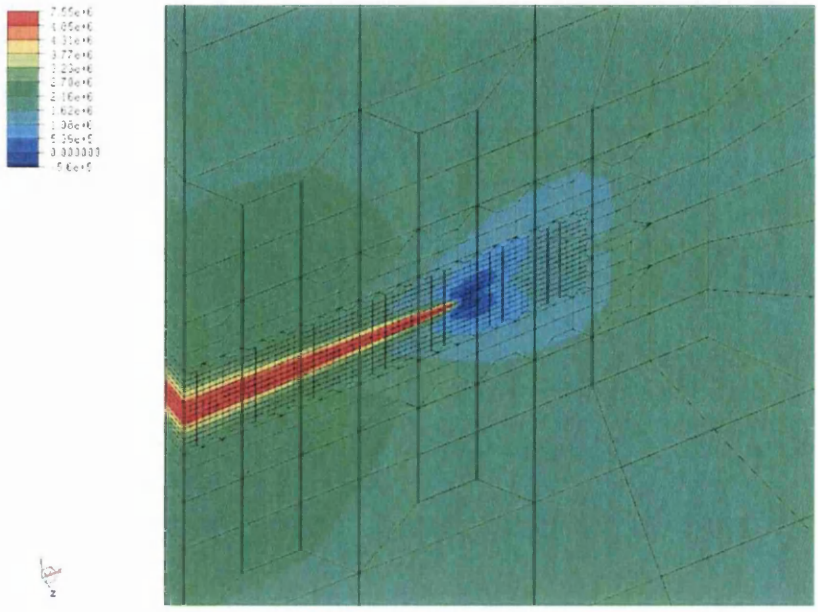

Figure 5.28: Pore pressures in a permeable rock ($k = 50$ mD).

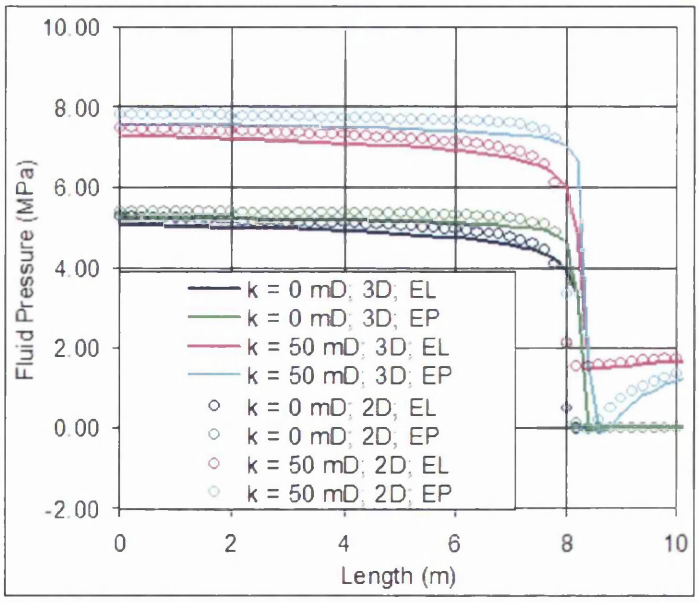

Figure 5.29: Fluid pressures along the fracture (3D case).

In summary, the proposed computational tool has been shown to be a powerful tool in the analysis of hydraulic fracture problems in oil production, providing a detailed knowledge of crucial variables involved in the process, such as: fluid pressure, apertures, pore pressures and in situ stresses, among others.

In the following chapter, another application where the proposed numerical procedure has proved to be particularly useful is investigated.

Chapter 6

Slope stability

The study of previous works related with rock mass stability has stimulated the present author to verify the influence of water pressure in slope stability problems. The focus has been directed at plane slope failures, due to the simplicity of obtaining a solution through a limit equilibrium method. The analytical results will be compared against numerical examples, in order, to validate the proposed model, as well as, to indicate some of the limitations of the analytical approach.

6.1 Background

Stability of slopes has been extensively studied over recent decades. Some of the first studies developed by authors such as Blake (1967), Yu et al. (1968), Blake (1969), Wang and Sun (1970), Stacey (1971), have assumed that the rock mass behaves as an elastic continuum. This has stimulated the use of numerical tools, such as the finite element method, and photoelastic stress analysis. The results obtained have shown to be very interesting and assisted analysts in understanding some of the mechanisms involved in slope failure.

Recently, more complex studies incorporating elasto-plastic continuum analysis with solid-fluid interaction have been carried out by a number of researchers. Griffiths and Lane (1999) have compared a series of slope stability results obtained by the FE methods against values predicted by equilibrium methods. A wide range of numerical examples involving no pore pressures, undrained clays slopes, and submerged and partially submerged approaches has been evaluated. The results have shown to be in good agreement with theory.

Ng and Shi (1998) and Cho and Lee (2001) have investigated the stability of an unsaturated slope due to intensive rainfall and its effect on soil slope

behavior using a FE flow-deformation coupled analysis. They have observed that the stress field is modified by water pressure distribution controlled by the spatial variation of hydraulic conductivity during rainfall infiltration, which affects the shear strength on the potential failure surface.

Ehlers et al. (2004) has used FE procedures with a space-adaptive method and a triphasic formulation, which couples the solid deformation with the water and gas flow, to investigate the deformation and localization behavior of unsaturated soil. The results have shown a significant influence of the fluid saturation on the solid deformation up to the onset and the development of localization phenomena prior to a possible failure of embankments and slopes.

Although, a good insight has been brought by previous studies based on continuum approaches, a comparison against practical rock slope behavior is still limited, since in most practical slope problems, it is possible to verify that the rock mass is not a continuum and its behavior is dominated by discontinuities such as bedding planes, faults and joints, as described by Muller (1959) and others.

The use of realistic numerical methods in modelling practical rock slope behaviour are in constant development, since, this type of problem involves a series of non-linearities imposed by contact, friction, development and propagation of fracture, network and seepage flow, large rotation and translation, data acquisition, among others. These difficulties make the role of analysts more crucial in the verification of the results and in the knowledge of the assumptions involved. However, the use of equilibrium methods, depending on the complexity of the problem investigated, can be considered almost unfeasible. Some of the studies developed using the discontinuum approach have been based on numerical methods such as the finite element method (FEM), discrete element method (DEM) and discontinuous deformation analysis (DDA).

In the work developed by Kim et al. (1999), one of the tasks has been to incorporate in the DDA method, the hydro-mechanical coupling between rock blocks and steady water flow in fractures. The aim is to evaluate the influence of fracture flow on the stability. In the evaluation of a tunnel example, it has been observed that water pressure caused by gravitational forces are essential factors to be taken into account in the tunnel stability analysis.

Eberhardt et al. (2004) has used a Finite/Discrete Element method which combines continuum and discontinuum methodologies, to understand the progressive failure in massive natural rock slopes as a function of slide plane surface and internal strength degradation. The failure process is triggered by the initial formation of brittle tensile fractures, which leads to the development of shear degradation and mobilization.

In a more recent work, Zhao et al. (2007) have simulated the spontaneous crack generation in brittle crustal rocks using particle simulation method. The deformation pattern in a basement controlled reverse faulting, resulting in crustal fault propagation folding above rigid basement blocks have shown to be very similar with field observations, demonstrating that their newly-proposed discontinuous type of loading does not exaggerate the ductile behavior of brittle rocks, being more suitable for dealing with this kind of problem, in comparison with the conventional continuous type of loading procedure.

From the wide variety of problems involving rock mass stability, the present work will focus on problems involving plane slope failures with water pressure effects. A comparison of the results against limiting equilibrium methods can be used to validate the numerical model. A description of the assumptions and limitations of the limit equilibrium method and the computational tool developed will follow.

6.2 Plane failure

6.2.1 Introduction

Slope failure processes can be classified as plane, wedge, circular, toppling and ravelling. The first three slope failures allow the use of limit equilibrium methods to calculate a factor of safety (*FOS*), since failure is related to simple sliding. Among them, plane failure is the simplest one and rarely can be found in practical rock slopes because of the difficulties in satisfying all the geometrical conditions required for such a failure to occur, (Figure 6.1). On the other hand, from the computational point of view it is particularly interesting, since in some cases a simple 2-D plane strain analysis can be used to address the problem.

According to Hoek and Bray (1977), the conditions necessary for sliding to occur on a single plane are:

(a) The slope face should be parallel or nearly parallel (within approximately $\pm$ 20°) to the failure plane on which sliding takes place.

(b) The dip of the failure plane must be smaller than the dip of the slope face, i.e. $\psi_f > \psi_p$.

(c) The angle of friction of a failure plane must be smaller than the dip of this plane, i.e. $\phi < \psi_p$.

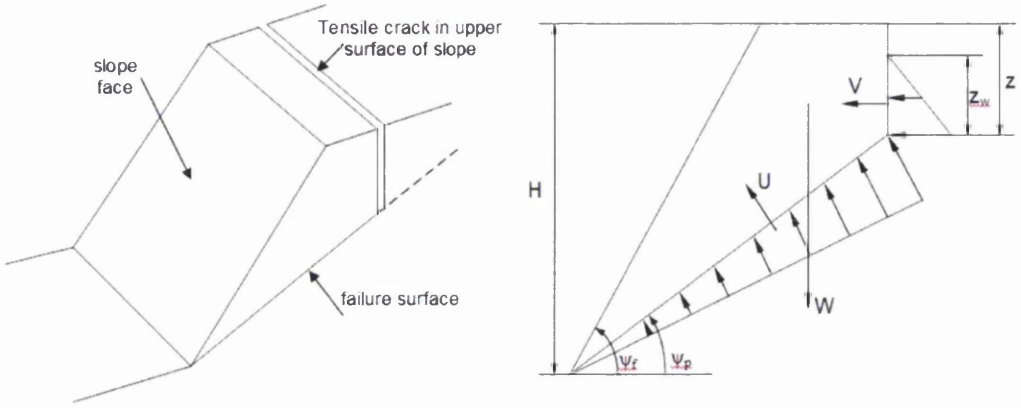

Figure 6.1: Geometry of a plane slope failure with fissure filled with water.

(d) The resistance force provided by release surfaces must be negligible. Also, the rock mass must contain the release surfaces in order to define lateral boundaries of the slide. Alternatively, a failure plane passing through the convex "nose" of a slope is enough for failure to occur.

6.2.2 Plane failure analysis

The stability of slopes with geological discontinuities are significantly affected by the orientation and inclination of these imperfections. Depending on a combination of these parameters a simple sliding of blocks, wedges or slabs can be avoided. Failure mechanisms in these slope are related to the coalescence and growth of the voids of the intact rock material and shear strength failure. In cases where angles between failure surfaces and slope face are around 30° to 70°, pure shear strength failure can occur. Also, slopes with this type of discontinuity surfaces present a more unstable condition than the ones with vertical and horizontal discontinuity surfaces.

In the analysis of simple sliding occurring in a plane failure where the crack is filled with water, several assumptions are made as described below:

(a) Water enters through the tensile crack in the upper surface of the slope and seeps along the fissure until the sliding surface strikes the slope face where it escapes at atmospheric pressure. The water pressure gradient in the tension crack has been assumed to increase linearly from the upper surface of the slope until it strikes the sliding surface. Then, along the sliding surface a linear decrease is assumed until the failure surface daylights the slope face, as shown in Figure 6.1. For general slope designs, this pressure distribution is reasonable. Although, a more conservative

assumption could be made assuming that the escape of the water is blocked, instead of the zero pressure condition.

(b) All the forces involved during the sliding process, such as the weight of the sliding block (W), the uplift force generated by the water pressure in the sliding surface (U) and the force caused by the water pressure in the tension crack (V), are considered to act at the centroid of the rockfall. This implies that no moments that could cause rotation and lead to failure are being taking into account. Although in actual slopes this assumption is not particularly true, the errors introduced are sufficiently small to allow us to neglect them.

(c) Coulomb's friction law is responsible for the shear strength of the sliding surface. It is important to notice that the effective normal stress (σ'_n) is increased by the water pressure, leading to a decrease in the effective shear stress (τ'). The cohesion (c), normal stress (σ_n), friction angle (ϕ) and water pressure (p) are related by the equation given below:

$$\tau' = c + (\sigma_n + p)\, tan\phi \tag{6.1}$$

(d) The slope is considered to have a unit thickness.

The cohesive and frictional properties of materials, such as many gravels and sandy soils and most hard rocks, are not significantly affected by the presence of water, i.e., they are considered to be constants even when changes in moisture content of the soils occurs. Therefore, modifications in the effective normal stress along the failure surfaces are entirely related to the changes in the water pressure distribution. On the other hand, in the case of clays and soft rocks changes in moisture content must be take into account as cohesion and friction angle are significantly affected.

6.2.3 Factor of safety in a slope

An interesting approach to verify the stability of the block is the use of a polygon of forces, as shown in Figure 6.2. It becomes clear that in the block a resisting force (R), which is composed of friction force (f) and cohesion force (cl), acts against the forces tending to induce the sliding of the block (S), which is formed by the weight of the block (W), the uplift force (U) and lateral force (V) due to water pressure. The sliding process in a slope is initiated when R is insufficient to support S, i.e., the balance of forces acting in the block, which is known as a limit equilibrium condition, is exceeded by S. Therefore, it is reasonable to define a parameter which quantifies the ratio

between the forces resisting/inducing sliding in a slope. This parameter is known as the factor of safety and for the problem presented in Figure 6.1 can be derived as:

$$FOS = \frac{cA + (W cos(\psi_p) - U - V sin(\psi_p)) \, tan(\phi)}{W sin(\psi_p) + V cos(\psi_p)} \tag{6.2}$$

There are three different situations regarding the magnitude of the FOS. For $FOS < 1$, sliding of the block is expected, since $S > R$. On the other hand, for $FOS > 1$, the block should remain static, since $R > S$. The critical situation is the case for $FOS = 1$, because the block is in an imminent stable condition, and any disturbance could initiate the process of sliding of the slope.

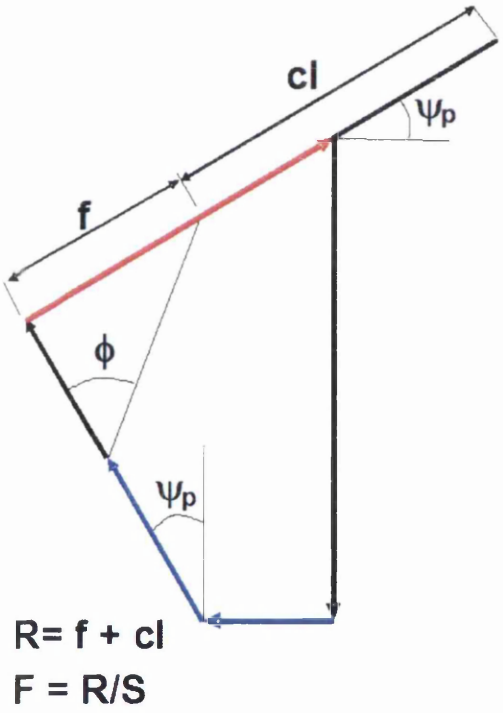

- Weight of the block (W).
- Uplift force of the water (U).
- Lateral force of the water (V).
- Effective normal force (N').
- Friction angle (ϕ).
- Dip of failure plane angle (ψ_p).
- Friction force (f).
- Cohesion force (cl).

Figure 6.2: Polygon of forces acting on a slope.

In practical slope design problems, a conservative increase in the FOS is commonly applied. For example, in mine slopes values for the factor of safety are around 1.3 since they are not required to remain stable for long period of time. For critical slopes such as haul roads and important installations, a factor of safety of 1.5 is necessary.

6.3 Numerical results

Three numerical examples will be used to validate and demonstrate the accuracy and capabilities of the numerical model proposed. The degree of complexity of the examples will be increased as confidence is gained. Firstly, a shear box test will be used to check the accuracy and reliability, since its analytical solution is simple to be obtained. Then, the sliding of an active passive slope will be investigated and results will be compared with analytical values obtained by a limit equilibrium theory. Finally, the failure of a fractured slope subject to a excavation process will be analysed.

6.3.1 Shear Box Test

The shear box test solved below is very simple and used as a benchmark to verify the effects caused by the fluid pressurization in the fracture. The aim is to check that the resultant normal force acting in the bottom of the block is decreased by the fluid pressure of the pipe, causing the block to slide more easily as a result of the reduction in the friction force.

In the example, a block with dimensions of 0.1 x 0.02 metres is compressed against a rigid surface with dimensions of 0.2 x 0.02 metres. Both have been assumed to have a unit thickness. Firstly, a normal load of 100000 N acts on the block. Then, a tangential force of 420000 N is slowly applied on the left side of the block in order to initiate its sliding, as shown in Figure 6.3.

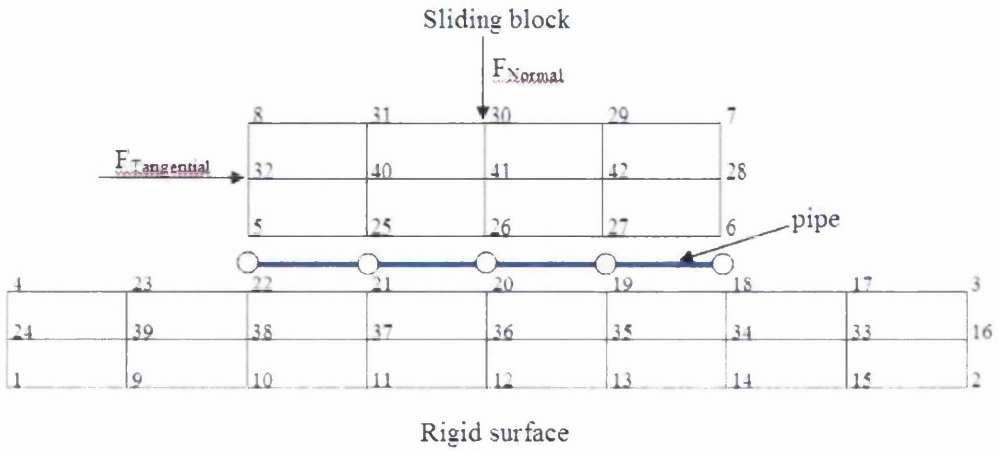

Figure 6.3: Layout of the shear box test.

Three different cases have been investigated. In the first case, the fluid is not pressurized. Block and rigid surface are impermeable materials. Then, in the second case, a constant pressure of 0.25 MPa prescribed for all pipe

nodes. Block and rigid surface are still considered impermeable materials. Finally, in the last case a constant pressure of 0.25 MPa is prescribed for all pipe. Block and rigid surface nodes are now considered permeable materials.

The contact is based on a penalty formulation and a Coulomb friction law is employed to model the frictional sliding. The material and contact properties used are shown in Table 6.1.

Material Properties	Value
Young Modulus	6.5 GPa
Poisson	0.24
Mass density	1070 kg/m^3
Contact Properties	Value
Normal stiffness	2.4 GPa/m
Tangential stiffness	0.24 GPa/m
Friction coefficient	0.78

Table 6.1: Material and contact data for the shear box test.

A very simple analytical solution can be obtained as described below:

- Calculate total (σ_N) and effective ($\sigma_N^{'}$) normal stress.

$$\begin{aligned} \sigma_N &= F_N \ / \ LT = 100000 \ / \ 0.1 \ 1 = 1.0 \ MPa \\ \sigma_N^{'} &= \sigma_N - p_{nf} = 1.0 - 0.25 = 0.75 \ MPa \end{aligned} \tag{6.3}$$

  where, F_N is the normal force, L is the length of the block, T is the thickness and p_{nf} is the fluid pressure.

- Calculate total (τ) and effective ($\tau^{'}$) shear failure.

$$\begin{aligned} \tau &= \mu \ \sigma_N = 0.78 \ 1.0 = 0.78 \ MPa \\ \tau^{'} &= \mu \ \sigma_N^{'} = 0.78 \ 0.75 = 0.586 \ MPa \end{aligned} \tag{6.4}$$

- Calculate maximum tangential displacements (u) and ($u^{'}$).

$$\begin{aligned} u &= \tau \ / K_T = 0.78/240 = 0.00325 \ m \\ u &= \tau^{'} \ / K_T = 0.586/240 = 0.00244 \ m \end{aligned} \tag{6.5}$$

In Figure 6.4 for case 1, a good agreement with the analytical solution has been obtained in the middle of the block (node 26) as expected. The shear stress value for 0.00326 m of tangential displacement is 0.782 MPa, getting very close to the analytical values obtained in Equations 6.5 and 6.4

respectively. In the adjacent sides to the middle of the block, the deformation has been responsible for the differences in the shear stress and displacement seen.

The results for cases 2 and 3 shown in Figures 6.5 and 6.6 respectively, confirms that the pressure in the pipe is responsible for a decrease in the effective normal stress, consequently reducing the friction force acting in the interface between the block and the rigid surface. In the 2 cases the effective tangential stress for 0.00244 of tangential displacement is 0.586 MPa, showing a very close match to the analytical values obtained in Equations 6.5 and 6.4 respectively.

Excellent accuracy has been achieved in this simple example.

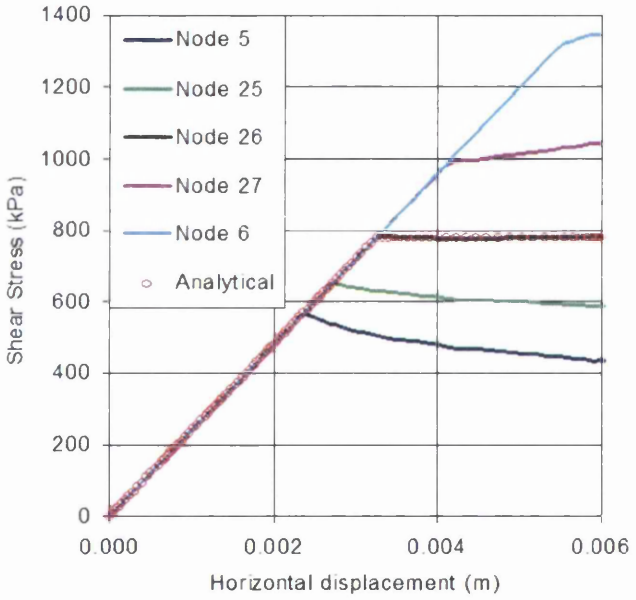

Figure 6.4: Shear stress versus tangential displacement in case 1.

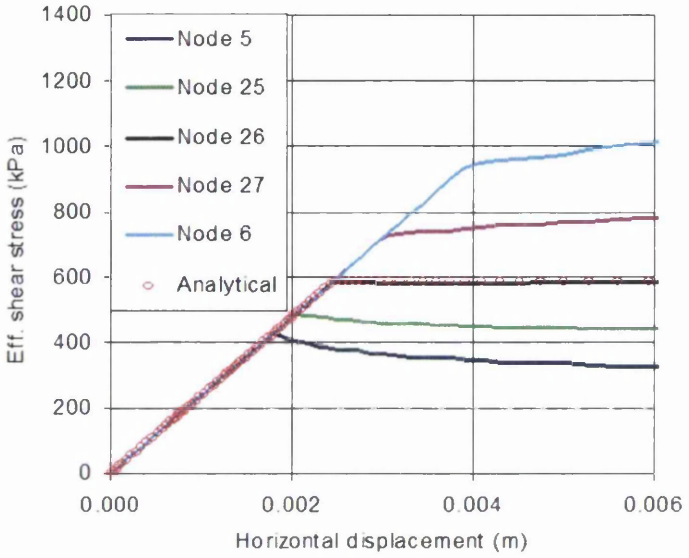

Figure 6.5: Shear stress versus tangential displacement in case 2.

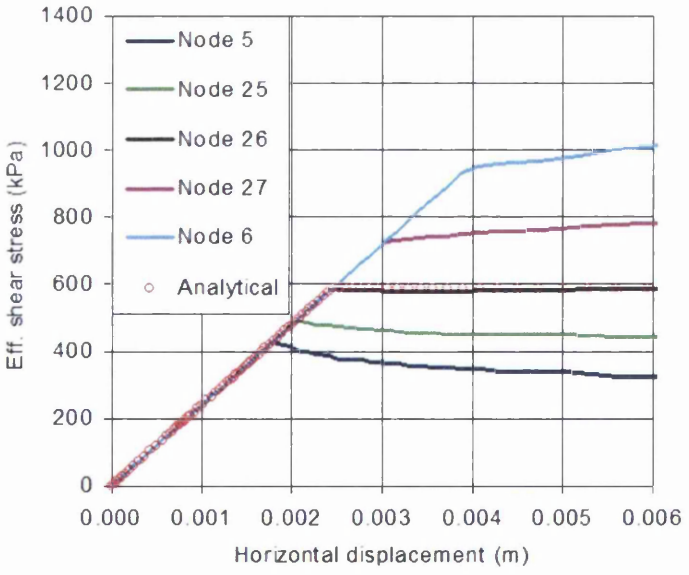

Figure 6.6: Shear stress versus tangential displacement in case 3.

6.3.2 Sliding of an active passive slope

In this example a solid-fluid interaction analysis is carried out in the assessment of the stability of a loose rockfall in a slope where the fissure is filled with water to the top and allowed to drain to the end of the fracture. The free surface is considered to be at the top of the slope and a gravity load is applied. The total time of the evaluation is 70 s (seconds), where in the first 10 s the rock mass is not allowed to have any displacement in the horizontal direction. Then, in the following twenty seconds the constraints have been progressively released. Finally, the block is free to slide. The boundary conditions applied and the layout of the problem are shown in Figure 6.7.

The numerical model consists of a 2-D plane strain analysis with linear triangular elements employed for the rockfall and main slope, and a 1-D linear element for the network flow. The constitutive model is a Rankine rotating crack formulation with softening. The contact is based on a penalty formulation and the frictional sliding is controlled by the Coulomb friction law.

Two different cases have been investigated where the rockfall and main slope are considered impermeable rock. First, the frictional sliding is controlled by a Coulomb friction law where cohesion at the interface is not taken into account. Then, a degree of complexity is added when the cohesion between the rock and main slope is considered in the analysis of the slope stability.

Case 1 : Cohesion in the interface between the rockfall and main slope is neglected.

The aim is to check the influence of the water pressure in a discontinuity between the main slope and rockfall using a network flow analysis. The main aims are to calibrate the numerical model for different values of factor of safety (*FOS*), and also, to obtain a better understanding of the water pressure's effect in the sliding of a rockfall. The focus has been directed at the initiation of sliding, due to a limitation in the analysis for large movements. The variation in the *FOS* is obtained through a modification in the friction angle (ϕ) in the interface of the fracture, see details in Table 6.2. The material properties and contact data used are shown in Table 6.3. Finally, the input parameters necessary for the network flow analysis are given in Table 6.4.

Friction angle (°)	*FOS*
63.0	1.00
65.2	1.10
68.7	1.30
71.3	1.50

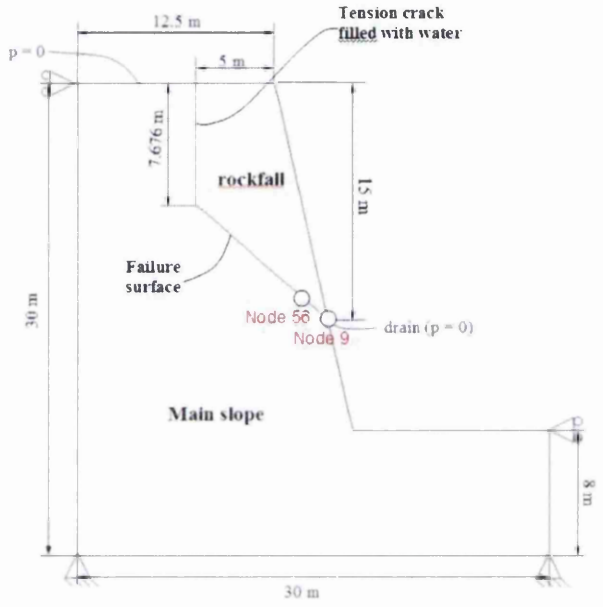

Figure 6.7: Layout of the problem.

Table 6.2: Factors of safety (FOS) evaluated for different friction angles.

Main slope		Rockfall	
Material Properties	Value	Material Properties	Value
Young Modulus	50.0 GPa	Young Modulus	20.0 GPa
Poisson	0.2	Poisson	0.25
Mass density	2600 kg/m^3	Mass density	2500 kg/m^3
Tensile strength	20 MPa	Tensile strength	0.35 MPa
Energy release	6000 Pa.m	Energy release	200 Pa.m
Contact Properties	Value	Contact Properties	Value
Normal stiffness	3.0 GPa/m	Normal stiffness	3.0 GPa/m
Tangential stiffness	0.3 GPa/m	Tangential stiffness	0.3 GPa/m

Table 6.3: Material properties and contact data.

Network flow data	Value
Normal stiffness of the fracture	5.0 GPa/m
Fluid compressibility	0.5 GPa^{-1}
Dynamic viscosity of the fluid	0.001 Pa.s
Residual aperture	0.05 mm
Initial aperture tensile crack	3.0 mm
Initial aperture failure surface	0.3 mm
Initial fluid pressure	0.0 Pa
Fluid mass density	1000 kg/m^3
Gravitational acceleration	9.81 m/s^2

Table 6.4: Input data for the network flow problem in case 1.

Figures 6.8 to 6.16 show the results obtained from the network flow analysis for the range of ϕ, as given in Table 6.2. They provide a good insight into the discussion that will follow.

For ϕ value of 63°, it can be seen that the friction force acting at the contact surface has been overcome by the tangential forces, Figure 6.13 (a). This limit condition implies that a failure point has been reached and the rock mass at that particular state begins to slide. However, for ϕ values of 65.2°, 68.7° and 71.3° (Figures 6.14(a) to 6.16(a)), a limit equilibrium condition takes place, characterizing a stable condition. This behavior is emphasized through the verification of the vertical displacements in Figure 6.8.

Figures 6.9 and 6.10 show an evolution in time of the water pressure along the tensile crack and failure surface respectively. The corner between the tensile crack and the failure surface is chosen as the initial crack length (0 m). Consequently, the total length is based on the top of the slope (7.676 m) in the case of the tensile crack and on the point where the drain is located (11.15 m) in the case of the failure surface. The pressure distribution along the tensile crack has a gradient increase toward the failure surface. Then a linear decrease occurs until the failure surface daylights the slope face. This is in agreement with the value estimated by the theory as described in Subsection 6.2.2.

Also, a decrease in the water pressure is shown (path A to B) for all ϕ values, as illustrated in Figures 6.13 to 6.16, item (c). This drop in the fluid pressure is caused by the abrupt sliding of the block, which increases the aperture of the fissure in the tensile crack region. Due to the large volume of water in the tensile crack in comparison to that found in the failure surface, a more sensitive change in pressure is noticed in the failure surface, as shown in Figures 6.9 and 6.10. Then, the water pressure starts to increase (path B to C) for all ϕ values, as illustrated in Figures 6.13 to 6.16, item (c).

The increase in pressure is given by a more uniform movement of the slope allowing the volume of water in the failure surface to be refilled.

In Figures 6.13 to 6.16, items (d) and (b), it can be observed that the effective normal stresses in the beginning of the failure surface is zero, consequently, it affects the effective tangential stresses leading to a redistribution of the friction forces along the failure surface. This results from the fact that the contact between the main slope and failure surface has been lost, this is attributed to the lateral and uplift forces applied to the rockfall. For this particular friction model these effects have been compensated by the redistribution of the forces. However, when a more complex contact model in which cohesion is taken into account is considered, it is believed that these effects will be more important in the evaluation of the slope stability. This will be checked in the following case.

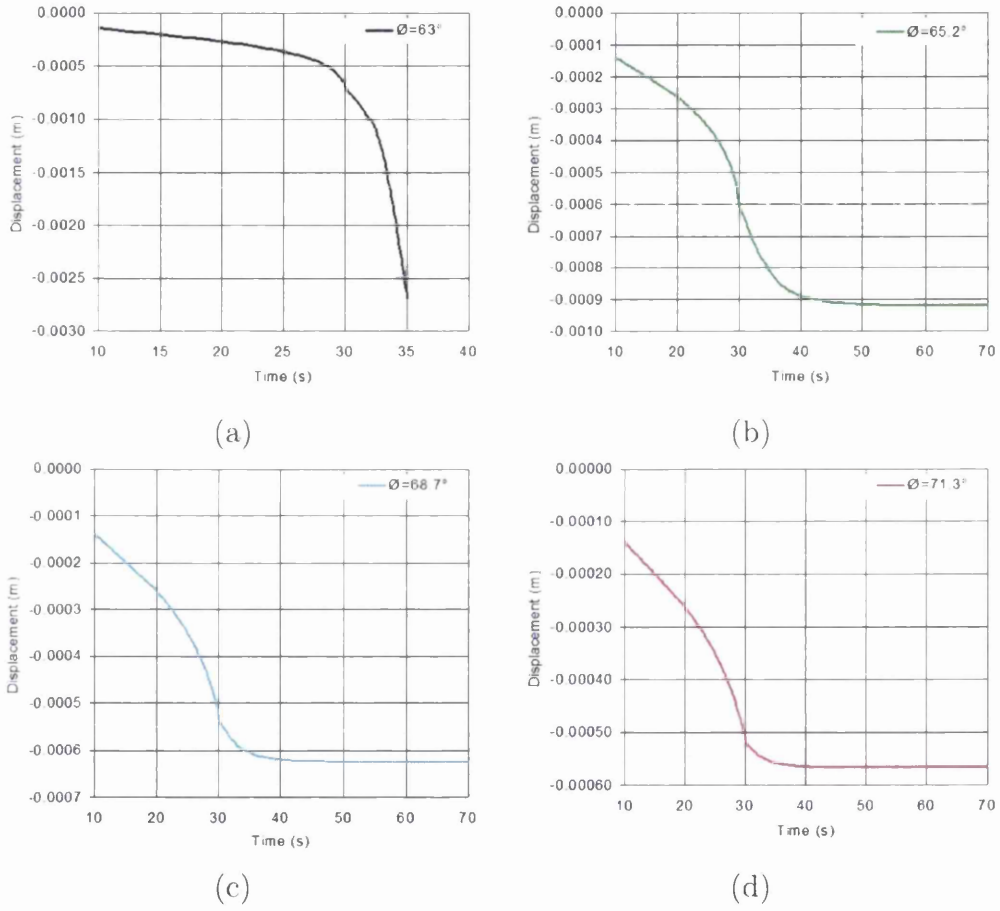

Figure 6.8: Progression of the vertical displacement at node 9 for different cohesion coefficients and time evaluated: (a) $\phi = 63.0°$, time = 35 s. (b) $\phi = 65.2°$, time = 70 s. (c) $\phi = 68.7°$, time = 70 s. (d) $\phi = 71.3°$, time = 70 s.

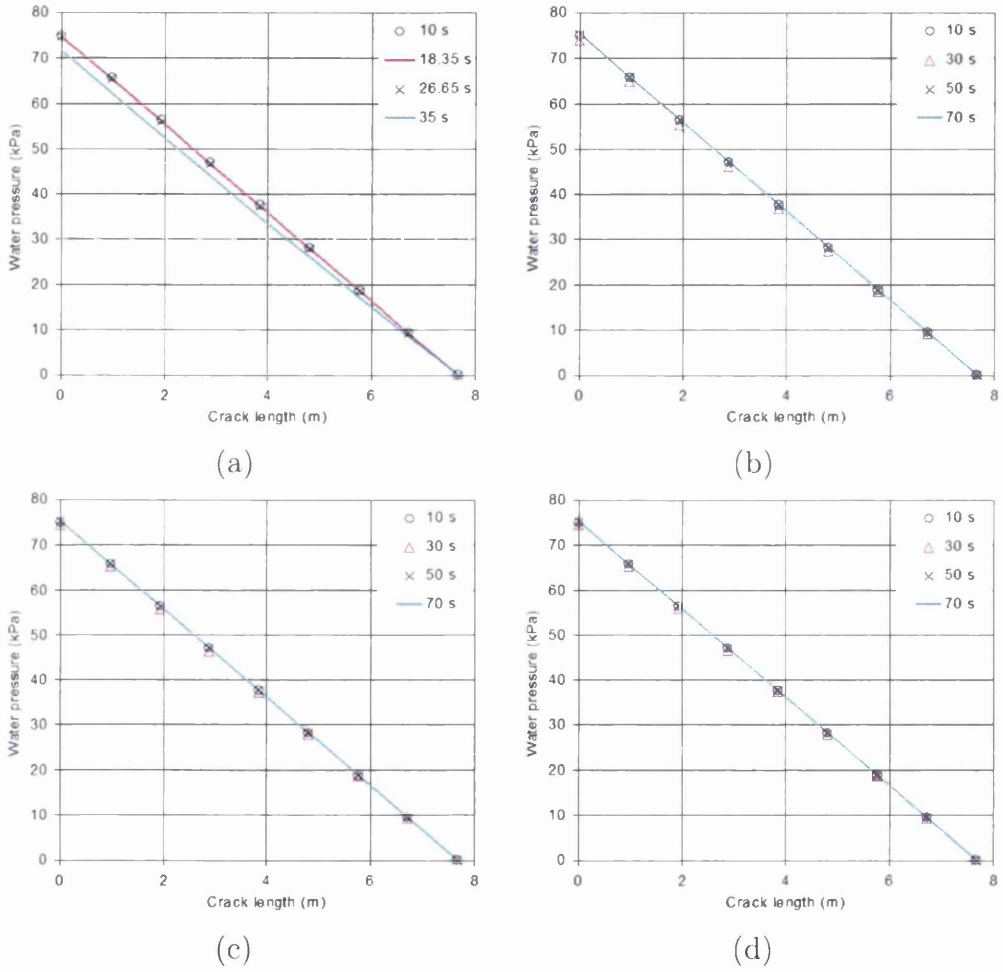

Figure 6.9: Water pressure distribution along the tensile crack. (a) $\phi = 63.0°$, time = 35 s. (b) $\phi = 65.2°$, time = 70 s. (c) $\phi = 68.7°$, time = 70 s. (d) $\phi = 71.3°$, time = 70 s.

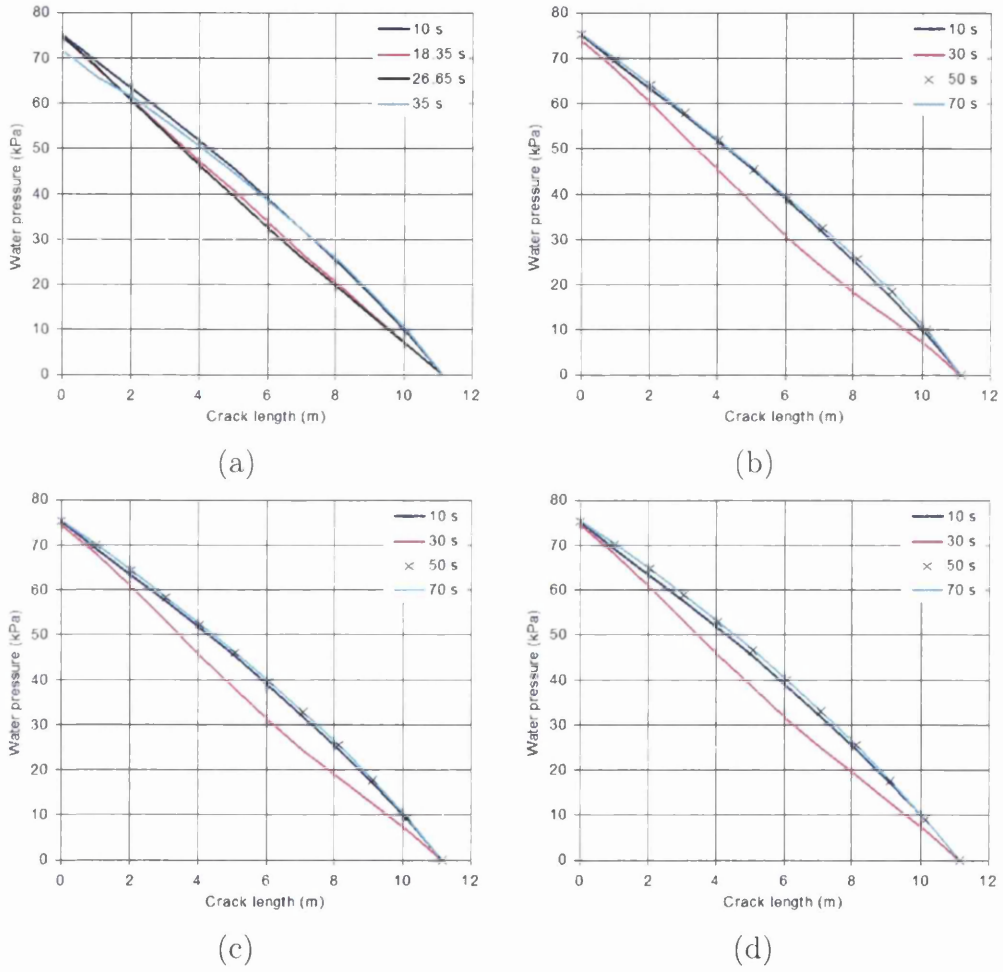

Figure 6.10: Water pressure distribution along the failure surface. (a) $\phi = 63.0°$, time = 35 s. (b) $\phi = 65.2°$, time = 70 s. (c) $\phi = 68.7°$, time = 70 s. (d) $\phi = 71.3°$, time = 70 s.

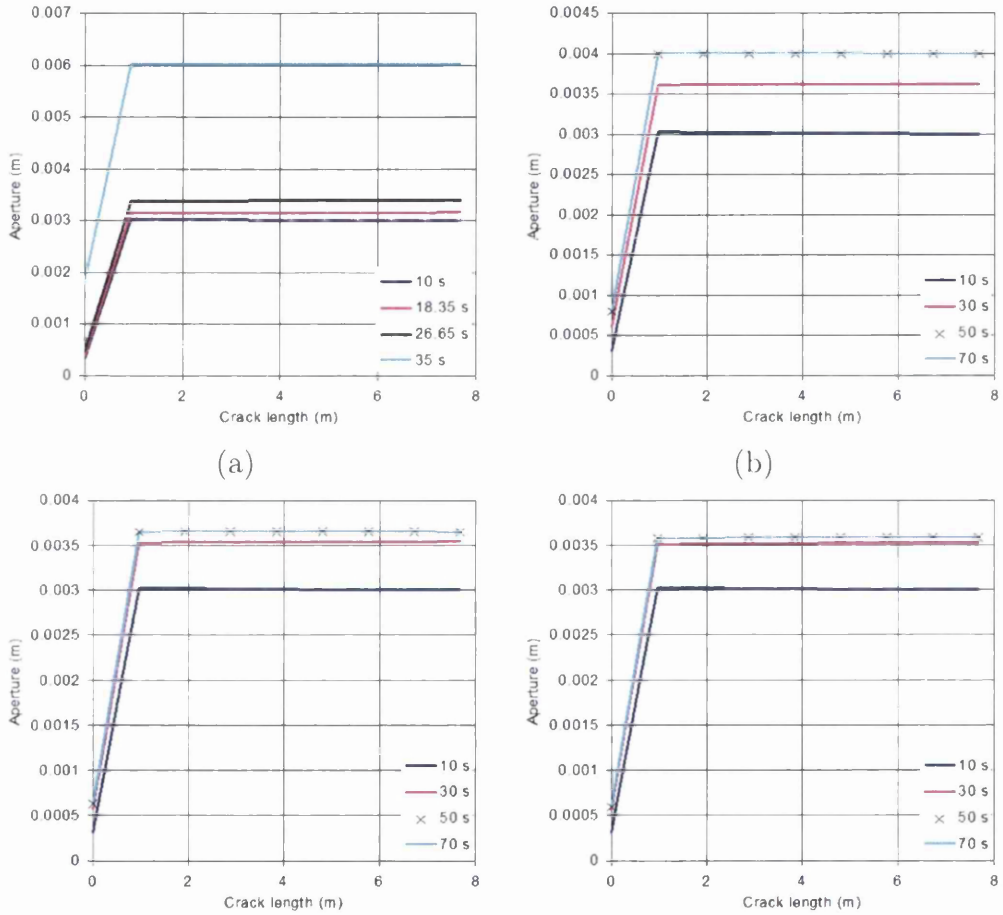

Figure 6.11: Aperture distribution along the tensile crack. (a) $\phi = 63.0°$, time = 35 s. (b) $\phi = 65.2°$, time = 70 s. (c) $\phi = 68.7°$, time = 70 s. (d) $\phi = 71.3°$, time = 70 s.

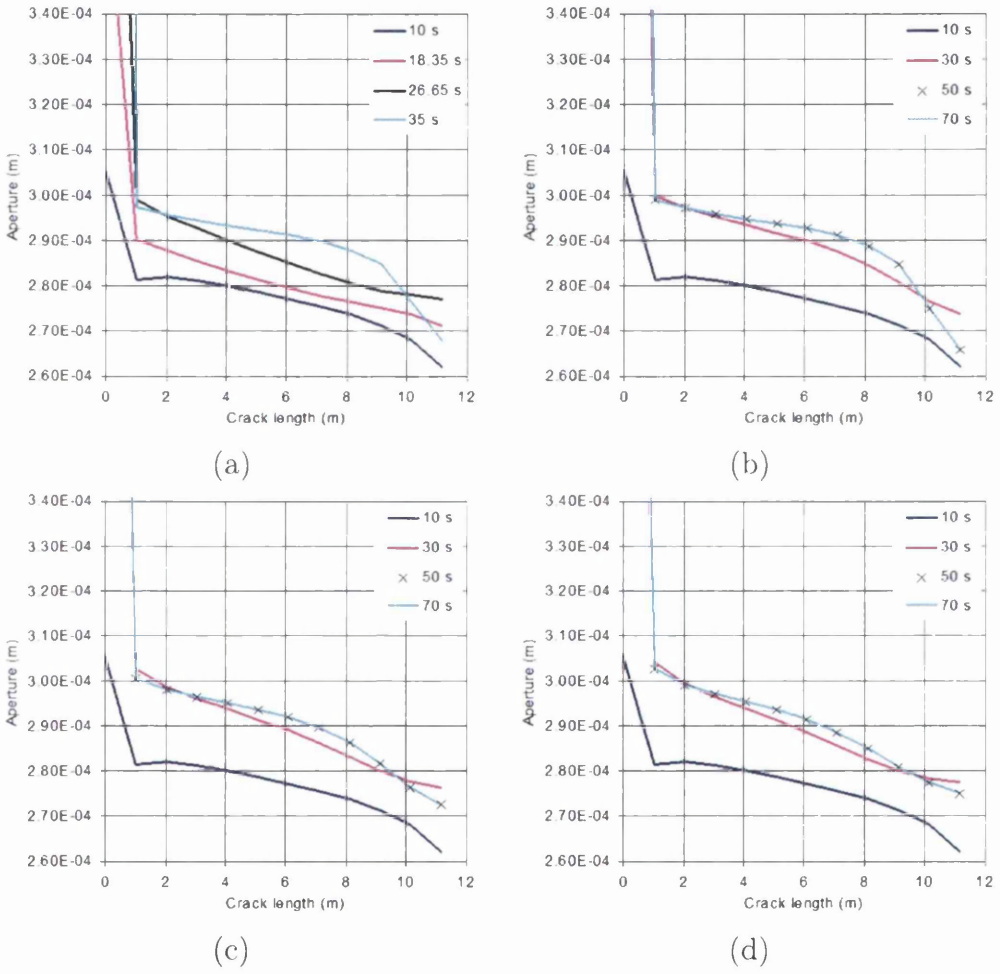

Figure 6.12: Aperture distribution along the failure surface. (a) $\phi = 63.0°$, time = 35 s. (b) $\phi = 65.2°$, time = 70 s. (c) $\phi = 68.7°$, time = 70 s. (d) $\phi = 71.3°$, time = 70 s.

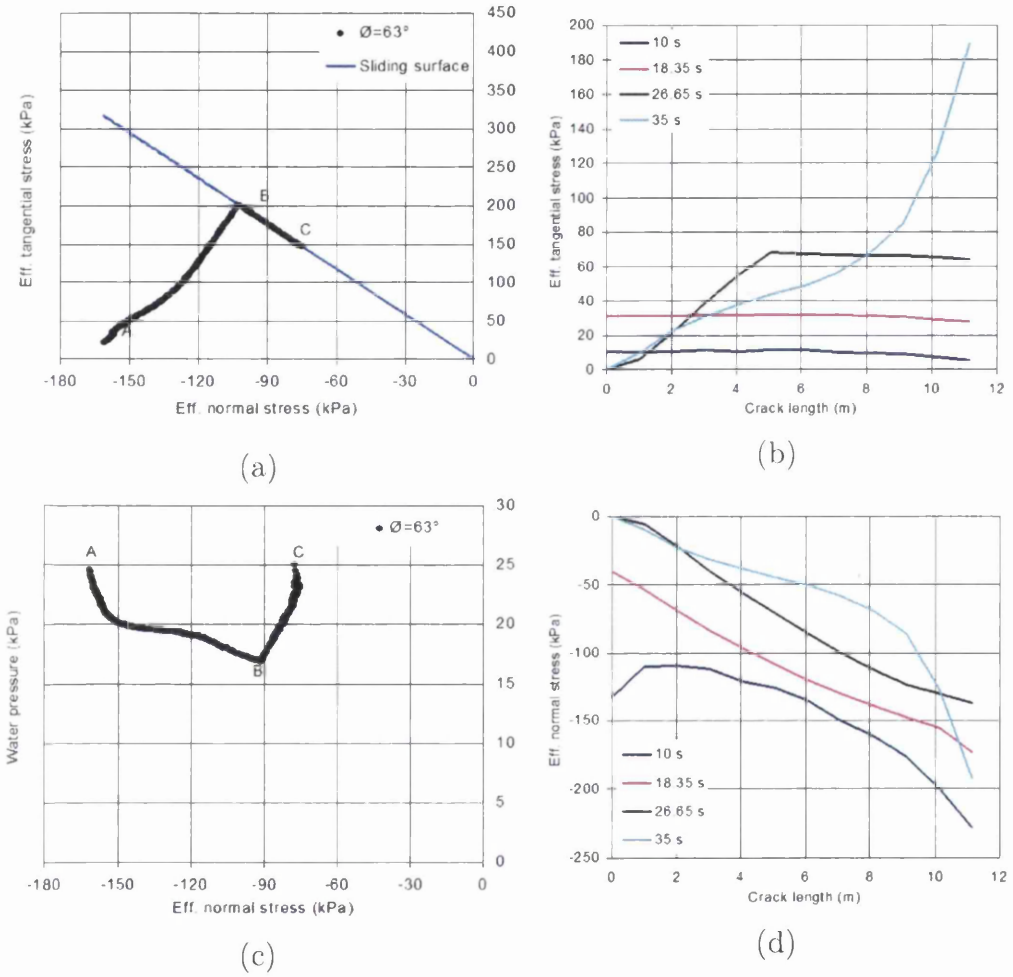

Figure 6.13: Shear strength characteristics and water pressure distribution for $\phi = 63.0°$: (a) Effective tangential stress vs effective normal stress at node 56 during 35 s of analysis time. (b) Effective tangential stress distribution along the failure surface. (c) Water pressure as a function of the effective normal stress at node 56 during 35 s of analysis time. (d) Effective normal stress distribution along the failure surface.

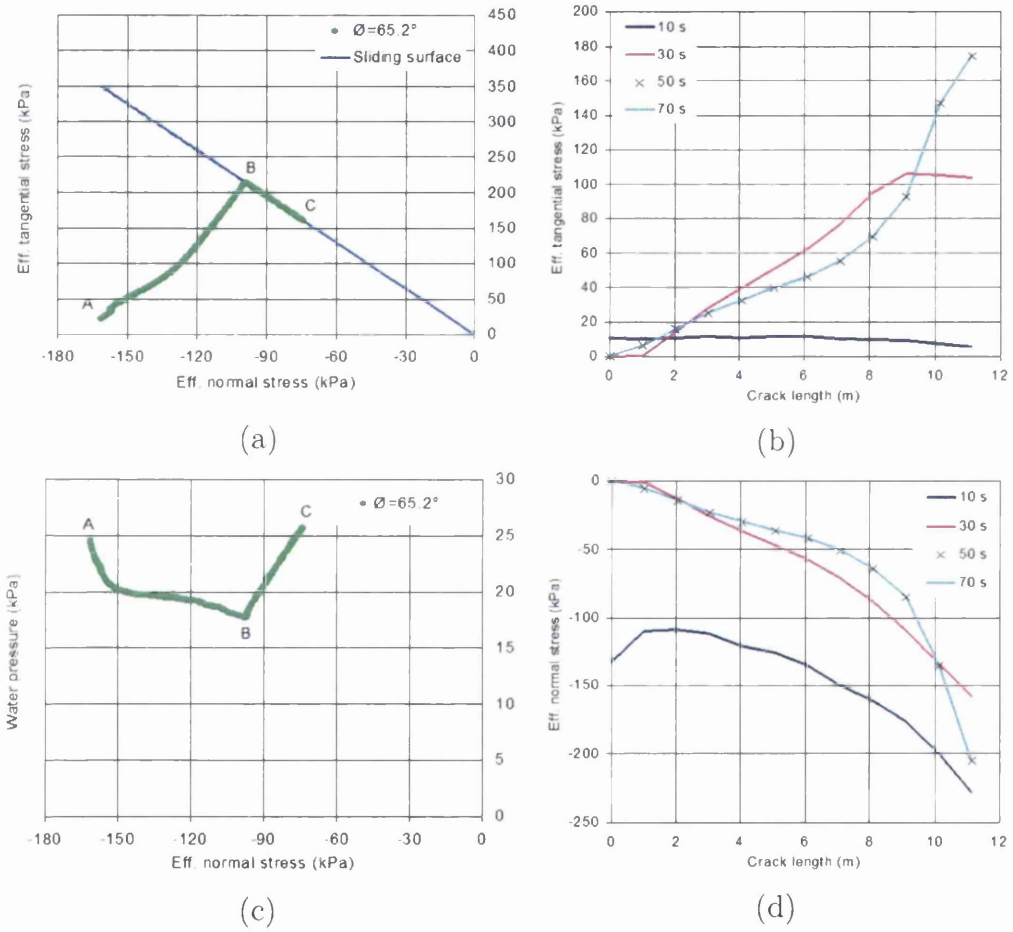

Figure 6.14: Shear strength characteristics and water pressure distribution for $\phi = 65.2°$ (a) Effective tangential stress vs effective normal stress at node 56 during 70 s of analysis time. (b) Effective tangential stress distribution along the failure surface. (c) Water pressure as a function of the effective normal stress at node 56 during 70 s of analysis time. (d) Effective normal stress distribution along the failure surface.

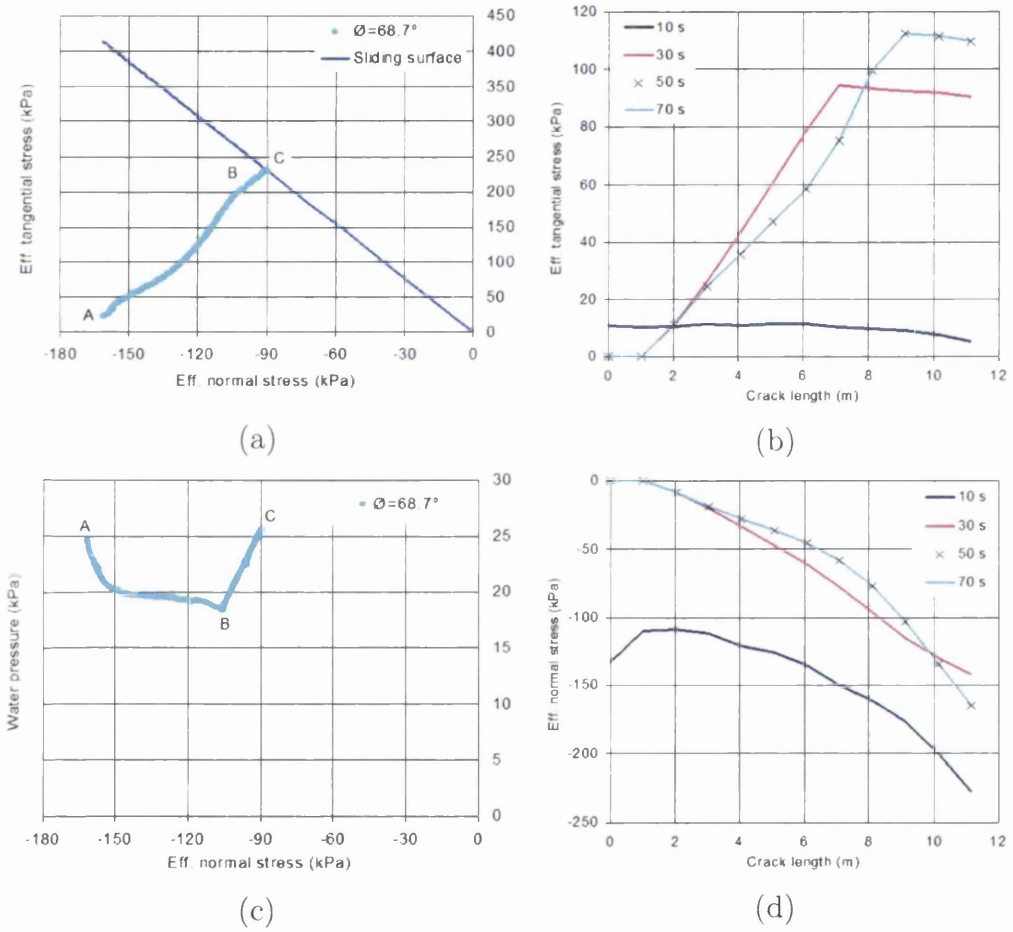

Figure 6.15: Shear strength characteristics and water pressure distribution for $\phi = 68.7°$ (a) Effective tangential stress vs effective normal stress at node 56 during 70 s of analysis time. (b) Effective tangential stress distribution along the failure surface. (c) Water pressure as a function of the effective normal stress at node 56 during 70 s of analysis time. (d) Effective normal stress distribution along the failure surface.

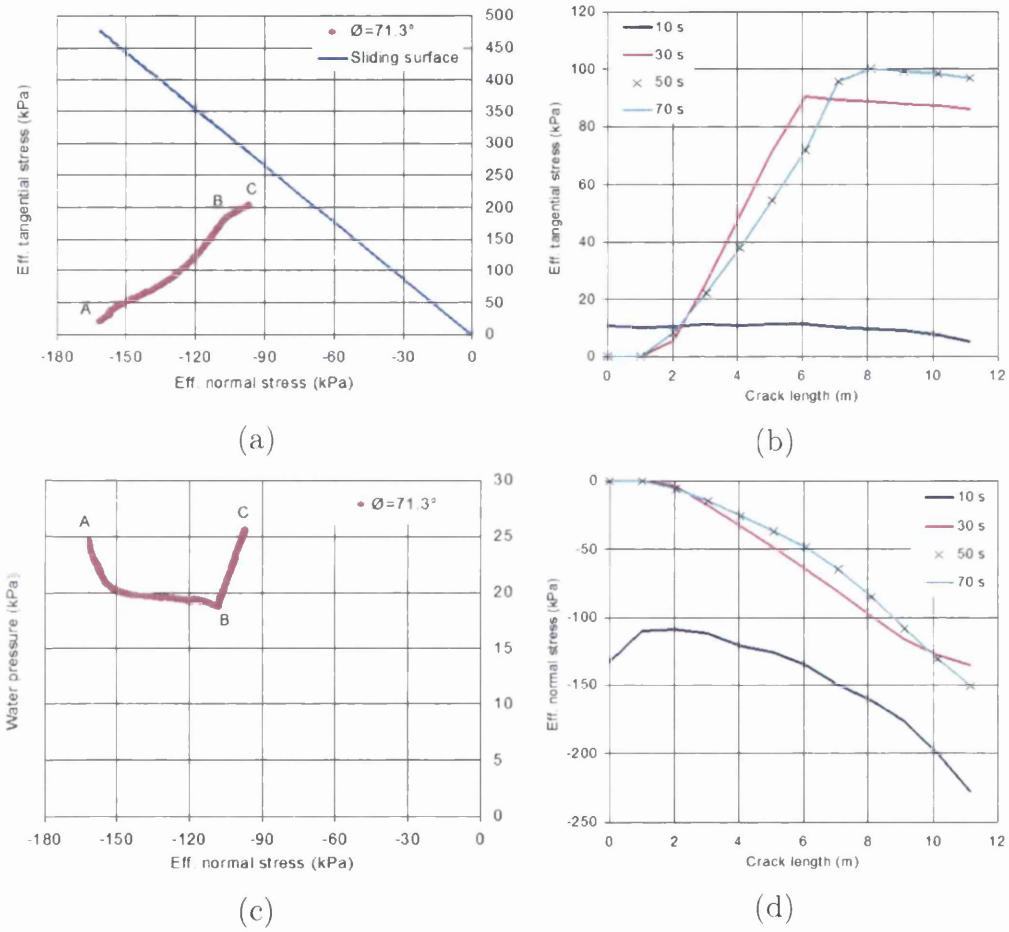

Figure 6.16: Shear strength characteristics and water pressure distribution for $\phi = 63.0°$ (a) Effective tangential stress vs effective normal stress at node 56 during 70 s of analysis time. (b) Effective tangential stress distribution along the failure surface. (c) Water pressure as a function of the effective normal stress at node 56 during 70 s of analysis time. (d) Effective normal stress distribution along the failure surface.

Case 2 : Cohesion in the interface between the rockfall and main slope are considered.

A similar investigation, as described in the previous case, is carried out in the following problem. The main goal is to compare the results obtained in the previous analysis against the ones presented below. The difference arises from the fact that the cohesion between the main slope and rockfall are considered at this time. This implies that in the interfaces between rockfall and main slope where the contact forces have been lost as shown in the previous case, the resisting forces will be more affected.

The *FOS* will now be a function of the cohesion coefficients as described in Table 6.5 and the friction angle is assumed to be a constant value of 30°. The material, contact properties and input parameters used in the analysis are exactly the same as given by Tables 6.3 and 6.4 respectively.

Cohesion coefficient (kPa)	*FOS*
85	1.00
97	1.10
121	1.30
145	1.50

Table 6.5: Factors of safety (*FOS*) evaluated for different cohesion coefficients.

For c values of 85 kPa and 97 kPa the sliding process occurs more abruptly compared to c of 121 kPa and 145 kPa, which causes a higher drop in the water pressure. First, there is a decrease of the fluid pressure in the tensile crack which is followed by a drop in the water pressure in the failure surface. It is important to notice that a small change in the water pressure in the tensile crack region causes a considerable drop in the fluid pressure in the failure surface, as the volume of water in the failure surface is smaller than in the tensile crack, which becomes more sensitive to variations. Following that, a more uniform sliding process occurs, causing the rate of volume change in the fissure to be very small, allowing a proportional refilling procedure to occur. For c values of 85 kPa and 97 kPa, the increase in water pressure is enough to generate an unstable condition, resulting in the sliding of the rock mass. On the other hand, even the addition of the uplift force generated by the water pressure has been shown to be insufficient to affect the stability of the block for c values of 121 and 145 kPa.

It is well known that the effective normal stress ($\sigma_n^{'}$) is highly affected by changes in water pressure and consequently, the effective tangential stress ($\tau^{'}$) distribution. Items (b) and (d) from Figures 6.22 to 6.25 illustrate this

phenomenon. For all c values, higher tensile forces act in the initial crack length, while, higher compression forces can be seen at the end of the crack length, as a result of the water pressure distribution. Consequently, lower friction forces are found in the initial crack length of the failure surface.

It is important to note that for c of 121 kPa, effective tangential stresses acting in the first 1.014 metres of the failure surface are non-existent, because the high uplift and lateral forces encountered in that region are enough to avoid any contact between the rockfall and main slope. The same behavior can be observed for a c value of 145 kPa.

The results have shown to be in agreement with what is expected. The increase in the value of the cohesion coefficients have led to an increase in the friction force and a consequent reduction in the sliding of the rockfall. Also, the effective normal stress has presented some variations in the behaviour according to changes occurring in the water pressure distribution. Finally, it can be seen that some discrepancies occur in the expected behavior of the slope based on the factor of safety predicted by the limit equilibrium theory and the numerical results obtained, since, no sliding was expected for factors of safety higher or equal to 1.0. The numerical results indicate that failure have occurred for *FOS* of 1.0, 1.2 and 1.3. The main factors that can be attributed to explain the differences are:

1. In the limit equilibrium theory, the water pressure distribution in the failure surface is not considered to suffer any modification during the sliding of the block. However, the numerical results in Figures 6.19, items (c) and (d), have shown that higher values can be found in the failure surface, which leads to a reduction in the resisting force. The explanation arises from the fact that the sliding of the block allows the formation of a higher hydraulic column in the tensile crack. Consequently, a higher gradient of fluid pressure will take place in the failure surface.

2. Deformations occur in the rockfall along the failure surface during the sliding process which affects the effective normal stress distribution, and consequently, the resisting forces, as illustrated in Figures 6.22 and 6.23, items (b) and (d).

3. Numerical instabilities caused by limitations in the formulation used. The velocity of the sliding process is crucial for the stability of the network flow analysis. The formulation used is acceptable for fluid flows occurring at low velocities.

Despite its limitations the proposed framework has been shown to be of particular interest from the practical point of view. The results have shown

that a factor of safety of 1.3 should only be used in situations where the stability of the slopes are not required to remain for long period of time, while, FOS = 1.5 can be used for critical slopes. These values are normally applied in practical situations.

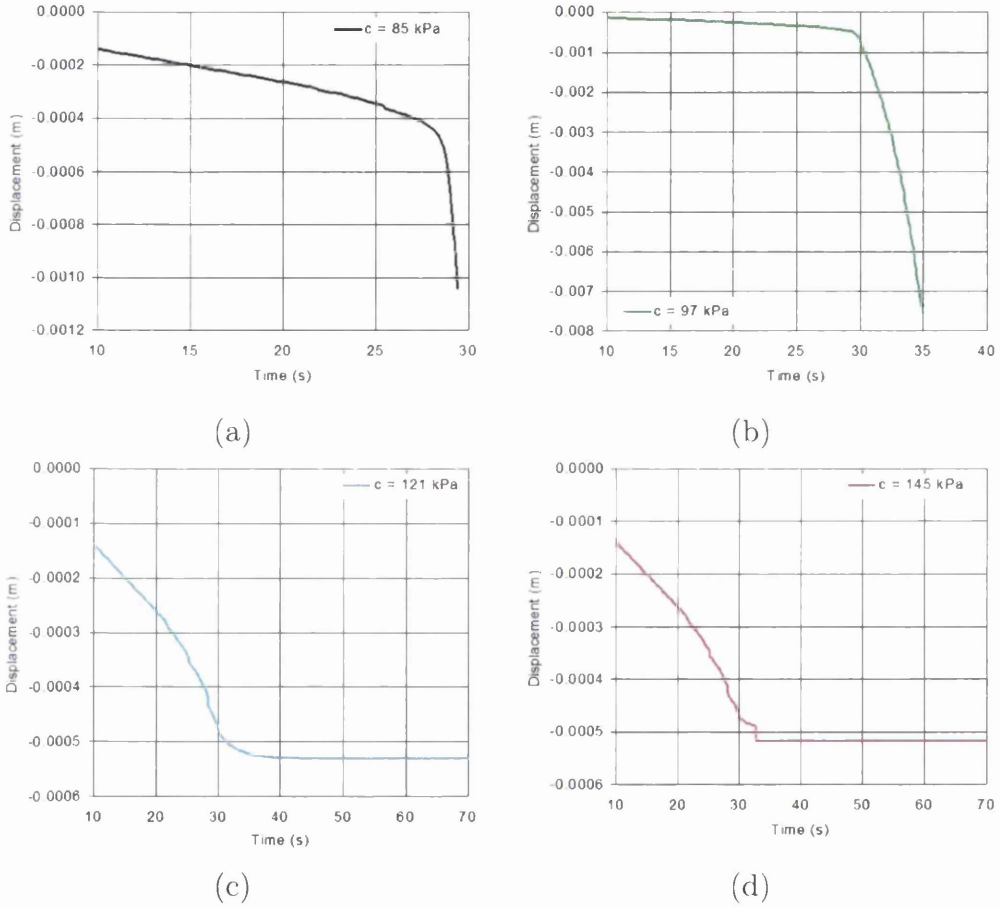

Figure 6.17: Progression of the vertical displacement at node 9 for different cohesion coefficients and time evaluated: (a) $c = 85$ kPa, time = 29.4 s. (b) $c = 97$ kPa, time = 34.95 s. (c) $c = 121$ kPa, time = 70 s. (d) $c = 145$ kPa, time = 70 s.

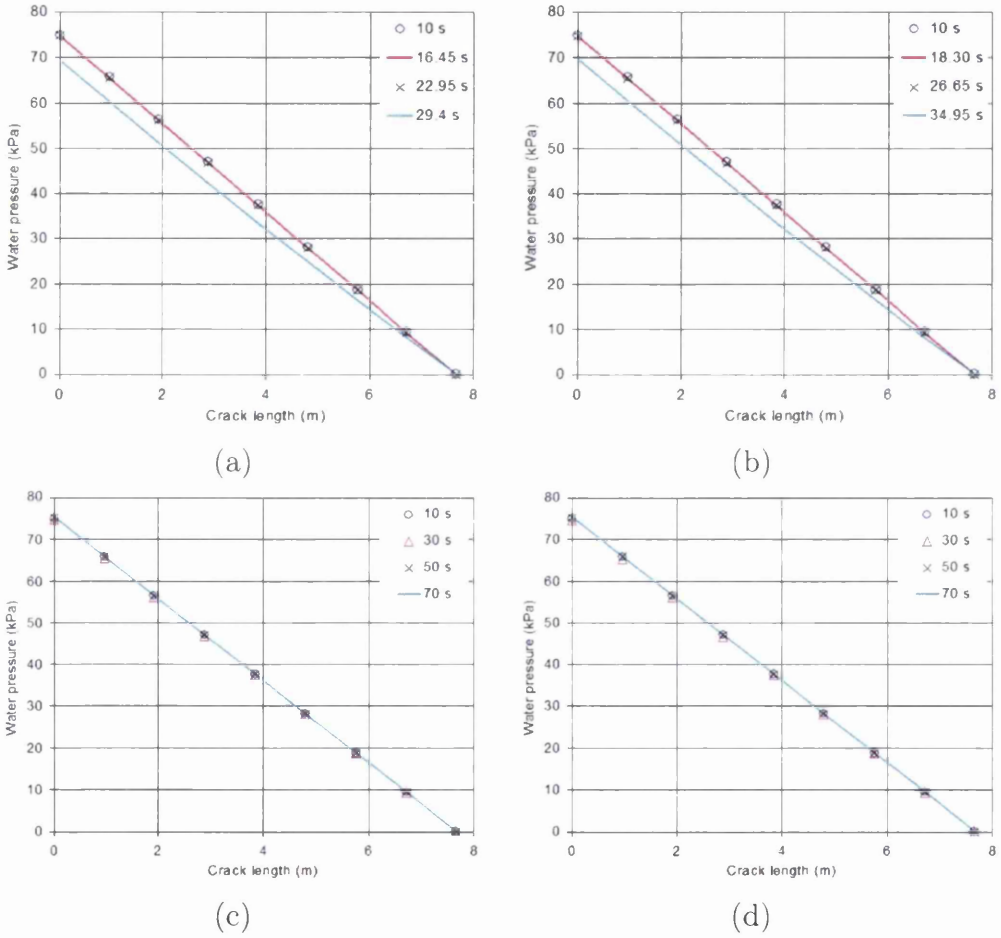

Figure 6.18: Water pressure distribution along the tensile crack. (a) $c = 85$ kPa. (b) $c = 97$ kPa. (c) $c = 121$ kPa. (d) $c = 145$ kPa.

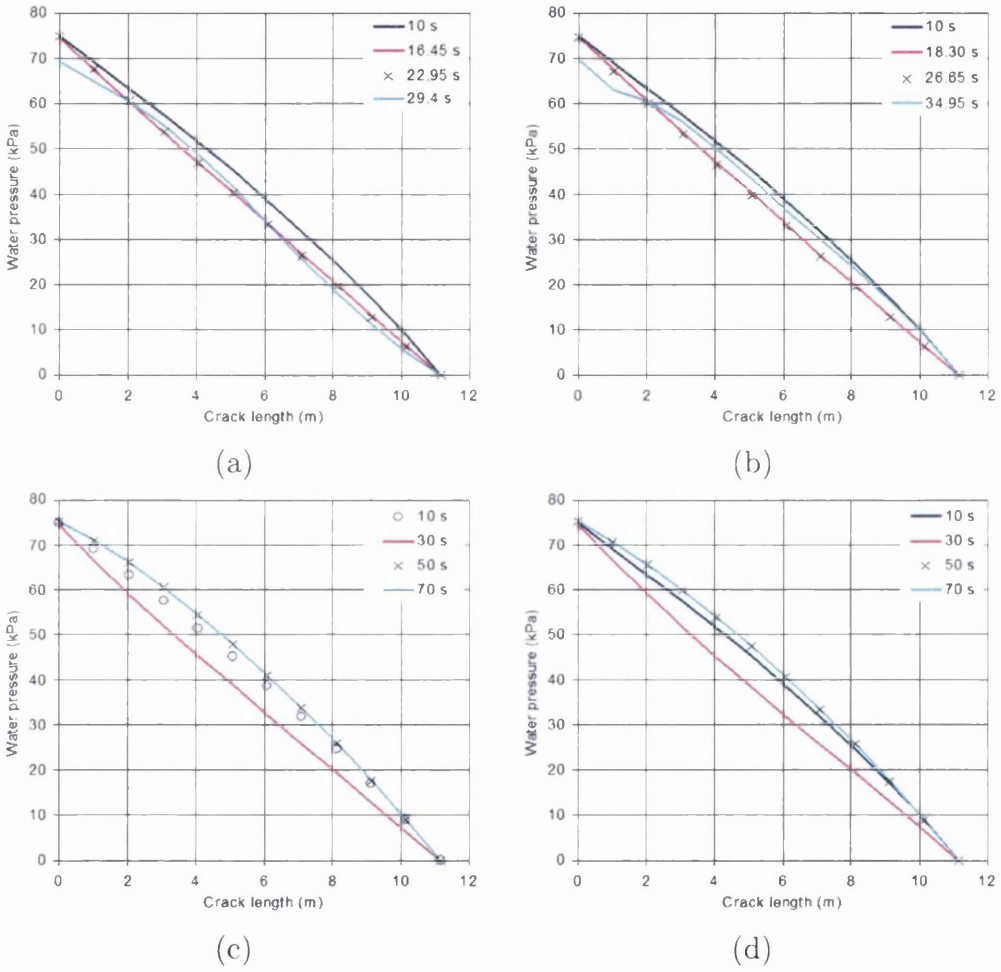

Figure 6.19: Water pressure distribution along the failure surface. (a) c = 85 kPa. (b) c = 97 kPa. (c) c = 121 kPa. (d) c = 145 kPa.

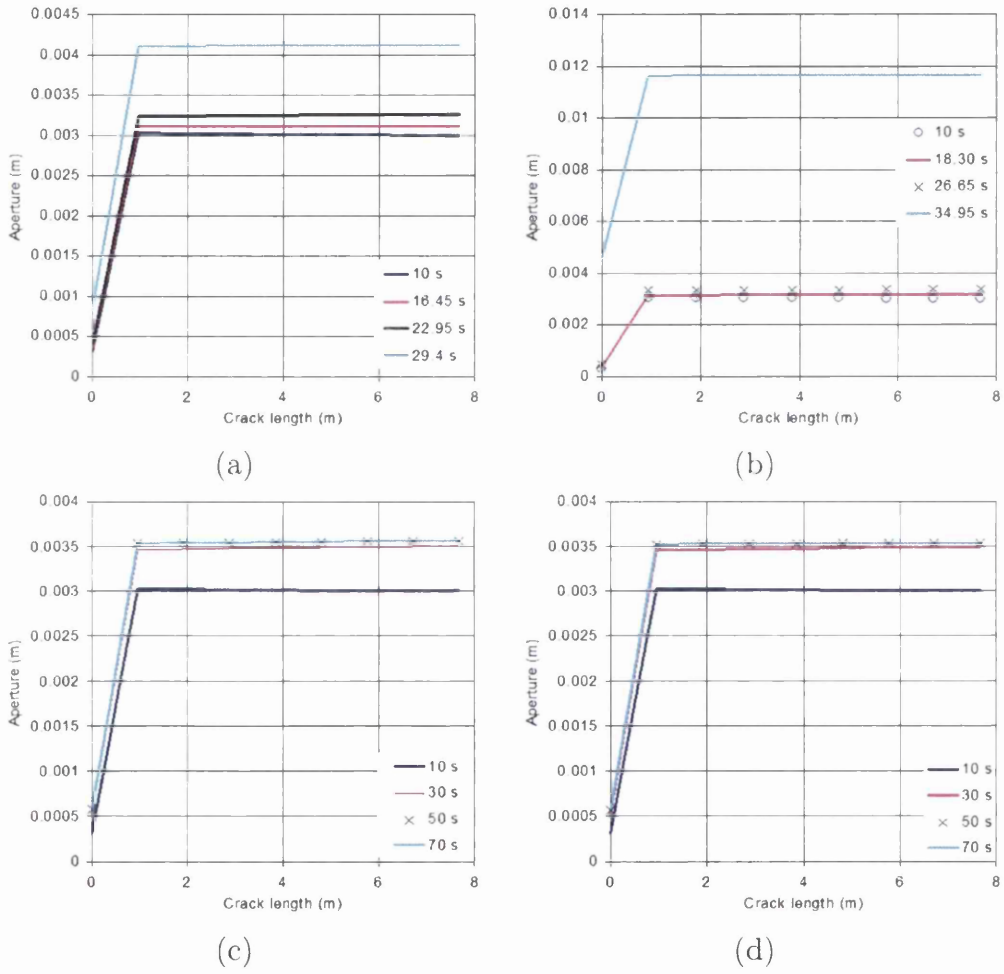

Figure 6.20: Aperture distribution along the tensile crack. (a) $c = 85$ kPa. (b) $c = 97$ kPa. (c) $c = 121$ kPa. (d) $c = 145$ kPa.

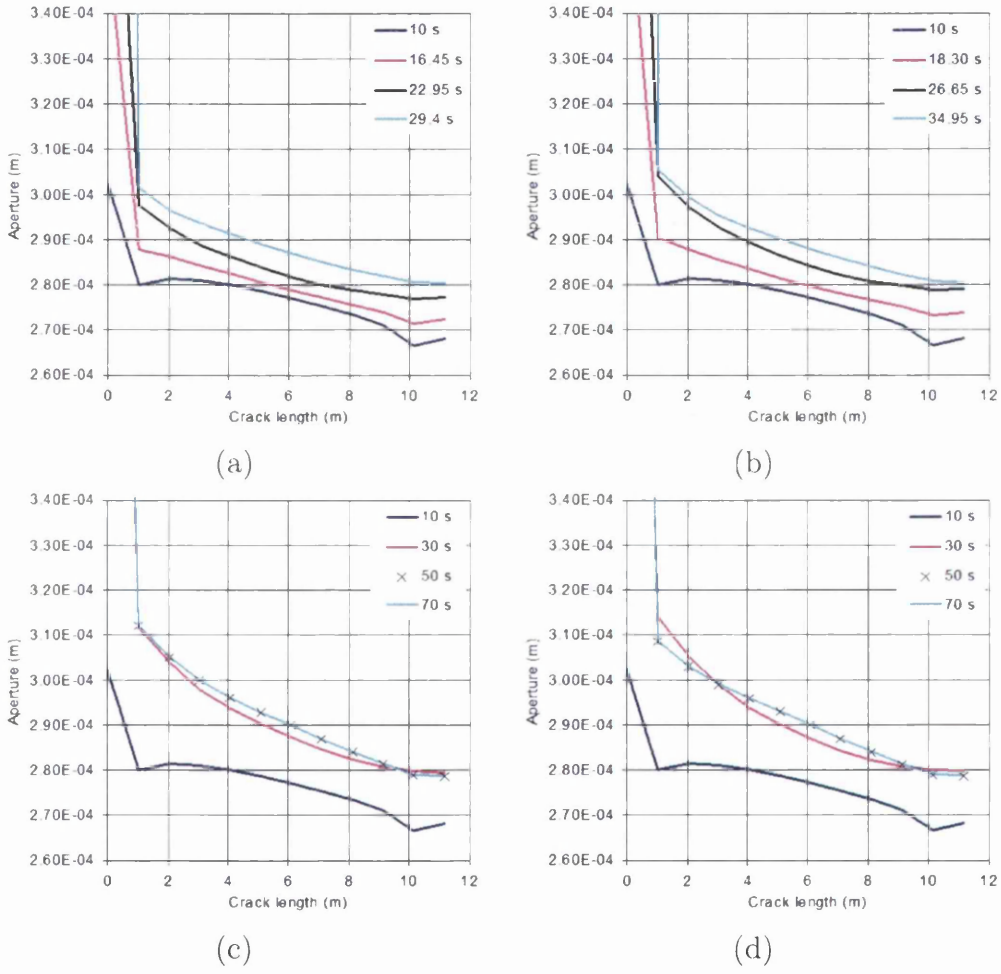

Figure 6.21: Aperture distribution along the failure surface. (a) $c = 85$ kPa. (b) $c = 97$ kPa. (c) $c = 121$ kPa. (d) $c = 145$ kPa.

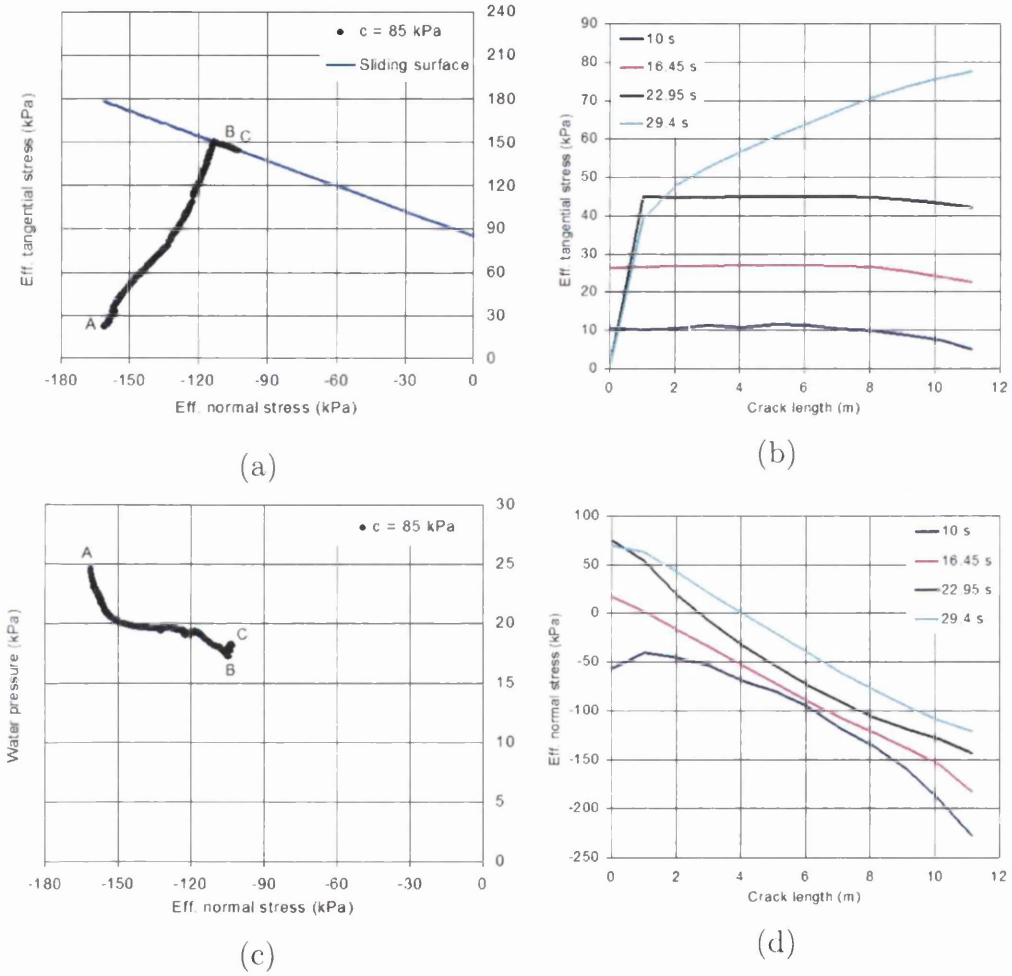

Figure 6.22: Shear strength characteristics and water pressure distribution for $c = 85$ kPa: (a) Effective tangential stress vs effective normal stress at node 56 during 29.4 s of analysis time. (b) Effective tangential stress distribution along the failure surface. (c) Water pressure as a function of the effective normal stress at node 56 during 29.4 s of analysis time. (d) Effective normal stress distribution along the failure surface.

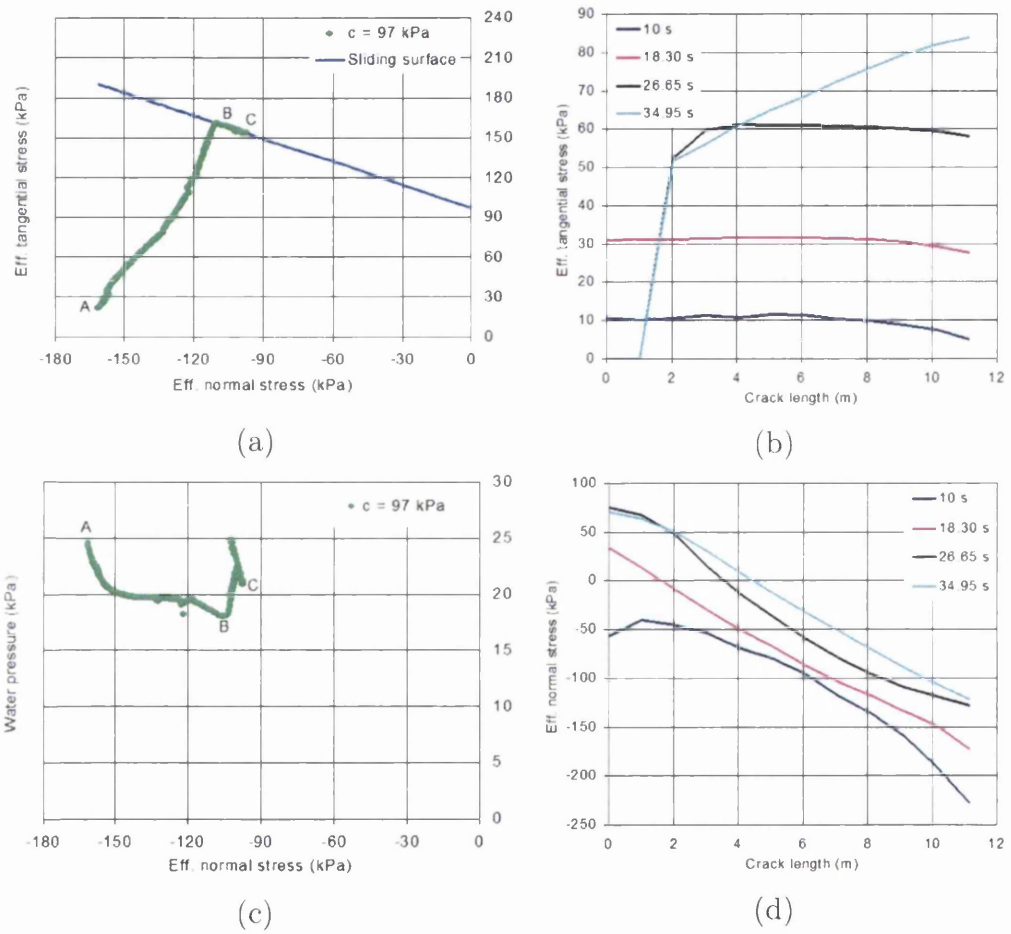

Figure 6.23: Shear strength characteristics and water pressure distribution for $c = 97$ kPa: (a) Effective tangential stress vs effective normal stress at node 56 during 34.95 s of analysis time. (b) Effective tangential stress distribution along the failure surface. (c) Water pressure as a function of the effective normal stress at node 56 during 34.95 s of analysis time. (d) Effective normal stress distribution along the failure surface.

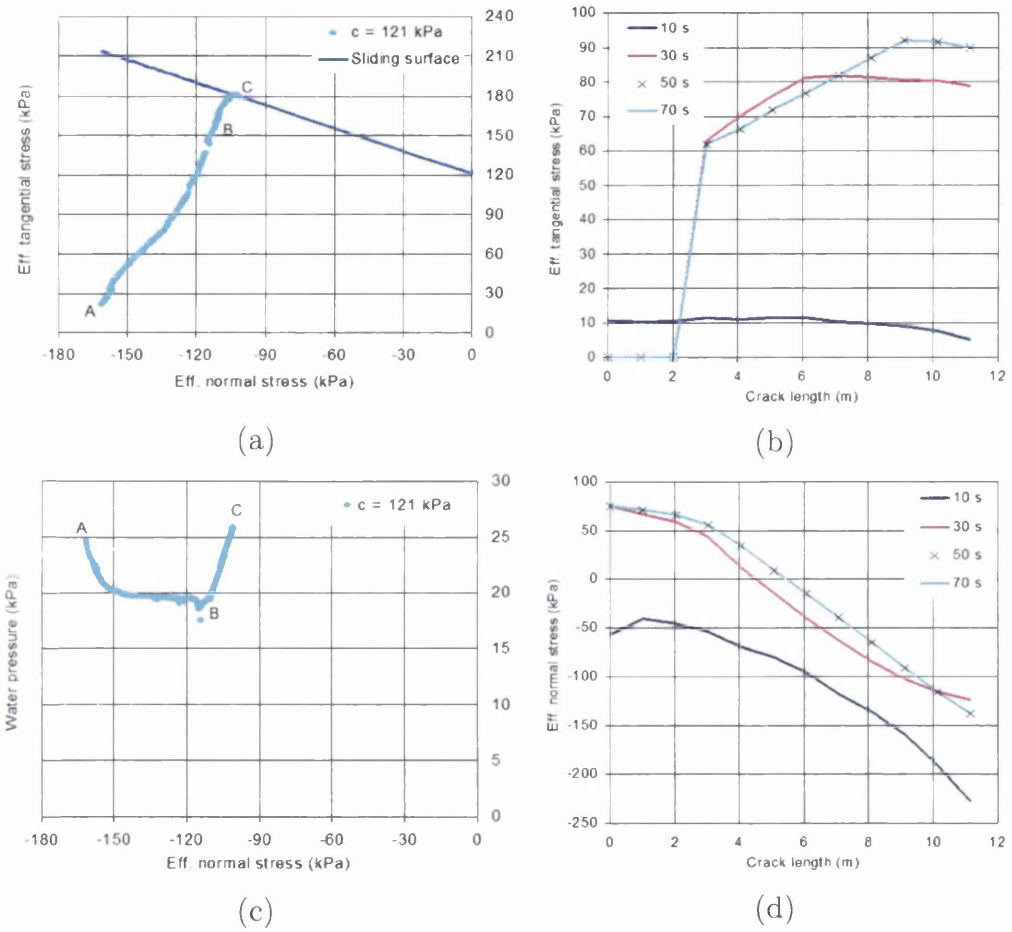

Figure 6.24: Shear strength characteristics and water pressure distribution for $c = 121$ kPa: (a) Effective tangential stress vs effective normal stress at node 56 during 70 s of analysis time. (b) Effective tangential stress distribution along the failure surface. (c) Water pressure as a function of the effective normal stress at node 56 during 70 s of analysis time. (d) Effective normal stress distribution along the failure surface.

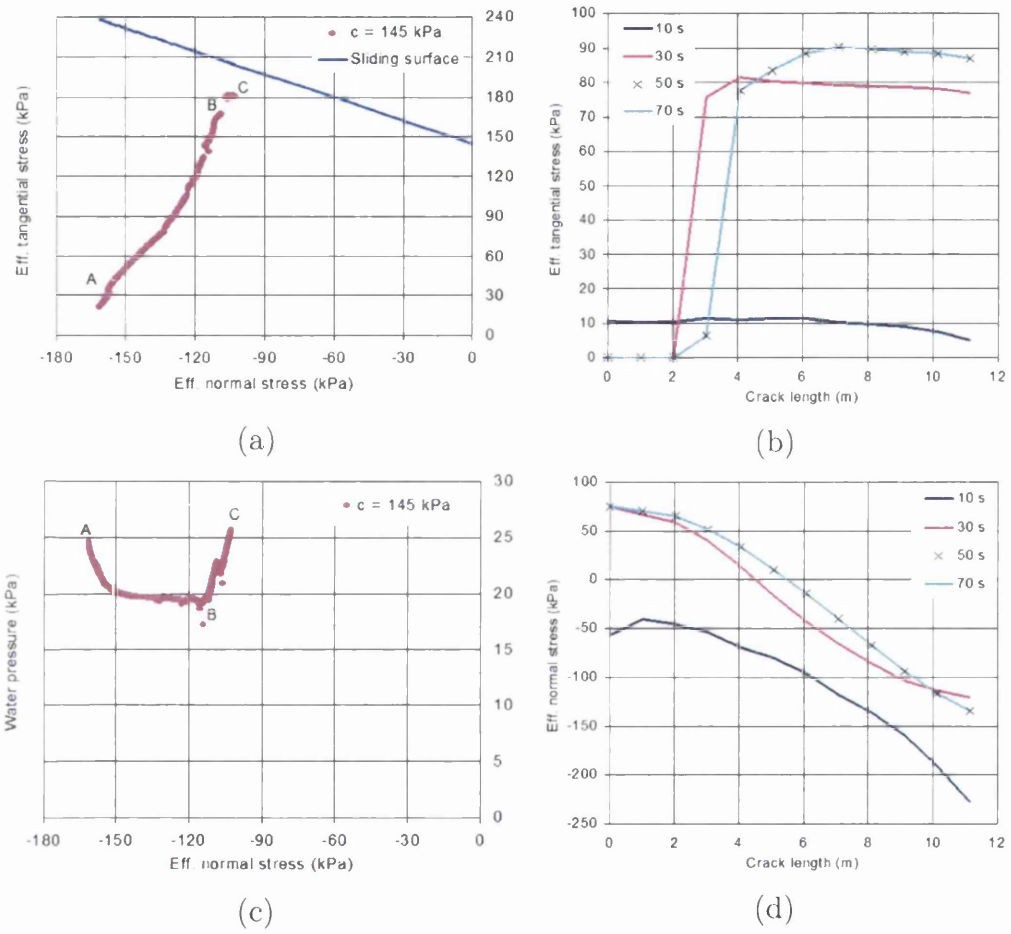

Figure 6.25: Shear strength characteristics and water pressure distribution for $c = 145$ kPa: (a) Effective tangential stress vs effective normal stress at node 56 during 70 s of analysis time. (b) Effective tangential stress distribution along the failure surface. (c) Water pressure as a function of the effective normal stress at node 56 during 70 s of analysis time. (d) Effective normal stress distribution along the failure surface.

6.3.3 Stability of a fractured slope after excavation process.

One of the major difficulties in excavation process is to predict the failure of the slope formed. From the computational point of view, the numerical model must be capable of dealing with a series of non-linearities and discontinuities as discussed previously in Section 6.1. Therefore, it provides a real challenge to the current model proposed.

The following example comprises an approximation to a real excavation problem, since the excavated part of the soil is neglected and substituted by displacement restrictions which will be slowly released after an initial stress state is reached, allowing the sliding of the rockfall. The soil is considered fully saturated and an undefined boundary condition is assumed on the excavated part of the soil, allowing the outflow in that region, but not the inflow. The geometry and boundary conditions of the problem are shown in Figure 6.26. Three initial fractures are assumed in the soil mass. These are indicated by the red lines in Figure 6.26.

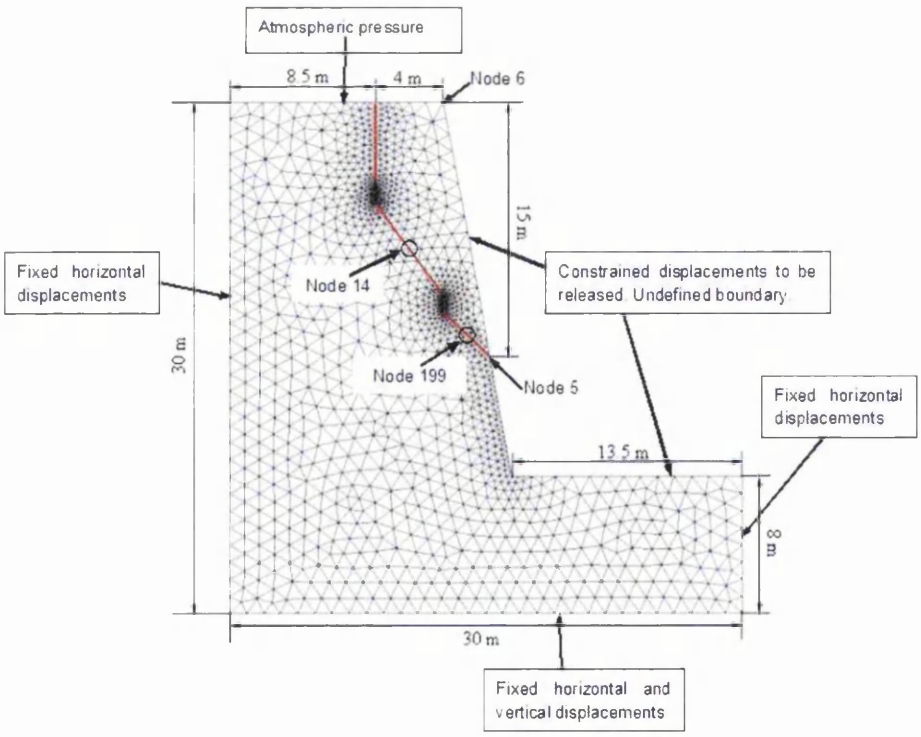

Figure 6.26: Layout of the problem.

A fully couple 2D plane strain analysis is used to solve the problem. The constitutive behaviour of the soil is represented by a Mohr-Coulomb rotating crack model proposed by Klerck (2000). And seepage and network flows are based on Darcy's and cubic laws respectively. The contact is based on a penalty formulation and friction sliding along joints is defined by the well known Coulomb's friction law. The material properties and contact data are given in Tables 6.6, 6.7 and 6.8.

The main goal is to demonstrate that a more accurate assessment of the slope failure in excavation problems can be made using the proposed model. In order to evaluate the model proposed, results will be compared against a more simple analysis (standard model), where, seepage or network flow are not considered.

Skeleton data	Value
Young's Modulus	1.0 GPa
Poisson ratio	0.24
Mass density of the skeleton	1700 Kg/m^3
Cohesion	26400 Pa
Friction angle	49°
Dilation angle	5°
Tensile strength	13000 Pa
Energy release	100 Pa.m
Contact data	Value
Normal penalty	1.0 GPa/m
Tangential penalty	0.1 GPa/m
Cohesion	10000 Pa
Friction angle	30°

Table 6.6: Skeleton properties and contact data.

Network flow data	Value
Normal stiffness of the fracture	5.0 GPa/m
Fluid compressibility	0.5 GPa^{-1}
Dynamic viscosity of the fluid	0.001 Pa.s
Residual aperture	0.03 mm
Initial aperture tensile crack	0.3 mm
Initial aperture failure surface	0.03 mm
Fluid mass density	1000 Kg/m^3
Gravitational acceleration	9.81 m/s^2

Table 6.7: Input data for the network flow problem.

Seepage flow data	Value
Intrinsic permeability	2.4670E-11 m^2
Grain bulk modulus	3.11 GPa
Fluid bulk modulus	2 GPa
Fluid mass density	1000 Kg/m^3
Grain mass density	1875 Kg/m^3
Dynamic viscosity of the fluid	0.001 Pa.s
Porosity	0.2
Saturation	1.0
Biot's number	1.0

Table 6.8: Input data for the seepage flow problem.

In the beginning (1 second), an initial geostatic condition is obtained, considering the soil mass intact. At this stage pore pressure distribution is represented in Figure 6.27.

Then, an excavation process occurs, causing the pore pressure in the daylight surface to drop to an atmospheric pressure value, as shown in Figure 6.28. At this point the displacement are still being slowly released. When the elapsed time reaches 3 seconds, the slope is completely free to slide.

At 15 seconds, higher plastic deformations are noted in rock bridges zones as shown in Figure 6.32. The rock bridges seems to be very close to a failure point, since that failure factor value is almost 1.0. At this stage, pore pressure have decreased in the soil mass as seen in Figure 6.30.

Finally, after 20 seconds material failure near the rock bridges occurs and the slope starts to slide down, as can be seen in Figure 6.32.

A comparison of the vertical displacements in Figure 6.33 shows that in a standard dry analysis where seepage or network flow are not considered, failure does not occur. However, the analysis carried out using the numerical model proposed have demonstrated that failure is expected, since pressures in the joints and in the soil decreases effective normal stress, and consequently effective tangential stress, reducing friction forces, as shown in Figure 6.31. Therefore, facilitating the failure of the rock bridges and sliding of the rock mass.

The numerical model proposed has shown to be a powerful tool in the assessment of slope stability problems, often seen in excavation processes. It provides useful data that can help analyst to have a better understanding of the failure mechanism involved in the process, since a more complex analysis which accounts for the constitutive behaviour of the soil, seepage and network flows is taken into consideration.

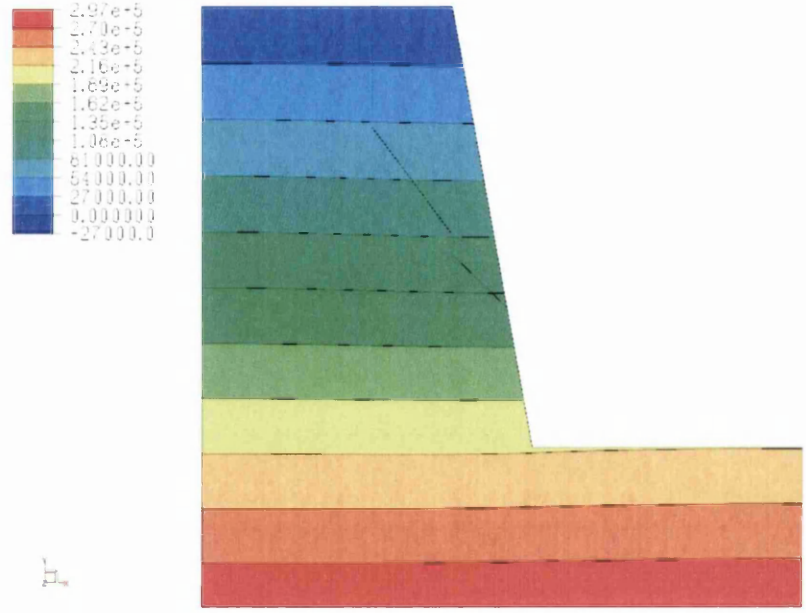

Figure 6.27: Initial pore pressure in the soil before excavation.

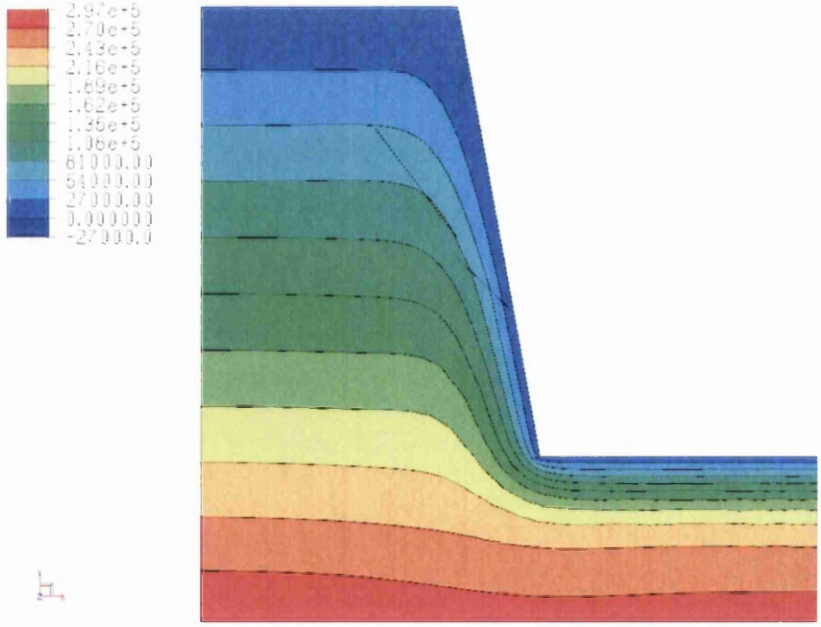

Figure 6.28: Initial pore pressure in the soil after excavation.

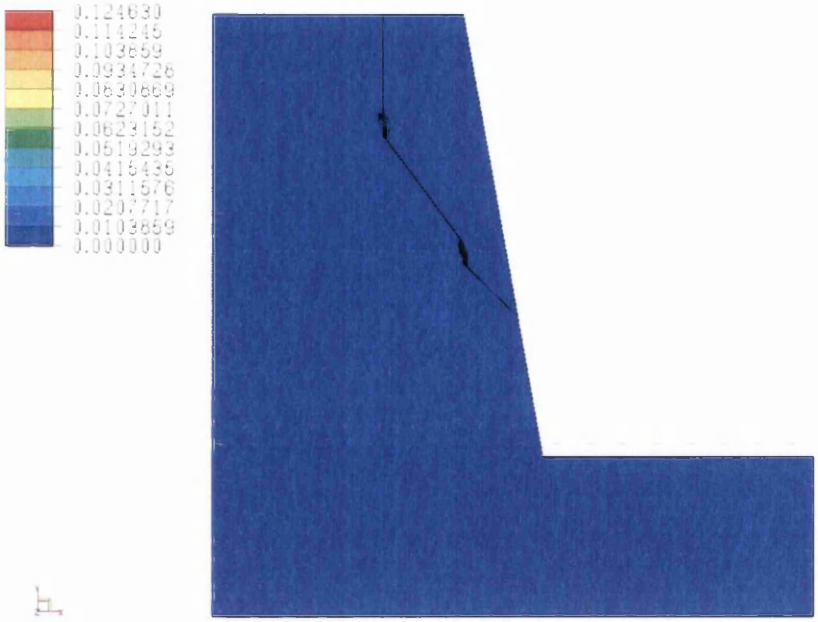

Figure 6.29: Effective plastic deformations in the rock bridges at 15 seconds.

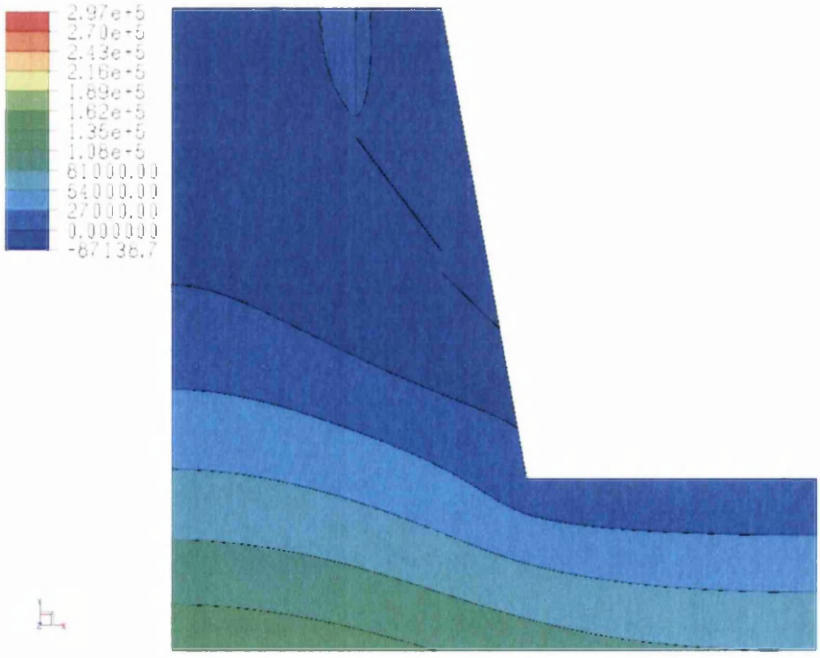

Figure 6.30: Pore pressure distribution after 15 seconds of elapsed time.

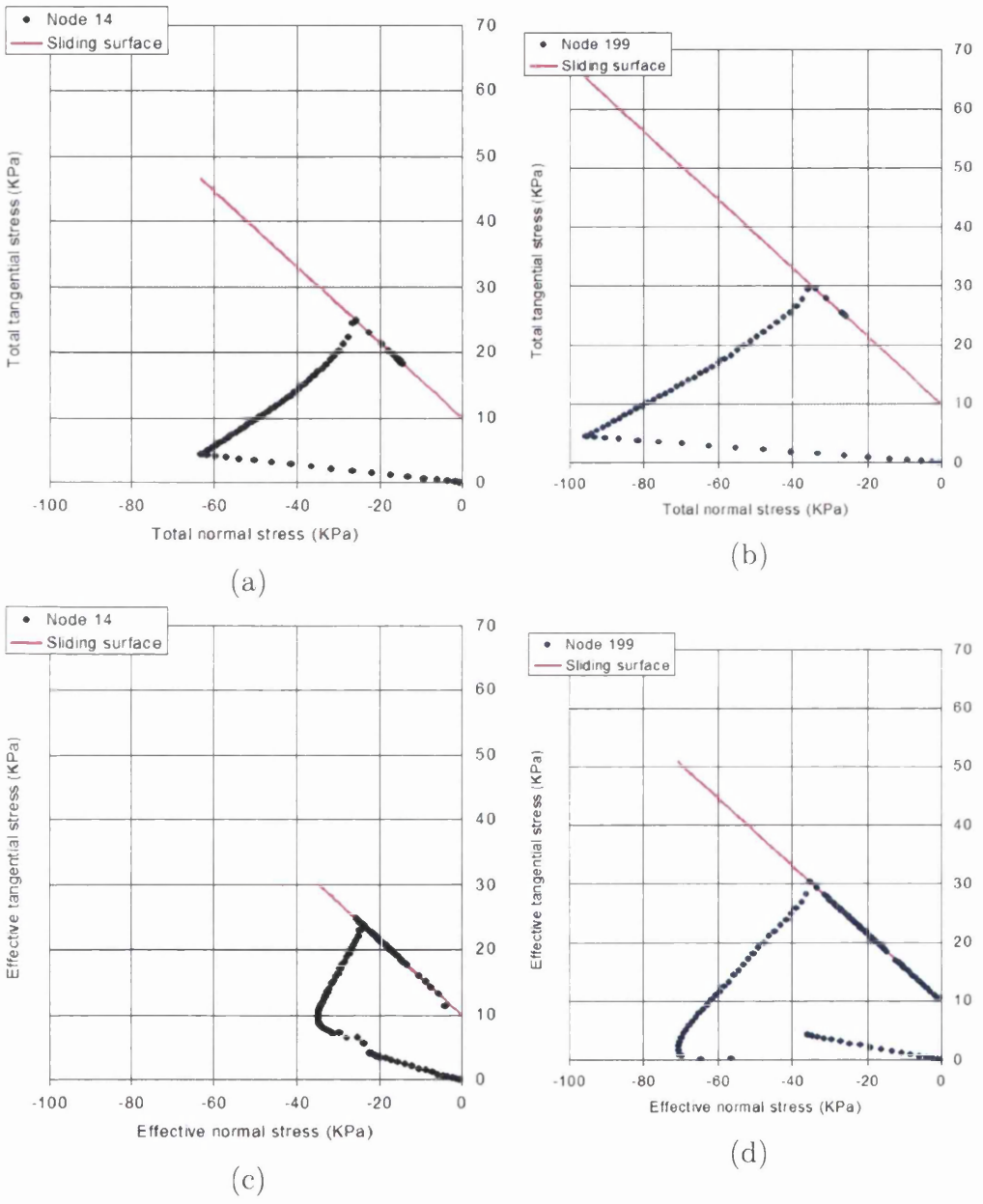

Figure 6.31: Shear strength characteristics during 20 seconds of elapsed time: (a) Total tangential stress vs Total normal stress at node 14. (b) Total tangential stress vs Total normal stress at node 199. (c) Effective tangential stress vs effective normal stress at node 14. (d) Effective tangential stress vs effective normal stress at node 199.

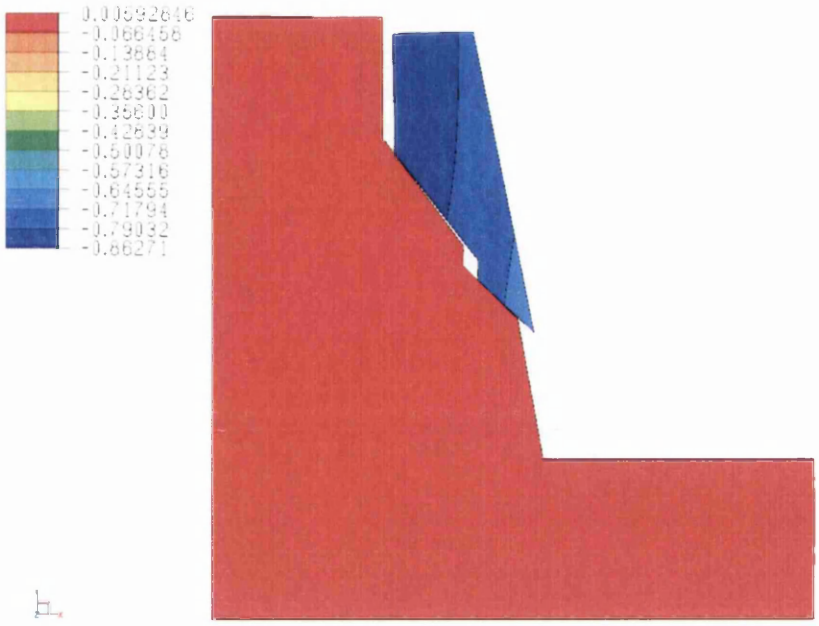

Figure 6.32: Vertical displacements showing that failure has occurred.

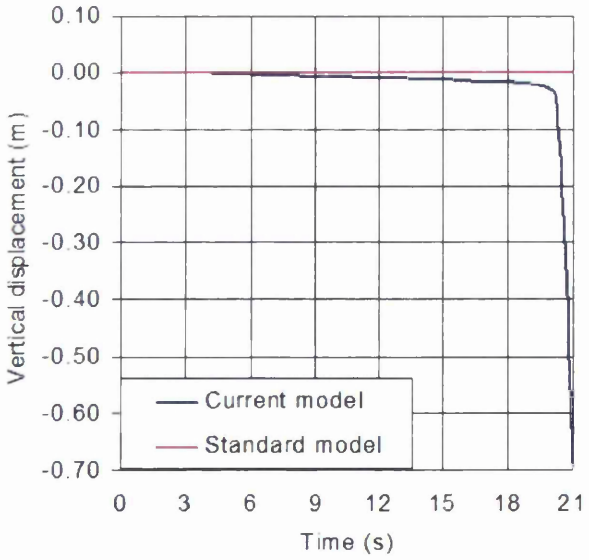

Figure 6.33: Vertical displacements showing that failure has occurred.

Chapter 7

Conclusions and Final Remarks

In this thesis, a series of developments have been proposed in order to tackle some of the limitations presented by current numerical models for oil production and slope stability analysis. The main tasks included the implementation and validation of soil-pore fluid interaction analysis, a procedure to stabilize spurious singular modes in seepage quadrilateral and hexahedral elements, development of a computational model for analysis of coupled hydro-fracture flow in porous media, verification of the influence of the plastic zones in a fractured porous medium and assessment of factor of safety for slope stability.

7.1 Conclusions

Significants progress has been made in the main topics addressed and an efficient numerical tool capable of dealing with the related problems has been developed. Special attention has been given to the development of new techniques to reduce the computational cost of coupled hydro-fracture flow in porous media based on explicit finite element procedures. Namely, a master-slave approach to link seepage and network flows and an explicit-explicit subcycling scheme have been introduced. Also, the application of the numerical model to the investigation of the influence of the plastic zones in a fractured porous medium and assessment of factor of safety for slope stability problems has been undertaken.

A more detailed list of the achievements and conclusions of the thesis are described in the following.

7.1.1 Soil-pore fluid interaction analysis

One of the first tasks necessary to achieve an efficient numerical model capable of dealing with problems that the present work is particularly directed at, has been to couple skeleton deformation and flow into the porous material. This is crucial to provide a correct evaluation of in situ stress fields, since, pressure dependent yield criteria used to model the constitutive behaviour of soils and rocks are based on effective stresses, which are highly affected by alterations in pore pressure.

The implementation has been based on a set of equations proposed and discussed in details by several authors, such as, Zienkiewicz et al. (2001) and Lewis and Schrefler (1998). However, in the literature review undertaken by the author, the *u-p* formulation adopted in the present work has never been employed using an explicit time integration scheme as proposed here. The main reasons for rejecting this time integration scheme are related to its conditional stability and high computational cost. The main reason for the adoption of an explicit integration scheme has been the fact that in large industrial problems the computational effort necessitated by implicit methods are prohibitive. Furthermore, in problems involving crack initiation and propagation, and complex contact situations, the lack of convergence of implicit methods is a well known major shortcoming. In such cases, the choice of an explicit method has shown to be particularly attractive.

As shown throughout the examples provided in this thesis, a robust numerical implementation has been achieved for 2-D and 3-D cases.

7.1.2 Stabilization of spurious singular modes

One of the main advantages of explicit methods is the use of one point quadrature elements because substantial reductions are achieved in the number of evaluations of the semi-discretized gradient operator and constitutive equations. However, mesh instabilities are well known to occur due to this reduced integration scheme.

To overcome this problem in the present work a stabilization procedure proposed by Liu and Belytschko (1984) and Belytschko et al. (1984) has been adopted. The stabilization technique has been previously applied by the authors cited above in the solution of thermal problems. Its use in seepage problems has been addressed by the present thesis for the first time. The patch test problem solved has shown that spurious zero-energy modes have been eliminated by a rank sufficient matrix formed by an element conductivity matrix using a one-point quadrature and a stabilization matrix, proving to be an efficient and accurate solution procedure, as shown mainly in Section

3.9.

7.1.3 Coupled hydro-fracture flow in porous media

The strategy used to simulate hydro-fracture flow in porous media is based on a staggered solution scheme employing a Finite/Discrete Element Method. The major contributions presented here are the development and validation of a master-slave procedure to link seepage and network flows and an explicit-explicit subcycling scheme, both discussed in Chapter 4.

The use of the master-slave technique has been shown to be particularly attractive in large scale calculations where significant decrease in computational costs can be achieved. In 2-D cases, the number of variables to be solved are reduced from four or six, necessary by double noded and triple noded formulations respectively, to only two. This reduction is even more significant in 3-D analysis, where only three or four variables, in tetrahedral and hexahedral elements respectively, are necessary to be solved by the proposed method. On th other hand six or nine in tetrahedral elements and nine or twelve in hexahedral elements are required to be solved by the other two formulations cited above. Also, it has been shown by means of a dynamic filtration example that mass conservation is preserved. The limitation is related to problems where a potential drop between network pressure and pore pressure occurs.

Large aperture increases have been shown to reduce significantly the time steps, as a result of the quadratic increase of the intrinsic permeability and a decrease in the fracture storativity. In order to overcome this problem an explicit-explicit subcycling scheme has been proposed. This has provided a 84% savings in CPU times for the 2-D case evaluated in comparison with standard methods, showing the procedure to be very efficient.

7.1.4 Plastic zones in a fractured porous medium

Plastic deformations and leak-off effects are the main factors responsible for the determintion of aperture, length and network pressure in the fractures, and pore pressure in the rock. The analyses carried out in this thesis have investigated these effects for different permeabilities of the rock, first, in a small scale problem and then, in a large scale case.

For the small scale problems, highly permeable poroelato-plastic rocks have resulted a shorter length and wider opening. Also, the vertical stresses show a more uniform distribution near the wellbore region and a steeper gradient near the crack tip. These are a consequence of its higher diffusion, which affects the effective stresses in far field regions causing a more

widespread development of inelastic deformations.

In the large scale case, two distinctive behaviours related to the aperture sizes have been noted. Impermeable rock have exhibited a wider opening near the wellbore and slightly smaller near the crack tip when compared against a permeable rock with intrinsic permeability of 50 mD. However, for $k = 200$ mD, the aperture has been wider throughout the entirely fracture length.

In the first case, the extra-stiffness induced by the increase in pore pressure is predominant in comparison to the inelastic deformations in the region near the wellbore. On the other hand, in the second case, inelastic deformations have overcome pore pressure effects, causing an increase in the aperture along the fracture.

Rocks of higher permeability have presented a large fluid lag region ahead of the crack tip, which results in higher pressure gradients. Consequently, they require a higher fluid pressure to open the fracture, leading to a higher shearing of the rock.

7.1.5 Factor of safety for slope stability

In the present work, the factor of safety obtained by limit equilibrium theory in plane slope failures has been compared to results produced by the numerical model proposed in Chapter 6. Both the rockfall and main slope are considered as impermeable rocks, and frictional sliding is controlled by a Coulomb friction law. First, cohesion in the interface has not been considered. Then, in a second case, cohesion between the rock and main slope has been taken into account.

In the first case, the effective normal stresses have disappeared in the begining of the failure surface. Consequently, a redistribution of the friction forces along the failure surface is obtained. The main reason for this is the fact that contact between main slope and failure surface has been lost. This phenomenon is attributed to lateral and uplift forces applied in the rockfall. A good agreement has been observed between the factor of safety (FOS) obtained by limit equilibrium theory and results obtained by the numerical model. For $FOS > 1$, no sliding of the rockfall have been seen. However, for $FOS = 1$, which is an unstable condition failure has occurred.

In the second case, an increase in the friction force has been noted for higher cohesion coefficient, consequently, reducing the sliding of the rockfall as expected. Also, results have shown that water pressure distributions are affected during the sliding process, causing variations in the effective normal stresses, consequently altering the friction forces. Some differences have been observed between failures occurring in the examples and factor of safety

predicted by limit equilibrium theory. Failures have occurred for *FOS* of 1.0, 1.2 and 1.3, which was not expected. The main reasons are attributed to:

1. Water pressure distribution in the failure surface is not considered to suffer any disturbance during the sliding of the block in the limit equilibrium theory. However, numerical results presented in Figures 6.19, items (c) and (d), have shown higher values at the failure surface, which leads to a reduction in the resisting force. A higher hydraulic column in the tensile crack is seen as a result of the sliding of the block. Consequently, a higher gradient of the fluid pressure occurs at the failure surface.

2. Deformations occurring in the rockfall along the failure surface during the sliding process which affect the effective normal stress distribution, and consequently, the resisting forces, as illustrated in Figures 6.22 and 6.23, items (b) and (d).

3. Numerical instabilities caused by limitations in the formulation used. The velocity of the sliding process has been shown to be crucial for the stability of the network flow analysis. The formulation used is acceptable to fluid flows occurring at low velocities only.

Despite its limitations the proposed framework was shown to be of particular interest from the practical point of view. The results have shown that a factor of safety of 1.3 should only be used in situations where the stability of the slopes are not required to be guaranteed for a long period of time, while, FOS = 1.5 can be used for critical slopes. These values are normally applied in practical situations.

7.2 Suggestion for future research

Results presented in previous chapters have shown that considerable advances have been achieved in this thesis. The simulation of coupled hydro-fracture flow in porous media has proved to be a powerful tool to deal with oil production and slope stability analysis. However, further developments are needed to improve the computational model. A list of possible aspects related to the topics presented in this thesis that could contribute to the continuity of this research are described below:

- Seepage field - Oil extraction is a multi-phase system where a mixture of injected fluid, crude oil and gases are present. Therefore, the incorporation of a formulation that includes various fluid phases into the

existing computational model will provide a better understanding of the overall process.

- Network field - Development of formulations capable of dealing with flow at higher velocities and mixtures of fluid injected, crude oil and gases, will improve the numerical model. Also, modifications in the implementation can be made in order to allow large rotations and movements as normally occur in slope stability problems. Finally, implementation of a triple-noded element should be interesting to account for problems where potential drops are important.

- Mechanical field - Implementation of an effective adaptivity/remeshing technique to provide a more accurate analysis of the crack initiation and propagation.

- Thermal field - the heat exchange between fluid injected, gases, oil and porous rock causes a variation in the material properties of the fluids and rock, such as mass density, viscosity, strength among others, influencing the overall analysis.

- Mass Transport field - Non-natural fluids injected into fractures include in their composition solid particles which are deposited along the crack walls in order to avoid closure. These creates a "*shield*" around the fracture reducing the flow into the rock mass and increasing the pressure in the fracture.

Bibliography

1377, B. S., 1991. Methods for test of soils for civil engineering purposes. Tech. rep., British Standards Institution.

5930, B. S., 1981. Code of practice for site investigations. Tech. rep., British Standards Institution.

Atkinson, B. K., 1987. Fracture mechanics of rock. Academic Press Limited.

Bear, J., 1979. Hydraulics of groundwater. McGraw-Hill Inc.

Belytschko, T., Liu, W. K., Moran, B., 2000. Nonlinear finite elements for continua and structures. John Wiley & Sons.

Belytschko, T., Mullen, R., 1978. Stability of explicit-implicit time mesh partitions in time integration. International Journal of Numerical Methods. 12, 1575–1586.

Belytschko, T., Ong, J. S.-J., Liu, W. K., Kennedy, J. M., 1984. Hourglass control in linear and nonlinear problems. Computer Methods in Applied Mechanics and Engineering. 43, 251–276.

Biot, M. A., 1941. General theory of three-dimensional consolidation. J. Appl. Phys. 12, 155–164.

Biot, M. A., 1955. Theory of elasticity and consolidation for a porous anisotropic solid. J. Appl. Phys. 26, 182–185.

Biot, M. A., 1956a. Theory of propagation of elastic waves in a fluid-saturated porous solid. part i - low frequency range. J. Acoust. Soc. Am. 28 (2), 168–178.

Biot, M. A., 1956b. Theory of propagation of elastic waves in a fluid-saturated porous solid. part ii - higher frequency range. J. Acoust. Soc. Am. 28 (2), 179–191.

Biot, M. A., 1962. Mechanics of deformation and acoustic propagation in porous media. J. Appl. Phys. 33 (4), 1482–1498.

Bishop, A. W., 1955. The use of the slip circle in the stability analysis of slopes. Géotechnique. 5 (1), 7–17.

Bjerrum, L., 1967. Progressive failure in slopes of overconsolidated plastic clay and clay shales. Journal Soil Mech. Foundat. Div ASCE, 93 (SM5), 1–49.

Blake, W., 1967. Stress and displacement surrounding an open pit in a gravity loaded rock. Tech. rep., U. S. Bureau of Mines Report of Investigations 7002,, United States.

Blake, W., 1969. Finite element model is excellent pit tool. Mining Engineering, A.I.M.E., 21 (8), 79–80.

Boone, T. J., Ingraffea, A. R., 1990. A numerical procedure for simulation of hydraulically-driven fracture propagation in poroelastic media. International Journal for Numerical and Analytical Methods in Geomechanics. 14, 27–47.

Boone, T. J., Ingraffea, A. R., Roegiers, J. C., 1991. Simulation of a hydraulic fracture propagation in poroelastic rock with application to stress measurement techniques. Intenational Journal of Rock Mech. Min. Sci. & Geomech. 28 (1), 1–14.

Carman, P. C., 1937. Fluid flow through granular bed. Trans. Instn. Chem. Engrs. (London) 15, 150–156.

Cho, S. E., Lee, S. R., 2001. Instability of unsaturated soil slopes due to infiltration. Computers and Geotechnics. 28, 185–208.

Cleary, M. P., Wright, C. A., Wright, T. B., 1991. Experimental and modeling evidence for major changes in hydraulic fracturing design and field procedures. In: Proceedings SPE Gas Technology Symposium. Houston, pp. 131–146.

Das, B. M., 1985. Principles of geotechnical engineering. PWS Publishers.

de Souza Neto, E. A., Peric, D., Owen, D. R. J., 2002. Computational plasticity - small and large strain finite element analysis of elastic and inelastic solids., non-linear computational mechanic course - USP.

Desroches, J., Detournay, E., Lenoach, B., Papanastasiou, P., Pearson, J., Thiercelin, M., Cheng, A., 1994. The crack tip region in hydraulic fracturing. Proceedings of Royal Society of London. , 39–48.

Detournay, E., Cheng, A. H. D., 1991. Plane strain analysis of a stationary hydraulic fracture in a poroelastic medium. Intenational Journal of Solids and Structures. 37, 1645–1662.

Detournay, E., Cheng, A. H. D., Mclennan, J. D., 1990. A poroelastic pkn hydraulic fracture model based on an explicit moving mesh algorithm. J. Energy Res. Tech., ASME, in print .

Duncan, J. M., 1996. State of the art: limit equilibrium and finite elemenent analysis of slopes. Journal Geotech. Engng., ASCE, 122 (7), 577–596.

Eberhardt, E., Stead, D., Coggan, J. S., 2004. Numerical analysis of initiation and progressive failure in natural rock slopes - the 1991 randa rockslide. International Journal of Rock Mechanics & Minning Sciences. 41, 69–87.

Ehlers, W., Graf, T., Ammann, M., 2004. Deformation and localization analysis of partially saturated soil. Comput. Methods Appl. Mech. Engrg. 193, 2885–2910.

Elfen, 2005. ELFEN 2D/3D numerical modelling package. Rockfield Software Ltd., Swansea, version 3.3.45 Edition.

Endo, H. K., Long, J. C. S., Wilson, C. R., Witherspoon, P. A., 1984. A model for investigating mechanical transport in fracture networks. Water Resources Research. 20 (10), 1390–1400.

Fellenius, W., 1936. Calculation of the slope stability of earth dams. In: Proc. 2^{nd} congr. large dams. Vol. 4. Washington D.C.

Geerstma, J., de Klerk, F., 1969. A rapid method of the theories for predicting width and extent of hydraulic induced fractures. J. Petrol. Tech. 246, 1571–1581, sPE 2458.

Griffiths, D. V., Lane, P. A., 1999. Slope stability analysis by finite elements. Géotechnique. 49 (3), 387–403.

Guiducci, C., Pellegrino, A., Radu, J. P., Collin, F., Charlier, R., 2002. Numerical modeling of hydro-mechanical fracture behavior. In: Numerical Models in Geomechanics NUMOG VII. G. N. Pande, S. Pietruszczak., Swets & Zeitlinger : Lisse, pp. 293–299.

Hazen, A., 1930. Watter supply. In: American Civil Engineers Handbook. John Wiley & Sons., New York.

Hoek, E., Bray, J., 1977. Rock slope engineering., revised second edition Edition. Institution of Mining and Metallurgy., London.

Hubbert, M. K., Willis, D. G., 1957. Have to find the reference yet. Journal of Petroleum Technology, Trans. AIME 210, 153–168.

Hughes, T. J. R., Liu, W. K., 1978a. Implicit-explicit finite elements in transient analysis: Implementation and numerical examples. J. Appl. Mech. 45, 375–378.

Hughes, T. J. R., Liu, W. K., 1978b. Implicit-explicit finite elements in transient analysis: Stability theory. J. Appl. Mech. 45, 371–374.

Hyne, N. J., 2001. Nontechnical guide to petroleum geology, exploration, drilling and production. Penn Well Corporation.

Iwai, K., 1976a. Fluid flow in simulated fractures. Am. Inst. Chem. Eng. J., 2, 259–263.

Iwai, K., 1976b. Fundamental studies of fluid flow through a single fracture. Ph.D. thesis, University of California, Berkeley.

Janbu, N., 1968. Slope stability computations. Tech. rep., Soil Mech. Found. Engng., Report,, Trondheim : Technical University of Norway,.

Jing, L., Ma, Y., Fang, Z., 2001. Modeling of fluid flow and solid deformation for fractured rocks with discontinuous deformation analysis (dda) method. International Journal of Rock Mechanics & Mining Sciences. 38, 343–355.

Khristianovic, S., Zheltov, Y., 1955. Formation of vertical fractures by means of highly viscous fluids. In: Proc. 4^{th} World Petroleum Congress. Vol. 2. Rome., pp. 579–586.

Kim, Y.-I., Amadei, B., Pan, E., 1999. Modeling the effect of water , excavation sequence and rock reinforcement with discontinuous deformation analysis. International Journal of Rock Mechanics and Mining Sciences. 36, 949–970.

Kirsch, G., 1898. Z. verein deutscher ing. VDI 42, 113.

Klerck, P. A., 2000. The finite element modelling of discrete fracture in quasi-brittle materials. Ph.D. thesis, University of Wales Swansea.

Lewis, R. W., Schrefler, B. A., 1998. The finite element method in the static and dynamic deformation and consolidation of porous media. John Wiley & Sons.

Li, Y., LeBoeuf, E. J., Basu, P. K., Mahadevan, S., 2005. Stochastic modeling of the permeability of randomly generated porous media. Advances in Water Resources. 28, 835–844.

Liu, W. K., Belytschko, T., 1984. Efficient linear and nonlinear heat conduction with a quadrilateral element. International Journal for Numerical Methods in Engineering. 20, 931–948.

Lowe, J., Karafiath, L., 1960. Stability of earth dams upon drawdown. In: Proc. 1^{st} Pan-Am Conf. Soil Mech. Found. Engng. pp. 537–552.

Mizukami, A., 1986. Variable explicit finite element methods for unsteady heat conduction equations. Computer Methods in Applied Mechanics and Engineering. 59, 101–109.

Moench, A. F., 1984. Double-porosity models for a fissured groundwater reservoir with fracture skin. Water Resources Research. 20 (7), 831–846.

Morgenstern, N. R., Price, V. E., 1965. The analysis of the stability of general slip surfaces. Géotechnique. 15 (1), 79–93.

Muller, L., 1959. The european approach to slope stability problems in open pit mines. In: Proc. 3^{rd} Symposium on Rock Mechanics. Vol. 54. Colorado School of Mines Quartely., pp. 116–133.

Neal, M. O., Belytschko, T., 1989. Explicit-explicit subcycling with non-integer time step ratios for structural dynamic systems. Computers & Structures. 31, 871–880.

Ng, C. W. W., Shi, Q., 1998. A numerical investigation of the stability of unsaturated soil slopes subjected to transient seepage. Computers and Geotechnics 22 (1), 1–28.

Ng, K. L. A., Small, J. C., 1997. Behavior of joints interfaces subjected to water pressure. Computers and Geotechnics. 20 (1), 71–93.

Nordgren, R. P., 1972. Propagation of a vertical hydraulic fracture. Society of Petroleum Engineering Journal, Trans. AIME 253, 306–314.

Nutting, P. G., 1930. Physical analysis of oil sands. Bull. Am. Ass. petrol. Geol. 14, 1337–1349.

Owen, D. R. J., Hinton, E., 1980. Finite elements in plasticity: Theory and Practice. Pineridge Press.

Papanastasiou, P., 1997a. A coupled elastoplastic hydraulic fracturing model. International Journal of Rock Mechanics and Mining Sciences. 34 (3-4), paper No. 240.

Papanastasiou, P., 1997b. The influence of plasticity in hydraulic fracturing. International Journal of Fracture. 84, 61–97.

Papanastasiou, P., 1999a. The effective fracture toughness in hydraulic fracturing. International Journal of Fracture. 96, 127–147.

Papanastasiou, P., 1999b. An efficient algorithm for propagating fluid-driven fractures. Computational Mechanics. 24, 258–267.

Papanastasiou, P., 1999c. Formation stability after hydraulic fracturing. International Journal for Numerical and Analytical Methods in Geomechanics. 23, 1927–1944.

Papanastasiou, P., 2000. Hydraulic fracture closure in a pressure-sensitive elastoplastic medium. International Journal of Fracture. 103, 149–161.

Papanastasiou, P., Thiercelin, M., 1993. Influence of inelastic rock behaviour in hydraulic fracturing. International Journal of Rock Mechanics and Mining Sciences and Geomechanics. 30 (7), 1241–1247.

Perkins, T. K., Kern, L. R., 1961. Widths of hydraulic fractures. Journal of Petroleum Technology, Trans. AIME 22, 937–949.

Pruess, K., Wang, J. S. Y., Tsang, Y. W., 1990. On thermohydrologic conditions near high-level nuclear wastes emplaced in partially saturated fractured tuff. 2. effective continuum approximation. Water Resources Research 26 (6), 1249–1261.

Ruina, A., 1978. Influence of coupled deformation-diffusion effects on the retardation of hydraulic fracture. In: Proceedings of the 19^{th} US Symposium on Rock Mechanics. pp. 274–282.

Savitski, A. A., Detournay, E., 2002. Propagation of a penny-shaped fluid-driven fracture in an impermeable rock: asymptotic solutions. International Journal of Solids and Structures. 39, 6311–6337.

Segura, J. M., Carol, I., 2004. On zero-thickness interface elements for diffusion problems. International Journal for Numerical and Anlytical Methods in Geomechanics. 28, 947–962.

Segura, J. M., Carol, I., 2005. Fluid driven fracture analysis with zero-thickness interface elements. In: Proceedings of the VIII International Conference on Computational Plasticity. International Center for Numerical Methods in Engineering (CIMNE)., Barcelona.

Shlyapobersky, J., 1985. Energy analysis of hydraulic fracturing. In: Proceedings of the 26^{th} US Symposium on Rock Mechanics. Rapid City, pp. 539–546.

Slide, 2002. Groundwater module in Slide. Verification manual. Rocscience Inc., version 2.2 Edition.

Smith, L., Schwartz, F. W., 1984. An analysis of the influence of fracture geometry on mass transport in fractured media. Water Resources Research. 20, 1241–1252.

Sneddon, I. N., 1946. The distribution of stress in the neighborhood of a crack in an elastic solid . In: Proc. R. Soc. London. Vol. A187. pp. 229–260.

Spencer, E., 1967. A method of analysis of the stability of embankments assuming parallel interslice forces. Géotechnique. 17 (1), 11–26.

Stacey, T. R., 1971. The stress surrounding open-pit mine slopes. In: Planning open pit mines, Johannesburg Symposium,. A. A. Balkema,, Amsterdam, pp. 199–207.

Sudicky, E. A., McLaren, R. G., 1992. The laplace transform galerkin technique for large-scale simulation of mass transport in discretely fractured porous formation. Water Resources Research. 28 (2), 499–514.

Turcke, M., Kueper, B., 1996. Geostatisticcal analysis of the borden aquifer hydraulic condutivity. Journal of Hydrology, 178, 223–240.

van Dam, D. B., de Pater, C. J., Romijn, R., 1997. Experimental study of the impact of plastic rock deformation on hydraulic fracture geometry. International Journal of Rock Mechanics and Mining Sciences. 34 (3-4), paper No. 240.

von Terzaghi, K., 1936. The shearing resistance of saturated soils. In: Proc. 1^{st} ICSMFE. Vol. 1. pp. 54–56.

von Terzaghi, K., Redulic, L., 1934. Die wirksame flächenporosität des betons. Z. Öst. Ing -u. ArchitVer 86, 1–9.

Wang, F. D., Sun, M. C., 1970. Slope stability analysis and limiting equilibrium method. Tech. rep., U. S. Bureau of Mines Report of Investigations 7341, United States.

Woodbury, A., Zhang, K., 2001. Lanczos method for the solution of groundwater flow in discretely fractured porous media. Advances in Water Resources. 24, 621–630.

Yu, Y. S., Gyenge, M., Coates, D. F., 1968. Comparison of stress and displacement inn a gravity loaded slope by photoelasticity and finite element analysis. Tech. rep., Canadian Dept. Energy, Mines and Resources Report MR 68-24 ID,.

Zhao, C., Hobbs, B. E., Ord, A., Robert, P. A., Hornby, P., Peng, S., 2007. Phenomenological modelling of crack generation in brittle crustal rocks using the particle simulation method. Journal of Structural Geology. 29, 1034–1048.

Zienkiewicz, O. C., Chan, A. H. C., Pastor, M., Schrefler, B. A., Shiomi, T., 2001. Computational Geomechanics with special reference to Earthquake Engineering. John Wiley & Sons.

Zienkiewicz, O. C., Chang, C. T., Bettess, P., 1980. Drained, undrained, consolidating and dynamic behaviour assumptions in soils. limits of validity. Geotechnique. 30, 385–395.

Zienkiewicz, O. C., Taylor, R. L., 2000. The Finite Element Method - Vol. 1: The Basis, and Vol. 2: Solid Mechanics., 5th Edition. Butterworth-Heinemann.

Appendix A

Hourglass control in 3D seepage elements.

Hourglass modes are a result of reduced integration techniques used in finite differences schemes to increase their performance. A mesh stabilization technique for eliminating spurious singular modes proposed by Belytschko et al. (1984) is applied in this work for hexahedral seepage elements in three dimensions.

The particular method consists in deriving a rank-sufficient matrix composed of a one-point-quadrature stiffness and stabilization matrix. A detailed description of their formulations is given below.

A.1 General form of rank sufficient matrix

In the present method the standard element, e, conductivity matrix , $\mathbf{K}_1^{(e)}$, is augmented by a stabilization matrix , $\mathbf{K}_{stab}^{(e)}$, to produce a rank sufficiency matrix:

$$\mathbf{K}^{(e)} = \mathbf{K}_1^{(e)} + \mathbf{K}_{stab}^{(e)} \tag{A.1}$$

In this formulation the pressure gradient, $\boldsymbol{\nabla} p$, is approximated by a Taylor series expansion by:

$$\begin{aligned}\boldsymbol{\nabla} p(\xi,\eta,\zeta) = \mathbf{B}_a(0)p_a + \mathbf{B}_{a,\xi}(0)p_a\ \xi + \mathbf{B}_{a,\eta}(0)p_a\ \eta + \mathbf{B}_{a,\zeta}(0)p_a\ \zeta + \\ 2\mathbf{B}_{a,\xi\eta}(0)p_a\ \xi\eta + 2\mathbf{B}_{a,\eta\zeta}(0)p_a\ \eta\zeta + 2\mathbf{B}_{a,\zeta\xi}(0)p_a\ \zeta\xi\ , \quad a = 1,\ldots,8\end{aligned} \tag{A.2}$$

where, ξ, η and ζ are the natural coordinates of the tri-unit cube and 0 denotes 'evaluated at (ξ, η, ζ) = (0,0,0)'; comma denotes partial differentiation in $\mathbf{B}_{a,(\cdot)}$; and $\mathbf{B}_a$ are the generalized gradient operators of the shape functions N_a given by:

$$\begin{aligned} \mathbf{B}_a &= \begin{bmatrix} N_{a,x} \\ N_{a,y} \\ N_{a,z} \end{bmatrix}; \\ N_a &= \frac{1}{8}(1+\xi_a)(1+\eta_a)(1+\zeta_a) \end{aligned} \tag{A.3}$$

The general form of the $\mathbf{K}_1^{(e)}$ and $\mathbf{K}_{stab}^{(e)}$ can be written as:

$$\begin{aligned} \mathbf{K}_1^{(e)} &= V\ \mathbf{B}_a^T(0)\ \frac{\mathbf{k}}{\mu}\ \mathbf{B}_b(0) \\ \mathbf{K}_{stab}^{(e)} &= \frac{1}{3}\ V\ \mathbf{B}_{a,\xi}^T(0)\ \frac{\mathbf{k}}{\mu}\ \mathbf{B}_{b,\xi}(0) + \frac{1}{3}\ V\ \mathbf{B}_{a,\eta}^T(0)\ \frac{\mathbf{k}}{\mu}\ \mathbf{B}_{b,\eta}(0) + \\ &\quad \frac{1}{3}\ V\ \mathbf{B}_{a,\zeta}^T(0)\ \frac{\mathbf{k}}{\mu}\ \mathbf{B}_{b,\zeta}(0) + \frac{4}{9}\ V\ \mathbf{B}_{a,\xi\eta}^T(0)\ \frac{\mathbf{k}}{\mu}\ \mathbf{B}_{b,\xi\eta}(0) + \\ &\quad \frac{4}{9}\ V\ \mathbf{B}_{a,\eta\zeta}^T(0)\ \frac{\mathbf{k}}{\mu}\ \mathbf{B}_{b,\eta\zeta}(0) + \frac{4}{9}\ V\ \mathbf{B}_{a,\zeta\xi}^T(0)\ \frac{\mathbf{k}}{\mu}\ \mathbf{B}_{b,\zeta\xi}(0) \end{aligned} \tag{A.4}$$

where, V is the volume of the element.

A.2 Explicit form of standard element conductivity matrix

In 3D, the computations of $\mathbf{K}_1^{(e)}$ requires the evaluation of the $\mathbf{B}_a(0)$ gradient submatrix. This can be obtained following the sequence described below.

Let us denote:

$$\begin{aligned} \boldsymbol{\xi} &= [-1,1,1,-1,-1,1,1,-1]^T; \\ \boldsymbol{\eta} &= [-1,-1,1,1,-1,-1,1,1]^T; \\ \boldsymbol{\zeta} &= [-1,-1,-1,-1,1,1,1,1]^T, \end{aligned} \tag{A.5}$$

where, $\boldsymbol{\xi_a}$, $\boldsymbol{\eta_a}$ and $\boldsymbol{\zeta_a}$ are the components of the a^{th} node of the tri-unit cube. Also, the x, y, z coordinates of the 8 node brick element can be described as

$$\begin{aligned} \mathbf{x} &= [x_1,x_2,x_3,x_4,x_5,x_6,x_7,x_8]^T; \\ \mathbf{y} &= [y_1,y_2,y_3,y_4,y_5,y_6,y_7,y_8]^T; \\ \mathbf{z} &= [z_1,z_2,z_3,z_4,z_5,z_6,z_7,z_8]^T. \end{aligned} \tag{A.6}$$

Then, a 3x3 Jacobian matrix, $J_8(\mathbf{0})$, can be shown to be:

$$J_8(\mathbf{0}) = \frac{1}{8}\begin{bmatrix} a_{11} & a_{12} & a_{13} \\ a_{21} & a_{22} & a_{23} \\ a_{31} & a_{32} & a_{33} \end{bmatrix} = \frac{1}{8}\begin{bmatrix} \xi^T\mathbf{x} & \xi^T\mathbf{y} & \xi^T\mathbf{z} \\ \eta^T\mathbf{x} & \eta^T\mathbf{y} & \eta^T\mathbf{z} \\ \zeta^T\mathbf{x} & \zeta^T\mathbf{y} & \zeta^T\mathbf{z} \end{bmatrix} \tag{A.7}$$

The 8x1 form of the gradients vectors, b_1, b_2, b_3 , which are evaluated at the centroid of the element in a reference configuration, are given by:

$$\begin{aligned} \mathbf{b}_1 = \{b_{1a}\} = \{N_{a,x}\} &= \frac{1}{64V}\left[C^1_{23}\,\boldsymbol{\xi} + C^1_{13}\,\boldsymbol{\eta} + C^1_{12}\,\boldsymbol{\zeta}\right] \\ \mathbf{b}_2 = \{b_{2a}\} = \{N_{a,y}\} &= \frac{1}{64V}\left[C^2_{23}\,\boldsymbol{\xi} + C^2_{13}\,\boldsymbol{\eta} + C^2_{12}\,\boldsymbol{\zeta}\right] \\ \mathbf{b}_3 = \{b_{3a}\} = \{N_{a,z}\} &= \frac{1}{64V}\left[C^3_{23}\,\boldsymbol{\xi} + C^3_{13}\,\boldsymbol{\eta} + C^3_{12}\,\boldsymbol{\zeta}\right] \end{aligned} \tag{A.8}$$

The nine coefficients, C^k_{ij}, are the determinants of the 2x2 partitioned submatrices of $J_8(\mathbf{0})$. They are explicitly derived as

$$\begin{aligned} C^1_{13} &= a_{32}a_{13} - a_{12}a_{33}, \\ C^1_{12} &= a_{12}a_{23} - a_{22}a_{13}, \\ C^2_{23} &= a_{31}a_{23} - a_{21}a_{33}, \\ C^2_{13} &= a_{11}a_{33} - a_{31}a_{13}, \\ C^2_{12} &= a_{21}a_{13} - a_{11}a_{23}, \\ C^3_{23} &= a_{21}a_{32} - a_{31}a_{22}, \\ C^3_{13} &= a_{31}a_{12} - a_{11}a_{32}, \\ C^3_{12} &= a_{11}a_{22} - a_{21}a_{12}. \end{aligned}$$

Then, the gradient submatrix, $\mathbf{B}_a(0)$, can be obtained using Equation A.3. Finally, the assembly of standard element conductivity matrix $\mathbf{K}^{(e)}_1$ can be made through Equation A.4.

The final task in the derivation of a rank sufficient matrix is to obtain the stabilization matrix. This will be show in the following Subsection.

A.3 Explicit form of stabilization matrix

The assembly of the stabilization matrix requires the evaluation of the derivatives of the gradient submatrices, $\mathbf{B}^T_{a,\xi}$, $\mathbf{B}^T_{a,\eta}$, $\mathbf{B}^T_{a,\zeta}$, $\mathbf{B}^T_{a,\xi\eta}$, $\mathbf{B}^T_{a,\eta\zeta}$, $\mathbf{B}^T_{a,\zeta\xi}$, with

respect to the reference configuration ξ, η, ζ, at the centroid of the element. Let us denote the hourglass vectors $\mathbf{h}_i$ and $\boldsymbol{\gamma}_i$, as

$$\begin{aligned} \mathbf{h}_1 &= [1,-1,1,-1,1,-1,1,-1]^T; \\ \mathbf{h}_2 &= [1,-1,-1,1,-1,1,1,-1]^T; \\ \mathbf{h}_3 &= [1,1,-1,-1,-1,-1,1,1]^T; \\ \mathbf{h}_4 &= [-1,1,-1,1,1,-1,1,-1]^T \end{aligned} \tag{A.9}$$

and

$$\begin{aligned} \boldsymbol{\gamma}_1 &= \mathbf{h}_1 - \left(\mathbf{h}_1^T\mathbf{x}\right)\mathbf{b1} - \left(\mathbf{h}_1^T\mathbf{y}\right)\mathbf{b2} - \left(\mathbf{h}_1^T\mathbf{z}\right)\mathbf{b3}; \\ \boldsymbol{\gamma}_2 &= \mathbf{h}_2 - \left(\mathbf{h}_2^T\mathbf{x}\right)\mathbf{b1} - \left(\mathbf{h}_2^T\mathbf{y}\right)\mathbf{b2} - \left(\mathbf{h}_2^T\mathbf{z}\right)\mathbf{b3}; \\ \boldsymbol{\gamma}_3 &= \mathbf{h}_3 - \left(\mathbf{h}_3^T\mathbf{x}\right)\mathbf{b1} - \left(\mathbf{h}_3^T\mathbf{y}\right)\mathbf{b2} - \left(\mathbf{h}_3^T\mathbf{z}\right)\mathbf{b3}; \\ \boldsymbol{\gamma}_4 &= \mathbf{h}_4 - \left(\mathbf{h}_4^T\mathbf{x}\right)\mathbf{b1} - \left(\mathbf{h}_4^T\mathbf{y}\right)\mathbf{b2} - \left(\mathbf{h}_4^T\mathbf{z}\right)\mathbf{b3}, \end{aligned} \tag{A.10}$$

where, $\mathbf{h}_1$ and $\boldsymbol{\gamma}_1$ are the $\xi\eta$-hourglass vectors; $\mathbf{h}_2$ and $\boldsymbol{\gamma}_2$ are the $\xi\zeta$-hourglass vectors; $\mathbf{h}_3$ and $\boldsymbol{\gamma}_3$ are the $\eta\zeta$-hourglass vectors; $\mathbf{h}_4$ and $\boldsymbol{\gamma}_4$ are the $\xi\eta\zeta$-hourglass vectors. Then after some algebra it can be shown that

$$\begin{aligned} \mathbf{b}_{1,\xi} &= \{N_{a,x\xi}\} = \frac{1}{64V}\left[C_{13}^1\,\boldsymbol{\gamma}_1 + C_{12}^1\,\boldsymbol{\gamma}_2\right], \\ \mathbf{b}_{2,\xi} &= \{N_{a,y\xi}\} = \frac{1}{64V}\left[C_{13}^2\,\boldsymbol{\gamma}_1 + C_{12}^2\,\boldsymbol{\gamma}_2\right], \\ \mathbf{b}_{3,\xi} &= \{N_{a,z\xi}\} = \frac{1}{64V}\left[C_{13}^3\,\boldsymbol{\gamma}_1 + C_{12}^3\,\boldsymbol{\gamma}_2\right], \\ \mathbf{b}_{1,\eta} &= \{N_{a,x\eta}\} = \frac{1}{64V}\left[C_{23}^1\,\boldsymbol{\gamma}_1 + C_{12}^1\,\boldsymbol{\gamma}_3\right], \\ \mathbf{b}_{2,\eta} &= \{N_{a,y\eta}\} = \frac{1}{64V}\left[C_{23}^2\,\boldsymbol{\gamma}_1 + C_{12}^2\,\boldsymbol{\gamma}_3\right], \\ \mathbf{b}_{3,\eta} &= \{N_{a,z\eta}\} = \frac{1}{64V}\left[C_{23}^3\,\boldsymbol{\gamma}_1 + C_{12}^3\,\boldsymbol{\gamma}_3\right], \\ \mathbf{b}_{1,\zeta} &= \{N_{a,x\zeta}\} = \frac{1}{64V}\left[C_{23}^1\,\boldsymbol{\gamma}_2 + C_{13}^1\,\boldsymbol{\gamma}_3\right], \\ \mathbf{b}_{2,\zeta} &= \{N_{a,y\zeta}\} = \frac{1}{64V}\left[C_{23}^2\,\boldsymbol{\gamma}_2 + C_{13}^2\,\boldsymbol{\gamma}_3\right], \\ \mathbf{b}_{3,\zeta} &= \{N_{a,z\zeta}\} = \frac{1}{64V}\left[C_{23}^3\,\boldsymbol{\gamma}_2 + C_{13}^3\,\boldsymbol{\gamma}_3\right], \end{aligned} \tag{A.11}$$

$$
\begin{aligned}
\mathbf{b}_{1,\xi\eta} &= \{N_{a,x\xi\eta}\} = \frac{1}{64V}\left[C^1_{12}\,\boldsymbol{\gamma}_4 - \left(\mathbf{p}_1^T\mathbf{x}_i\right)\mathbf{b}_{i,\xi} - \left(\mathbf{r}_1^T\mathbf{x}_i\right)\mathbf{b}_{i,\eta}\right], \\
\mathbf{b}_{2,\xi\eta} &= \{N_{a,y\xi\eta}\} = \frac{1}{64V}\left[C^2_{12}\,\boldsymbol{\gamma}_4 - \left(\mathbf{p}_2^T\mathbf{x}_i\right)\mathbf{b}_{i,\xi} - \left(\mathbf{r}_2^T\mathbf{x}_i\right)\mathbf{b}_{i,\eta}\right], \\
\mathbf{b}_{3,\xi\eta} &= \{N_{a,z\xi\eta}\} = \frac{1}{64V}\left[C^3_{12}\,\boldsymbol{\gamma}_4 - \left(\mathbf{p}_3^T\mathbf{x}_i\right)\mathbf{b}_{i,\xi} - \left(\mathbf{r}_3^T\mathbf{x}_i\right)\mathbf{b}_{i,\eta}\right], \\
\mathbf{b}_{1,\eta\zeta} &= \{N_{a,x\eta\zeta}\} = \frac{1}{64V}\left[C^1_{23}\,\boldsymbol{\gamma}_4 - \left(\mathbf{q}_1^T\mathbf{x}_i\right)\mathbf{b}_{i,\eta} - \left(\mathbf{p}_1^T\mathbf{x}_i\right)\mathbf{b}_{i,\zeta}\right], \\
\mathbf{b}_{2,\eta\zeta} &= \{N_{a,x\eta\zeta}\} = \frac{1}{64V}\left[C^2_{23}\,\boldsymbol{\gamma}_4 - \left(\mathbf{q}_2^T\mathbf{x}_i\right)\mathbf{b}_{i,\eta} - \left(\mathbf{p}_2^T\mathbf{x}_i\right)\mathbf{b}_{i,\zeta}\right], \\
\mathbf{b}_{3,\eta\zeta} &= \{N_{a,x\eta\zeta}\} = \frac{1}{64V}\left[C^3_{23}\,\boldsymbol{\gamma}_4 - \left(\mathbf{q}_3^T\mathbf{x}_i\right)\mathbf{b}_{i,\eta} - \left(\mathbf{p}_3^T\mathbf{x}_i\right)\mathbf{b}_{i,\zeta}\right], \\
\mathbf{b}_{1,\zeta\xi} &= \{N_{a,x\zeta\xi}\} = \frac{1}{64V}\left[C^1_{13}\,\boldsymbol{\gamma}_4 - \left(\mathbf{r}_1^T\mathbf{x}_i\right)\mathbf{r}_{i,\zeta} - \left(\mathbf{q}_1^T\mathbf{x}_i\right)\mathbf{q}_{i,\xi}\right], \\
\mathbf{b}_{2,\zeta\xi} &= \{N_{a,y\zeta\xi}\} = \frac{1}{64V}\left[C^2_{13}\,\boldsymbol{\gamma}_4 - \left(\mathbf{r}_2^T\mathbf{x}_i\right)\mathbf{r}_{i,\zeta} - \left(\mathbf{q}_2^T\mathbf{x}_i\right)\mathbf{q}_{i,\xi}\right], \\
\mathbf{b}_{3,\zeta\xi} &= \{N_{a,z\zeta\xi}\} = \frac{1}{64V}\left[C^3_{13}\,\boldsymbol{\gamma}_4 - \left(\mathbf{r}_3^T\mathbf{x}_i\right)\mathbf{r}_{i,\zeta} - \left(\mathbf{q}_3^T\mathbf{x}_i\right)\mathbf{q}_{i,\xi}\right],
\end{aligned}
$$

where summation over the repeated indices i ($i = 1, 2, 3$) is implied in the above equations. The vectors $\mathbf{r}_i$, $\mathbf{p}_i$ and $\mathbf{q}_i$ are given by:

$$
\begin{aligned}
\mathbf{r}_i &= C^i_{13}\mathbf{h}_1 + C^i_{12}\mathbf{h}_2, \quad i = 1, 2, 3 \text{ (no sum)} \\
\mathbf{p}_i &= C^i_{23}\mathbf{h}_1 + C^i_{12}\mathbf{h}_3, \quad i = 1, 2, 3 \text{ (no sum)} \\
\mathbf{q}_i &= C^i_{23}\mathbf{h}_2 + C^i_{13}\mathbf{h}_3 \quad i = 1, 2, 3 \text{ (no sum)}
\end{aligned}
\tag{A.12}
$$

With the above definitions, the derivatives of the gradient submatrices required for the computations of $\mathbf{K}^e_{stab}$ are given by:

$$
\mathbf{B}_{a,\xi}(\mathbf{0}) = \begin{bmatrix} \mathbf{b}_{1,\xi a} \\ \mathbf{b}_{2,\xi a} \\ \mathbf{b}_{3,\xi a} \end{bmatrix}; \quad \mathbf{B}_{a,\eta}(\mathbf{0}) = \begin{bmatrix} \mathbf{b}_{1,\eta a} \\ \mathbf{b}_{2,\eta a} \\ \mathbf{b}_{3,\eta a} \end{bmatrix}; \quad \mathbf{B}_{a,\zeta}(\mathbf{0}) = \begin{bmatrix} \mathbf{b}_{1,\zeta a} \\ \mathbf{b}_{2,\zeta a} \\ \mathbf{b}_{3,\zeta a} \end{bmatrix};
$$

$$
\mathbf{B}_{a,\xi\eta}(\mathbf{0}) = \begin{bmatrix} \mathbf{b}_{1,\xi\eta a} \\ \mathbf{b}_{2,\xi\eta a} \\ \mathbf{b}_{3,\xi\eta a} \end{bmatrix}; \; \mathbf{B}_{a,\eta\zeta}(\mathbf{0}) = \begin{bmatrix} \mathbf{b}_{1,\eta\zeta a} \\ \mathbf{b}_{2,\eta\zeta a} \\ \mathbf{b}_{3,\eta\zeta a} \end{bmatrix}; \; \mathbf{B}_{a,\zeta\xi}(\mathbf{0}) = \begin{bmatrix} \mathbf{b}_{1,\zeta\xi a} \\ \mathbf{b}_{2,\zeta\xi a} \\ \mathbf{b}_{3,\zeta\xi a} \end{bmatrix}
\tag{A.13}
$$

where, $a = 1, \ldots, 8$ represents the number of nodes in the cube.

Now that all submatrices have been defined, the use of Equation A.4 provides the final form of $\mathbf{K}^e_{stab}$. Finally, a rank sufficient conductivity matrix of an element, e, is obtained using Equation A.1.